Ion Beam Synthesis and Modification of Germanium and Silicon-Germanium for Integration with Silicon Optical Circuits

Ion Beam Synthesis and Modification of Germanium and Silicon-Germanium for Integration with Silicon Optical Circuits

By

ROSS ANTHONY

B. Sc. McMaster University (2019)

A Thesis

Submitted to the School of Graduate Studies in Partial Fulfillment of the

Requirements for the Degree

Doctor of Philosophy

McMaster University (Engineering Physics)

DOCTOR OF PHILOSOPHY (2019)

Hamilton, Ontario

TITLE: Ion Beam Synthesis and Modification of Germanium and Silicon-Germanium for Integration with Silicon Optical Circuits

AUTHOR: Ross Edward Anthony, B.Sc. (McMaster University)

SUPERVISOR: Dr. A. P. Knights

NUMBER OF PAGES: xviii, 137

Abstract

Silicon photonics offers great benefits in terms of cost, performance and power consumption. This is increasingly important as the demand for internet bandwidth continues to grow. Optical detection in silicon photonics is performed via the integration of germanium, one of the more challenging integration steps during fabrication. This thesis describes research into a novel technique to grow silicon-germanium on silicon and its application in waveguide detectors and research performed into the application of germanium at extended wavelengths of light.

Chapter 1 provides a brief introduction to silicon photonics and chapter 2 covers background material on p-n and p-i-n detectors as well as germanium growth on silicon and it's applications in silicon photonics. Chapter 3 presents work done on a germanium condensation technique using high fluence ion implantation, suitable for straightforward silicon-germanium fabrication. Using this technique a crystalline layer of silicon-germanium with a high concentration of 92% germanium was demonstrated. In addition a semi-empirical model was developed using a segregation coefficient, an enhanced linear oxidation rate and transient enhanced diffusion. This technique was then used to fabricate a photodetector for operation at a wavelength of 1310 nm. While the responsivity of the detector of 0.01 A/W was modest, this work presents the first demonstration of a detector fabricated in this way, and as such provides a foundation for future improved devices. Chapter 4 presents work done on p-i-n germanium detectors to increase their detection limit in the thulium doped fibre amplifier band. This work originally focused on using mid-bandgap lattice defects introduce via ion implantation to improve the detection limit.

However, during this experimental work it was determined that the unimplanted samples had a responsivity of 0.07 A/W at 1850 nm and 0.02 A/W at 2000 nm which was higher than that of the defect implanted samples and so the unimplanted samples were investigated further. From this work it was found that the absorption of the germanium detectors was 0.003 μm^{-1} at 1900 nm, which is approximately a factor of 10 greater than that of bulk germanium. The increased responsivity and absorption coefficient were attributed to tensile strain in the germanium. In Chapter 5 Raman spectroscopy was employed in order to investigate the detectors described in chapter 4 and confirm the presence of tensile strain. When compared with Raman spectra from a bulk germanium sample it was found that the detectors were experiencing 0.27 to 0.48 % tensile strain, consistent with the enhanced absorption at extended wavelengths. Nanowire bridges were then fabricated in germanium and silicon-germanium and characterized using Raman spectroscopy. Germanium was found to have enhanced strain in the nanowire with an enhancement of up to 13.5 demonstrated, whereas for the silicon-germanium samples the structures were shown to reduce the compressive strain in the samples. It is concluded that strain engineering is a very promising route for the development of extended wavelength detectors integrated with silicon photonic systems.

Acknowledgements

I would like to begin by thanking my supervisor Andy Knights for his support, guidance and patience throughout this process. I would also like to thank my committee members Ayse Turak, and Peter Mascher for their encouragement and advice.

I would also like to thank all of the members of the Knights group both past and present for their friendship and help these past few years, Edgar *'Dr. H-bomb'* Huante-Ceron, Jason *'J-roc'* Ackert, Zhao *'the chairman'* Wang, Dixon *'D$'* Paez-Capacho, Kyle *'KFM Radio'* Murray, Jimmy *'the angry one'* Zheng, David *'DJ-L'* Hagan, Jeremy *'the thriller'* Miller, Dylan Genuth-Okon, Connor Wong, Matt Vukovic, Ashley Gilbank and Yanran Xie.

To Doris Stevanovic, Zhiling Peng, and Shahram Tavakoli, thank you so much for your the many hours that you spent helping with sample preparation, training and fixing equipment to make this work possible. I would also like to thank Simon Ruffell for his help.

The work done in this thesis would not have been accomplished without the help of Yaser Haddara of McMaster University and Iain Crowe at the University of Manchester.

To my partner Kirsten thank you for your love, support and putting up with me throughout this process. I would also like to thank my daughter Eloise for motivating me to finish.

Last and most important of all I would like to thank my parents without whom none of this would have been possible.

Table of Contents

List of Figures

List of Tables

List of Acronyms & Abbreviations

AFM – Atomic Force Microscopy

BOX – Buried Oxide

CMOS – Complementary Metal-Oxide-Semiconductor

CCD – Charge-Coupled Device

DC – Direct Current

EDS – Energy Dispersive X-ray Spectroscopy

EDFA – Erbium Doped Fibre Amplifier

EF – Enhancement Factor of Strain

EOR – End of Range

Ge – Germanium

HR-TEM – High Resolution-Transmission Electron Microscope

LEP-CVD – Low-energy plasma enhanced Chemical Vapour Deposition

MPWS – Multi Project Wafers

MBE – Molecular Beam Epitaxy

NI – Normal Incidence

RBS – Rutherford Backscattering

SEM – Scanning Electron Microscope

SNR – Signal to Noise Ratio

Si – Silicon

SiGeOI – Silicon-Germanium-On-Insulator

SOI – Silicon-On-Insulator

SiO_2 – Silicon Dioxide

STEM – Scanning-Transmision Electron Microscope

TCAD – Technology Computer Aided Design

TDFA – Thulium Doped Fibre Amplifier

TED – Transient Enhanced Diffusion

TEM – Transmission Electron Microscope

UHV-CVD – Ultra-High Vacuum Chemical Vapour Deposition

WDM – Wavelength Division Multiplexing

WGI – Waveguide Integrated

Chapter 1 – Introduction

1.1 Optical interconnects

Improvement in computing power and the development of optical fibre networks over the last three decades have enabled individuals to use devices with relatively low functionality (for example a smartphone) to access a wide range of services. As a result this has enabled the rise of social media (notably via companies such as Facebook, Twitter and Instagram), video streaming (Netflix, Youtube, Hulu, Amazon Prime) and cloud computing and storage (Dropbox). The infrastructure backbone of all of these services are datacenters- large scale systems housing thousands of processors. However, with the amount of internet traffic predicted to grow [1], datacenters in their current incarnation will begin to reach their limitations in terms of bandwidth and while it is possible to address these limitations by adding more processors to these systems, this will lead ultimately to a consumption of an unsustainable amount of power [2].

For some years, a new method of interconnection without metal has been sought such that optical interconnects, using photons instead of electrons, will send signals between processors [3]. This is motivated because of several metal interconnect limitations. For metal interconnects at room temperature the number of bits per second that can be transmitted is limited to:

$$B = 10^{16} \frac{A}{L^2} \tag{1.1}$$

with area A of the line fixed by the so-called skin effect, where for an AC source most of the current is concentrated in the area around the surface of the wire; while the length L

of the interconnect is dictated by the physical setup of the datacenter [3]. In addition, electrical buses can only be designed to work at a small range of frequencies due to differences in loss, cross talk and impedance mismatch associated with different speeds of modulation [4–6]. Optical interconnects do not suffer from any of the above-mentioned problems, can increase transmission rates by using Wavelength-Division-Multiplexing (WDM) where multiple wavelengths of light are transmitted on the same optical bus [7]; and also provide reduced power consumption when compared with metal interconnects as a result of the lack of resistive heating [8]. Connections can be replaced with active optical fibres [9], most efficiently taking full advantage of integration where the photonic components such as a laser, modulator and detector are integrated directly onto a single platform [10].

1.2 Silicon photonics

While there is a definite need for optical interconnection, there are multiple potential solutions all of which can operate with comparable performance. However, the scale of volume required to produce the necessary number of interconnects makes cost a priority [11–13]. Silicon photonics, which is based on the use of Silicon-on-Insulator (SOI) as the material platform, from the perspective of cost and maturity of technology, is one of the best potential solutions as it leverages years of research and development from the complementary metal-oxide-semiconductor (CMOS) industry, with devices produced at the wafer level at a relatively low cost. While SOI was originally developed for use in electronics][14, 15], it is an excellent choice of material for optics as the buried oxide

(BOX), which is made up of silicon dioxide (SiO_2), has a large index contrast from that of Silicon (Si) (~3.4 for Si and ~1.4 for SiO_2), at the wavelengths of interest (1.3-1.62 μm), allowing for optical confinement of light. In addition, Si's optical band-edge is ~1100 nm which is below the wavelength range of modern communication. This allows for the fabrication of low loss waveguides, a schematic diagram of an example waveguide is shown in Fig. 1.1, a fundamental building block of any optical circuit [16].

As the cost of outfitting and maintaining a state-of-the-art semiconductor fabrication facility is prohibitively high, from both a research and small business perspective, Si photonics also offers benefits due to the access to Multi-Project Wafers

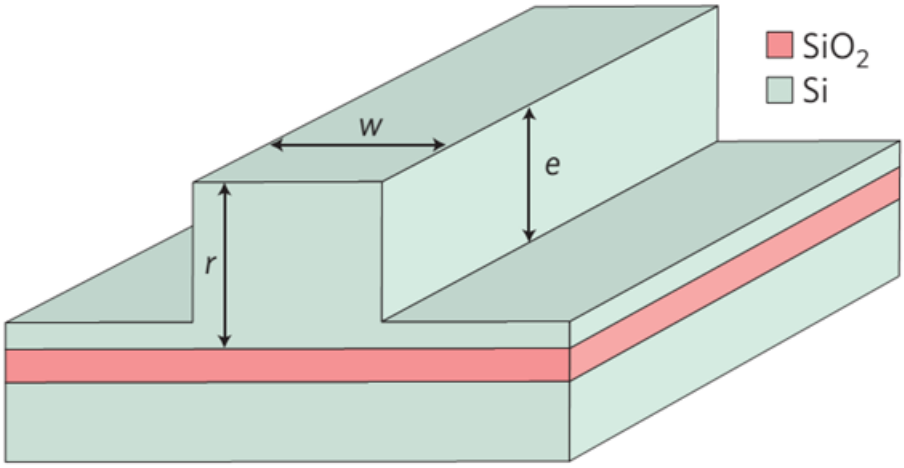

Fig. 1.1 Schematic diagram of a Si waveguide. Figure reproduced from [11] © 2014 NPG.

(MPWS). MPWS are offered by large facilities to multiple-users utilising a common process flow, thus the cost of fabrication is shared between users. Designs are submitted by said users and then fabricated at a CMOS foundry such as IME A-Star in Singapore or IMEC in Belgium. In addition to the reduction in cost, this allows for better repeatability of design as the fabrication methods and tolerances at such foundries are well-understood. The biggest disadvantage of MPWS runs is the need for stringent design rules, so while

there may be elegant solutions to a specific problem in Si photonics, for example enhancing strain in Ge to increase the detection limit and emission properties, if it does not meet the rules of a given fabrication facility, then the solution cannot be explored during standard fabrication [17–19]. This does not however preclude its adoption by the foundry at a later date following process verification.

While Si photonics, from a cost perspective is one of the best solutions for a route to optical interconnection, it is not without its own problems, specifically in relation to the building blocks of an optical circuit. For example, as stated above, the Si optical bandgap is much smaller than the wavelengths of interest. Thus, what makes Si good at guiding light makes it unsuitable as a detector and possible light source (although the indirect bandgap of Si precludes the fabrication of a Si laser at this time). In addition, Si has no Pockel's effect and weak 2^{nd} order properties, due to the symmetry of its crystalline structure, making modulation difficult. These challenges are now further described, together with the most successful approaches to their resolution.

1.2.1 Light source

The development of light sources for Si photonic circuits is of great interest, with the goal being an electrically pumped source which emits at either 1310 nm or 1550 nm and is fully CMOS compatible [20]. Whether it is necessary for the light source to be on-chip or off-chip may depend on the application, however. On-chip light sources are more desirable as they avoid the extra coupling loss associated with fibre coupling to an off-chip source, and allow for ease of integration and packaging [21]. For on-chip light sources Si Raman lasers, Si nanocrystals, III-V based devices fabricated both by direct

growth and wafer bonding techniques, Ge and GeSn, and erbium doped materials have all

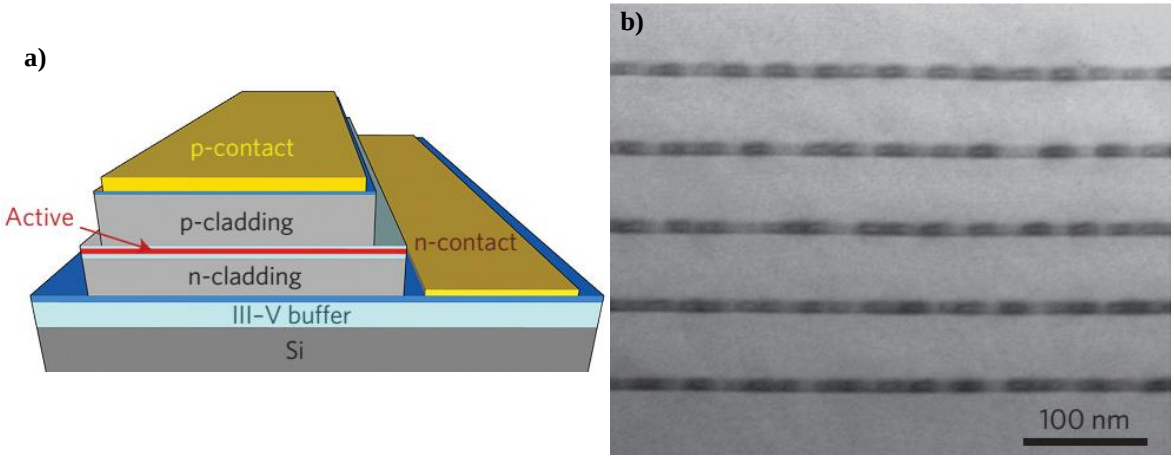

Fig. 1.2 a) Schematic diagram of an InP quantum dot laser and b) a Transmission electron microscope (TEM) image of the active layer of an InP quantum dot laser. Figure reproduced from [26] © 2016 NPG.

been investigated. Si Raman lasers [22] do not meet the current requirements for lasers in Si photonics as they both require high power optical pumps, while it is still unclear as to whether Si nanocrystals actually produce optical gain [23]. III-V wafer bonded devices have been demonstrated with high optical gain and output power, with the downside being that the wafer bonding technique increases the fabrication complexity making high volume production costly [24, 25]. III-V devices grown directly on Si either using buffer layers such as silicon-germanium (SiGe) or GaAs to reduce threading dislocations have been demonstrated as well as quantum dots grown directly on Si, an example of which is shown in Fig. 1.2. [26]. Both of these direct growth techniques currently have worse device characteristics than for wafer bonded devices but are a very promising area of future research. Electrically pumped Ge lasers have also been demonstrated, however, devices have a very high current threshold. This is a consequence of Ge lasers being

highly *n*-doped close to the point of solid solubility in Ge [27]. Strain can be used to reduce the need for *n*-doping but this has several drawbacks as some device schemes require optical pumping [28] and also result in red-shifting the emission wavelength to beyond the point where it can be used for current Si photonic devices [29]. Another method for avoiding high *n*-doping is introducing tin (Sn) into the lattice; to date though only optically pumped GeSn light sources have been demonstrated [30]. In addition, Sn redshifts the wavelength higher than would be desired for current optical links. GeSn is also difficult to grow due the lattice mismatch between Ge and Sn and poor equilibrium solubility of Sn in Germanium [31]. While both strain enhanced Ge and GeSn are poor candidates for 1.3-1.62 μm, the red shifting of their optical bandgap makes them interesting candidates for mid-infrared applications. Therefore, it is possible that there will be development of an optical link at a wavelength where Ge or GeSn is used as both the emission source and detector [32, 33]. Erbium-related light sources offer a very interesting area of research especially given the success of the erbium doped fiber amplifier (EDFA) with optically pumped erbium lasing being demonstrated [34, 35]. These devices however, have poor electrical characteristics due to the dielectric nature of the materials doped with erbium such as SiO_x [36], SiN_x [37] and erbium silicates [38]. For the wavelength window of 1300-1620 nm, III-V lasers bonded to Si have been seen as the defacto laser for commercial applications where off-chip coupling is undesirable. However, with the development of direct growth of III-V's on Si, it is perhaps only a matter of time before this is no longer the case.

1.2.2 Modulators

For high speed optical communication there is an obvious need to modulate the signal, and while it is possible to perform direct modulation of a laser, this is undesirable as it adds another level of complication to designing a light source, and in general direct modulation technologies are bandwidth limited [39]. Therefore, it is often preferable to

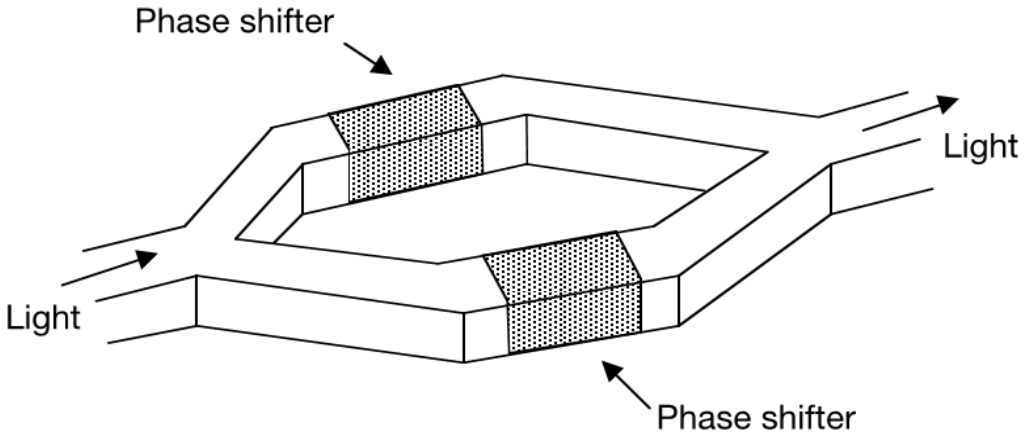

Fig.1.3 Schematic diagram of a Mach-Zender modulator. Figure reproduced from [43] © 2004 NPG.

introduce the modulator as a separate component. By exploiting the use of the plasma-dispersion effect, whereby the refractive index of Si is changed by altering the carrier concentration [40] (either via carrier injection [41] or depletion), Si modulators [42] can be integrated monolithically into Si photonic circuits. These modulators most often employ carrier depletion as it avoids the long minority carrier lifetimes in Si allowing for increased speeds of modulation. The most commonly used devices in Si photonics which exploit this effect are Mach-Zender Interforemeters [43] and microring resonators [44]. While the most important characteristics for a modulator is clearly the speed at which it can modulate there are several other factors which must be considered such as the footprint of the device, the extinction ratio and the power consumption. As shown in Fig

1.3 Mach-Zehnders operate by altering the phase difference between two waveguide arms allowing for constructive and destructive interference. Mach-Zehnders offer good speeds of modulation (>40 GHz), high extinction ratio, are temperature insensitive and have a large optical bandwidth. Unfortunately, they require a large footprint, up to several mm^2, and as a consequence of this also require a high amount of energy per bit.

Microring resonators, a schematic of which is shown in Fig. 1.4, operate by

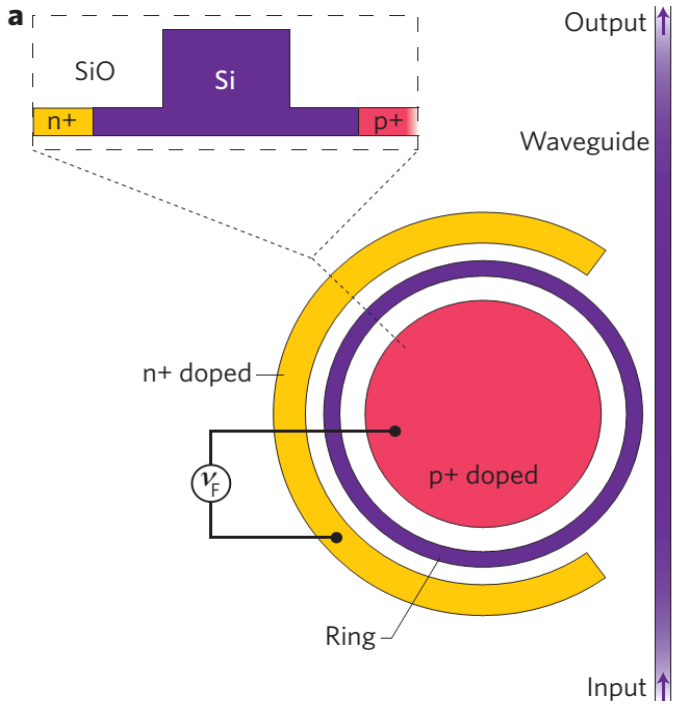

Fig. 1.4 Schematic diagram of a Si microring resonator modulator. Figure reproduced from [44] © 2005 NPG.

moving the resonant wavelength of the ring. They are relatively compact (the bend radius can be on the order of 10's of μms), have relatively low power consumption, and can be used for WDM. However, they have a small optical bandwidth and are very sensitive to manufacturing tolerances and the temperature at which the device will operate. It is

feasible to stabilize such devices with respect to temperature, however this results in increasing the energy consumption per bit.

While the above mentioned devices operate by employing changes in the real part of the refractive index, work has also been performed on modulators which change the imaginary part of the refractive index and are referred to as electro-absorption modulators [45]. These devices are generally fabricated for high-speed operation using SiGe and have been demonstrated in waveguides using both the Franz-Keldysh effect, where as shown in the schematic diagram in Fig .1.5 [46] the modulation occurs in a uniform SiGe layer, and the quantum confinement stark effect [47] which employs the use of SiGe

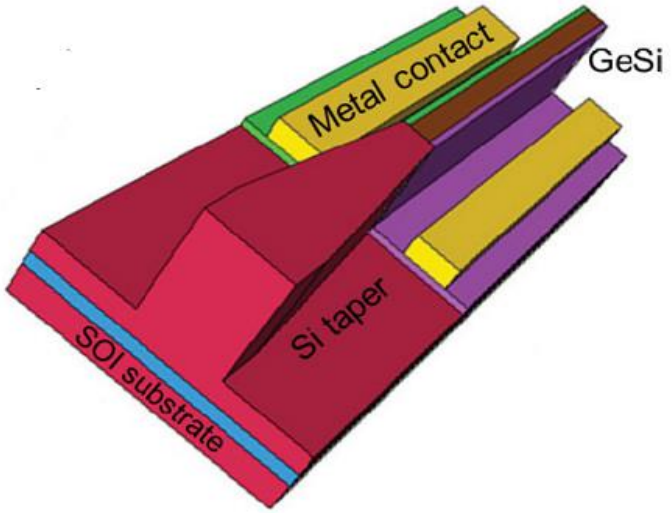

Fig. 1.5 Schematic diagram of a SiGe electro-absorption modulator. Figure reproduced from [46] © 2012 Optical Society of America.

quantum wells. While these devices offer comparable performance to monolithic Si modulators, they too are susceptible to thermal stability while the fabrication of quantum wells is complex.

1.2.3 Detection

There are several viable options for detectors in Si photonics: integrated III-V's [48], defect mediated detection [49] and directly grown germanium (Ge) [50]. III-V's appear to provide an optimal solution offering high speed detection at the desired wavelengths.

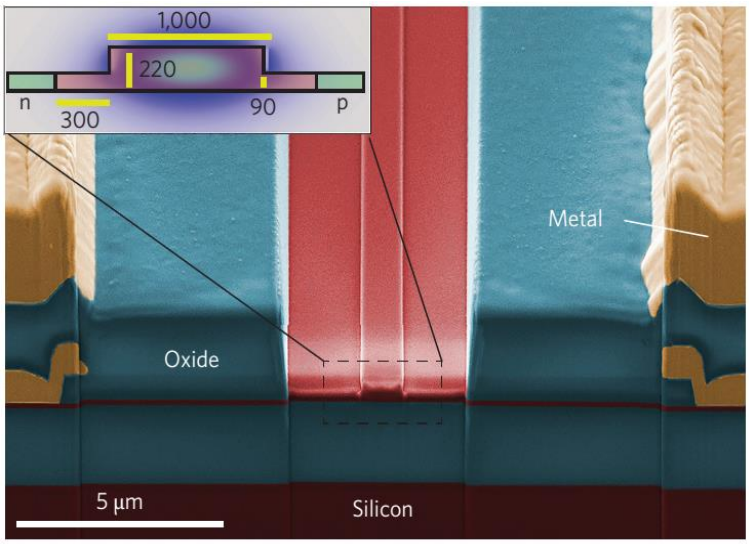

Fig. 1.6 Scanning electron microscope (SEM) image of an all Si photodetector using defect mediated detection. Figure reproduced from [51] © 2015 NPG.

Integration may take place via bonding or direct growth in a manner similar to that used for light source integration. However, integration of III-V material with Si always presents issues with CMOS process compatibility. To enable defect mediated detection, defects are created in the Si lattice, which introduce mid gap states in the band structure. This is readily achieved by implanting an inert element such as Si. Defect mediated detection poses an interesting solution as it is compatible with CMOS processing, requires no difficult growth step and is easy to control. An SEM of such a device is shown in Fig. 1.6, and there have been demonstrations of high-speed operation beyond 2 µm [51]. However, these detectors require a large footprint and have a reduced

responsivity as compared with both III-V's and Ge. Ge detectors are compatible with CMOS processing and have a much higher absorption coefficient as compared with defect detectors allowing for a small device footprint. While the growth of high-quality Ge-on-Si is now available through central fabrication facilities, sophisticated and expensive technologies are required to overcome issues associated with the significant lattice mismatch of 4% between Si and Ge. This mismatch can result in, for example, islanding and a large number of defects providing an unwanted dark current and reduced responsivity [52]. These problems have been addressed over the last several years through the use of a low-temperature/high-temperature growth method (to be detailed in later sections) resulting in high quality Ge detectors. A schematic diagram and SEM of one such detector is shown in Fig 1.7 a and b respectively [53]. These devices have good speed of operation and good responsivity from 1.3-1.55 μm, with detection at higher wavelengths being enabled through the use of strain [54]. However, there is still a desire

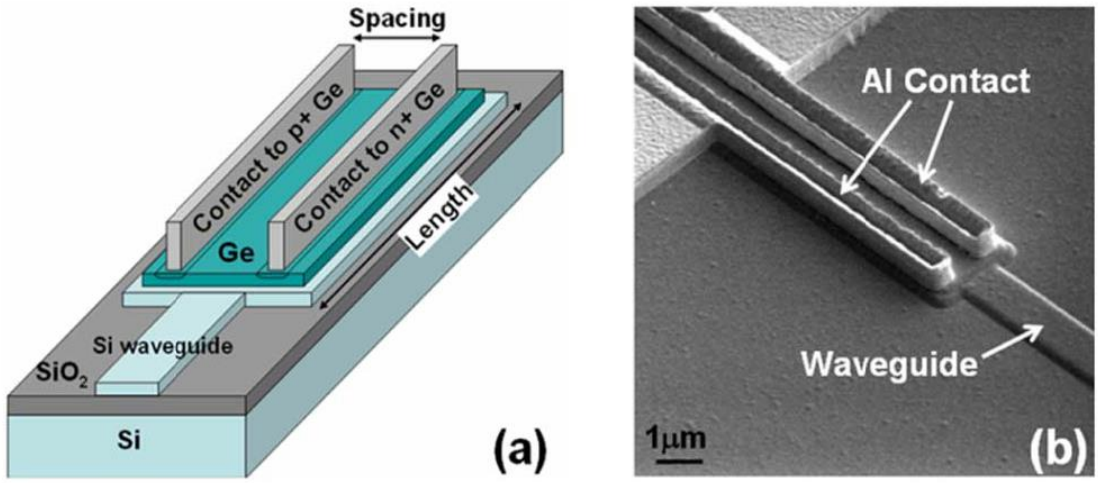

Fig. 1.7 a) Schematic diagram and b) SEM of a Ge photodetector. Figure reproduced from [53] © 2008 IEEE.

to reduce the dark current of such detectors into the nA range to keep power requirements low [55].

1.3 Statement of thesis work

This thesis contributes to knowledge on the integration of Ge with silicon-based technologies, primarily through the use of ion implantation for fabrication or post-growth modification; or through the use of strain engineering.

In Chapter 2 a brief summary of the theoretical operation of a detector is presented, followed by a literature review of the growth of Ge-on-Si and the use of Ge-on-Si as a platform for detection.

In Chapter 3 the formation of Silicon-Germanium-On-Insulator (SiGeOI) through implantation and condensation is presented. The composition and strain of the SiGe layer and rate of oxidation are analyzed and discussed and a model is presented for the formation of the SiGeOI. Finally, the developed process is used to fabricate a photodetector. Loss and electrical measurements are included to give a full understanding of the detector. The model was developed in collaboration with Prof. Yaser Haddara of McMaster University and Dr. Iain Crowe of Manchester University facilitated Raman analysis.

Chapter 4 describes the results from operation of a PIN Ge detector at extended wavelengths in the range 1.85 – 2.01 μm. The use of defect mediated detection in Ge is also presented for the first time. The high speed operation of the PIN detector is presented and the optical absorption length of Ge at 2 μm is calculated.

In Chapter 5 the use of strain engineering for both SiGe and Ge bridges is presented with an examination of the enhancement of Ge's absorption when subjected to strain. Raman data in this chapter was collected by myself with the assistance of Dr. Iain Crowe of Manchester University who provided access to the Raman spectrometer and training in analyzing the spectra.

The thesis concludes with chapter 6; a summary and suggestions for future work.

1.4 Publications

Journal papers that resulted from the research reported in this thesis are listed as follows:

R. Anthony, D. Hagan, D. Genuth-Okon, J. Mullins, I. F. Crowe, M. P. Halsall, and A. P. Knights, "Extended wavelength responsivity of a germanium photodetector integrated with a silicon waveguide" *IEEE Journal of Lightwave Technology,* 2019 (submitted)

R. Anthony, Y. M. Haddara, I. F. Crowe, and A. P. Knights "SiGe-on-insulator fabricated via germanium condensation following high-fluence Ge^+ ion implantation" *J. of Appl. Phys.,* vol. 122, no. 6, 2017.

Conference proceedings that are also part of the thesis work are listed as follows:

R. Anthony, A. Gilbank, I. Crowe, A. Knights, "Strain Analysis of SiGe Microbridges" *Proc. of SPIE,* 10537, Silicon Photonics XIII, San Francisco, 2018

References

[1] Cisco White Paper, "Cisco Global Cloud Index: Forecast and Methodology 2015-2020," 2015.

[2] A. K. Kodi, B. Neel, and W. C. Brantley, “Photonic interconnects for exascale and datacenter architectures,” *IEEE Micro*, vol. 34, no. 5, pp. 18–30, 2014.

[3] D. A. B Miller, “Rationale and challenges for optical interconnects to electronic\nchips,” *Proc. IEEE*, vol. 88, no. 6, pp. 728–749, 2000.

[4] D. A. B. Miller and H. M. Ozaktas, “Limit to the Bit-Rate Capacity of Electrical Interconnects from the Aspect Ratio of the System Architecture,” *J. Parallel Distrib. Comput.*, vol. 41, no. 1, pp. 42–52, 1997.

[5] C. Kachris and I. Tomkos, “A survey on optical interconnects for data centers,” *IEEE Communications Surveys and Tutorials*, vol. 14, no. 4. IEEE, pp. 1021–1036, 2012.

[6] D. A. B. Miller, “Device requirements for optical interconnects to silicon chips,” *Proc. IEEE*, vol. 97, no. 7, pp. 1166–1185, 2009.

[7] R. S. Tucker, R. Parthiban, J. Baliga, K. Hinton, R. W. A. Ayre, and W. V. Sorin, “Evolution of WDM optical IP networks: A cost and energy perspective,” *J. Light. Technol.*, vol. 27, no. 3, pp. 243–252, 2009.

[8] M. R. Feldman, S. C. Esener, C. C. Guest, and S. H. Lee, “Comparison between optical and electrical interconnects based on power and speed considerations,” *Appl. Opt.*, vol. 27, no. 9, pp. 1742–1751, 2009.

[9] C. Lam, H. Liu, B. Koley, X. Zhao, V. Kamalov, and V. Gill, “Fiber optic communication technologies: What’s needed for datacenter network operations,” *IEEE Commun. Mag.*, vol. 48, no. 7, pp. 32–39, 2010.

[10] J. E. Cunningham, A. V Krishnamoorthy, R. Ho, I. Shubin, H. Thacker, J. Lexau, D. C. Lee, D. Feng, E. Chow, Y. Luo, X. Zheng, G. Li, J. Yao, T. Pinguet, K. Raj, M.

Asghari, and J. G. Mitchell, “Integration and packaging of a macrochip with silicon nanophotonic links,” *IEEE J. Sel. Top. Quantum Electron.*, vol. 17, no. 3, pp. 546–558, 2011.

[11] M. Asghari and A. V. Krishnamoorthy, “Silicon Photonics: Energy-Efficient Communication,” *Nat. Photonics*, vol. 5, pp. 268–270, 2011.

[12] A. Rickman, “The commercialization of silicon photonics,” *Nat. Photonics*, vol. 8, no. 8, pp. 579–582, 2014.

[13] Y. Arakawa, T. Nakamura, Y. Urino, and Fu, “Silicon Photonics for Next Generation System Integration Platform,” vol. 51, no. 3, pp. 72–77, 2013.

[14] M. Bruel, B. Aspar, and A. J. Auberton-Hervé, “Smart-cut: A new silicon on insulator material technology based on hydrogen implantation and wafer bonding,” *Japanese J. Appl. Physics, Part 1 Regul. Pap. Short Notes Rev. Pap.*, vol. 36, no. 3 SUPPL. B, pp. 1636–1641, 1997.

[15] M. Bruel, “Silicon on insulator material technology,” *Electron. Lett.*, vol. 31, no. 14, p. 1201, 2002.

[16] R. Soref, L. Fellow, and I. Paper, “The Past , Present , and Future of Silicon Photonics,” *IEEE J. Sel. Top. Quantum Electron.*, vol. 12, no. 6, pp. 1678–1687, 2006.

[17] M. Hochberg and T. Baehr-Jones, “Towards fabless silicon photonics,” *Nat. Photonics*, vol. 4, no. 8, pp. 492–494, 2010.

[18] M. Hochberg, N. Harris, R. Ding, Y. Zhang, A. Novack, Z. Xuan, and T. Baehr-Jones, “Silicon photonics: The next fabless semiconductor industry,” *IEEE Solid-State Circuits Mag.*, vol. 5, no. 1, pp. 48–58, 2013.

[19] A. E. J. Lim, J. Song, Q. Fang, C. Li, X. Tu, N. Duan, K. K. Chen, R. P. C. Tern, and T. Y. Liow, "Review of Silicon Photonics Foundry Efforts," *IEEE J. Sel. Top. Quantum Electron.*, vol. 20, no. 4, pp. 405–416, 2014.

[20] Z. Zhou, B. Yin, and J. Michel, "On-chip light sources for silicon photonics," *Light Sci. Appl.*, vol. 4, no. 11, pp. 1–13, 2015.

[21] M. J. R. Heck and J. E. Bowers, "Energy efficient and energy proportional optical interconnects for multi-core processors: Driving the need for on-chip sources," *IEEE J. Sel. Top. Quantum Electron.*, vol. 20, no. 4, 2014.

[22] H. Rong, A. Liu, R. Jones, O. Cohen, and D. Hak, "An all-silicon Raman laser," vol. 433, no. 7023, pp. 292–294, 2005.

[23] L. Pavesi, L. Dal Negro, C. Mazzoleni, G. Franzo, and F. Priolo, "Optical gain in silicon nanocrystals," *Nature*, vol. 408, pp. 440–444, 2000.

[24] X. Sun, A. Zadok, M. J. Shearn, K. A. Diest, A. Ghaffari, H. A. Atwater, A. Scherer, and A. Yariv, "Electrically pumped hybrid evanescent Si/InGaAsP lasers," *Opt. Lett.*, vol. 34, no. 9, pp. 1345–1347, 2009.

[25] K. Tanabe, K. Watanabe, and Y. Arakawa, "III-V/Si hybrid photonic devices by direct fusion bonding," *Sci. Rep.*, vol. 2, pp. 1–6, 2012.

[26] S. Chen, W. Li, J. Wu, Q. Jiang, M. Tang, S. Shutts, S. N. Elliott, A. Sobiesierski, A. J. Seeds, I. Ross, P. M. Smowton, and H. Liu, "Electrically pumped continuous-wave III-V quantum dot lasers on silicon," *Nat. Photonics*, vol. 10, no. 5, pp. 307–311, 2016.

[27] J. Liu, X. Sun, D. Pan, X. Wang, L. C. Kimerling, T. L. Koch, and J. Michel, "Tensile-strained, n-type Ge as a gain medium for monolithic laser integration on Si,"

Opt. Express, vol. 15, no. 18, p. 11272, 2007.

[28] S. Bao, D. Kim, C. Onwukaeme, S. Gupta, K. Saraswat, K. H. Lee, Y. Kim, D. Min, Y. Jung, H. Qiu, H. Wang, E. A. Fitzgerald, C. S. Tan, and D. Nam, "Low-threshold optically pumped lasing in highly strained germanium nanowires," *Nat. Commun.*, vol. 8, no. 1, pp. 1–7, 2017.

[29] R. Camacho-Aguilera, Z. Han, Y. Cai, L. C. Kimerling, and J. Michel, "Direct band gap narrowing in highly doped Ge," *Appl. Phys. Lett.*, vol. 102, no. 15, p. 152106, 2013.

[30] S. Wirths, R. Geiger, N. Von Den Driesch, G. Mussler, T. Stoica, S. Mantl, Z. Ikonic, M. Luysberg, S. Chiussi, J. M. Hartmann, H. Sigg, J. Faist, D. Buca, and D. Grützmacher, "Lasing in direct-bandgap GeSn alloy grown on Si," *Nat. Photonics*, vol. 9, no. 2, pp. 88–92, 2015.

[31] K. P. Homewood and M. A. Lourenço, "Optoelectronics: The rise of the GeSn laser," *Nat. Photonics*, vol. 9, no. 2, pp. 78–79, 2015.

[32] R. Soref, "Mid-infrared photonics in silicon and germanium," *Nat. Photonics*, vol. 4, no. 8, pp. 495–497, 2010.

[33] J. Zheng, S. Wang, Z. Liu, H. Cong, C. Xue, C. Li, Y. Zuo, B. Cheng, and Q. Wang, "GeSn p-i-n photodetectors with GeSn layer grown by magnetron sputtering epitaxy," *Appl. Phys. Lett.*, vol. 108, no. 3, pp. 1–5, 2016.

[34] L. Yang, D. K. Armani, and K. J. Vahala, "Fiber-coupled erbium microlasers on a chip," *Appl. Phys. Lett.*, vol. 83, no. 5, pp. 825–826, 2003.

[35] A. Polman, B. Min, J. Kalkman, T. J. Kippenberg, and K. J. Vahala, "Ultralow-

threshold erbium-implanted toroidal microlaser on silicon," *Appl. Phys. Lett.*, vol. 84, no. 7, pp. 1037–1039, 2004.

[36] G. M. Miller, R. M. Briggs, and H. A. Atwater, "Achieving optical gain in waveguide-confined nanocluster-sensitized erbium by pulsed excitation," *J. Appl. Phys.*, vol. 108, no. 6, p. 063109, 2010.

[37] L. Dal Negro, J. H. Yi, J. Michel, L. C. Kimerling, T. W. F. Chang, V. Sukhovatkin, and E. H. Sargent, "Light emission efficiency and dynamics in silicon-rich silicon nitride films," *Appl. Phys. Lett.*, vol. 88, no. 23, pp. 2004–2007, 2006.

[38] X. J. Wang, T. Nakajima, H. Isshiki, and T. Kimura, "Fabrication and characterization of Er silicates on SiO2 /Si substrates," *Appl. Phys. Lett.*, vol. 95, no. 4, p. 041906, 2009.

[39] G. T. Reed, G. Mashanovich, F. Y. Gardes, and D. J. Thomson, "Silicon optical modulators," *Nat. Photonics*, vol. 4, no. 8, pp. 518–526, 2010.

[40] R. A. Soref and B. R. Bennett, "Electro-optical effects in Silicon," *IEEE J. Quantum Electron.*, vol. QE-23, no. 1, pp. 123–129, 1987.

[41] Q. Xu, S. Manipatruni, B. Schmidt, J. Shakya, and M. Lipson, "12.5 Gbit/s carrier-injection-based silicon micro-ring silicon modulators," *Opt. Express*, vol. 15, no. 2, pp. 430–436, 2007.

[42] A. Liu, L. Liao, D. Rubin, H. Nguyen, B. Ciftcioglu, Y. Chetrit, N. Izhaky, and M. Paniccia, "High-speed optical modulation based on carrier depletion in a silicon waveguide," *Opt. Express*, vol. 15, no. 2, p. 660, 2007.

[43] A. Liu, R. Jones, L. Liao, D. Samara-Rubio, D. Rubin, O. Cohen, R. Nicolaescu,

and M. Paniccia, “A high-speed silicon optical modulator based on a metal-oxide-semiconductor capacitor.,” *Nature*, vol. 427, no. 12, pp. 615–618, 2004.

[44] Q. Xu, B. Schmidt, S. Pradhan, and M. Lipson, “Micrometre-scale silicon electro-optic modulator,” vol. 435, no. May, pp. 325–327, 2005.

[45] J. Liu, M. Beals, A. Pomerene, S. Bernardis, R. Sun, J. Cheng, L. C. Kimerling, and J. Michel, “Waveguide-integrated, ultralow-energy GeSi electro-absorption modulators,” *Nat. Photonics*, vol. 2, no. 7, pp. 433–437, 2008.

[46] D. Feng, S. Liao, H. Liang, J. Fong, B. Bijlani, R. Shafiiha, B. J. Luff, Y. Luo, J. Cunningham, A. V. Krishnamoorthy, and M. Asghari, “High speed GeSi electro-absorption modulator at 1550 nm wavelength on SOI waveguide,” *Opt. Express*, vol. 20, no. 20, p. 22224, 2012.

[47] S. Ren, Y. Rong, S. A. Claussen, R. K. Schaevitz, T. I. Kamins, J. S. Harris, and D. A. B. Miller, “Ge/SiGe quantum well waveguide modulator monolithically integrated with SOI waveguides,” *IEEE Photonics Technol. Lett.*, vol. 24, no. 6, pp. 461–463, 2012.

[48] J. Brouckaert, S. Member, G. Roelkens, and S. Member, “Compact InAlAs – InGaAs Metal – Semiconductor – Metal Photodetectors Integrated on Silicon-on-Insulator Waveguides,” vol. 19, no. 19, pp. 1484–1486, 2007.

[49] J. K. Doylend, P. E. Jessop, and A. P. Knights, “Silicon photonic resonator-enhanced defect-mediated photodiode for sub-bandgap detection,” *Opt. Express*, vol. 18, no. 14, pp. 14671–14678, 2010.

[50] D. Feng, S. Liao, P. Dong, N. N. Feng, H. Liang, D. Zheng, C. C. Kung, J. Fong, R. Shafiiha, J. Cunningham, A. V Krishnamoorthy, and M. Asghari, “High-speed Ge

photodetector monolithically integrated with large cross-section silicon-on-insulator waveguide," *Appl. Phys. Lett.*, vol. 95, p. 261105, 2009.

[51] J. J. Ackert, D. J. Thomson, L. Shen, A. C. Peacock, P. E. Jessop, G. T. Reed, G. Z. Mashanovich, and A. P. Knights, "High-speed detection at two micrometres with monolithic silicon photodiodes," *Nat. Photonics*, vol. 9, no. 6, pp. 393–396, 2015.

[52] J. Michel, J. Liu, and L. C. Kimerling, "High-performance Ge-on-Si photodetectors," *Nat. Photonics*, vol. 4, no. 8, pp. 527–534, 2010.

[53] J. Wang, W. Y. Loh, K. T. Chua, H. Zang, Y. Z. Xiong, S. M. F. Tan, M. B. Yu, S. J. Lee, G. Q. Lo, and D. L. Kwong, "Low-voltage high-speed (18 GHz/1 V) evanescent-coupled thin-film-Ge lateral PIN photodetectors integrated on Si waveguide," *IEEE Photonics Technol. Lett.*, vol. 20, no. 17, pp. 1485–1487, 2008.

[54] J. Liu, D. D. Cannon, K. Wada, Y. Ishikawa, S. Jongthammanurak, D. T. Danielson, J. Michel, and L. C. Kimerling, "Tensile strained Ge p-i-n photodetectors on Si platform for C and L band telecommunications," *Appl. Phys. Lett.*, vol. 87, no. 1, 2005.

[55] A. M. Urbas, Z. Jacob, L. Dal, D. Thomson, A. Zilkie, J. E. Bowers, and T. Komljenovic, "Roadmap on silicon photonics," *J. Opt.*, vol. 18, no. 7, pp. 1–20, 2017.

Chapter 2 – Background and Theoretical Considerations

Overview

This chapter is divided into three sections. The first will describe the theory that underpins photodetectors, the primary application of Ge in silicon photonics. The second will review approaches to the growth of Ge and SiGe on Si. The third section will review the fabrication techniques used in the thesis.

2.1 Ge photodetectors

This section reviews the theory of semiconductor photodetectors, specifically that of p-n and p-i-n detectors. While there are many types of semiconductor photodetector, I will limit the section to describing the p-n and p-i-n detector because these are the designs most used using Ge-Si. For further background the reader is referred to the classic text *Physics of Semiconductor Devices* by S. M. Sze [1].

2.1.1 p-n and p-i-n photodetector

p-n junctions are produced in semiconductors with altered carrier concentrations with the p-type region being more highly doped with acceptor atoms (where a dopant atom replaces an intrinsic atom in the lattice and has one less electron than the intrinsic semiconductor thus introducing a hole into the lattice) and the n-type region being more highly doped with donor atoms (where a dopant atom replaces a intrinsic atom in the

lattice and has one more electron than the intrinsic semiconductor thus introducing an electron). The formation of a p-n junction, as demonstrated in Fig. 2.1, occurs when the p-doped and n-doped regions are adjacent. To establish equilibrium, there is a diffusion of free charge carriers, known as the diffusion current, with electrons moving to the p-type region, leaving behind positively charged donor ions, and holes moving to the n-type region, leaving behind negatively charged acceptor ions. The displacement of the carriers creates an electric field which in steady-state prevents further diffusion, while creating a potential across the p-n junction. As a result of the potential, free carriers are driven away from the junction resulting in a volume lacking in free charge carriers called the depletion region.

Applying a positive external potential to the positive side of the junction (forward

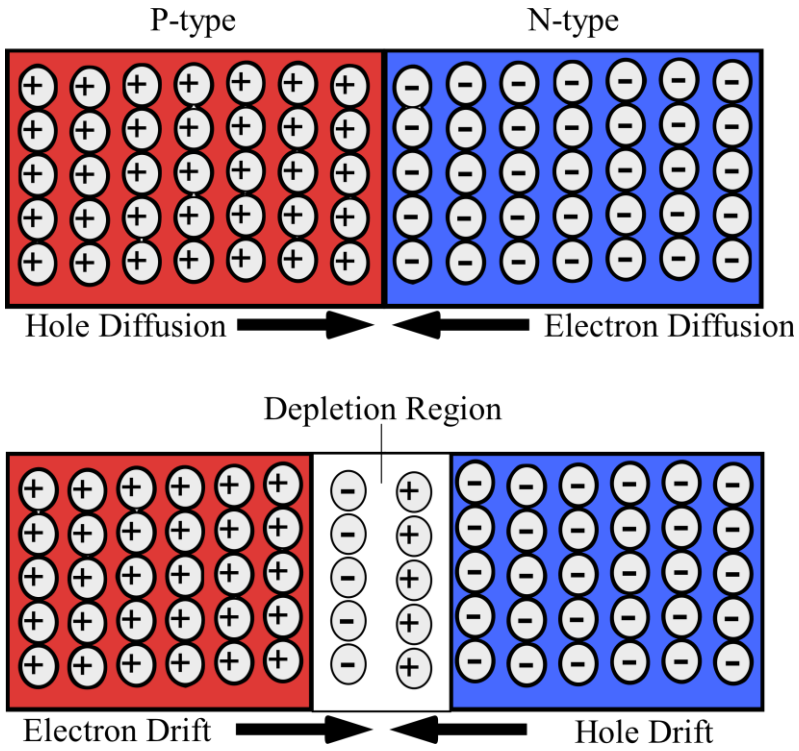

Fig. 2.1 Schematic representation of the formation of the depletion region in a p-n junction.

biasing the junction) reduces the potential barrier allowing the flow of a diffusion current. Applying a positive potential to the negative side of the junction increases the potential barrier. The ideal diode equation describing current flow through an ideal p-n junction is given by:

$$I = I_s(e^{qV/k_bT} - 1) \tag{2.1}$$

where I_s is the saturation current, q is the elementary charge, V is the applied potential, k is the Boltzmann constant and T is the temperature of the junction.

A p-n junction can function as a photodetector due to the built-in electric field in the depletion region which allows for charge separation of electron-hole pairs generated by an incident photon exciting an electron from the valence to conduction band, as shown

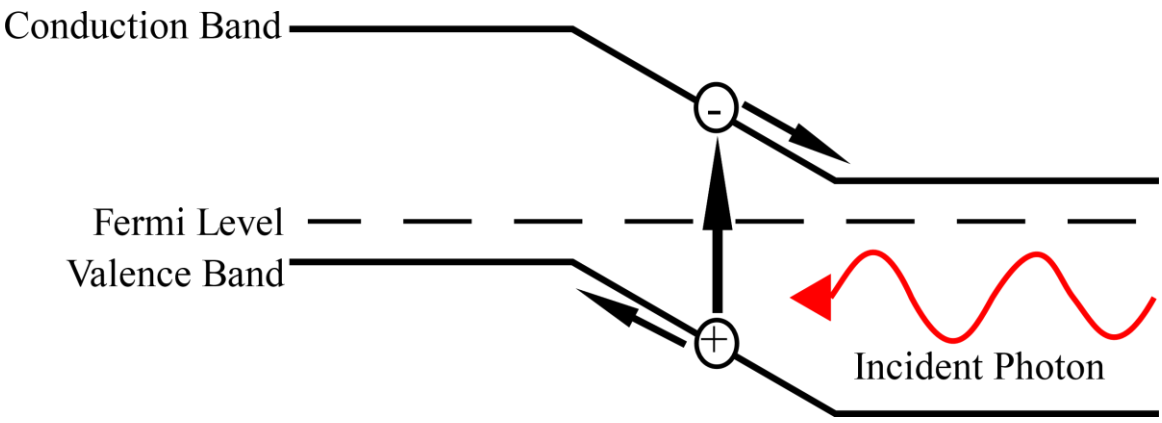

Fig. 2.2 Schematic Diagram of the band gap of the p-n junction with the creation of an electron-hole pair via electron excitation due to photon absorption.

in Fig. 2.2. As a result a p-n junction can be used as a photodetector with photocurrent generated from absorption occurring in the depletion region, or within a diffusion length of the depletion region. The efficiency of the detector thus requires the optimization of the depletion width W_d which is given by:

$$W_d = \left(\frac{2\varepsilon (V_o - V)}{q} \left(\frac{1}{N_a} + \frac{1}{N_d} \right) \right) \tag{2.2}$$

where ε is the electric permittivity, V_o is the built-in junction potential, V is the applied potential, and N_a and N_d are the acceptor and donor carrier concentrations respectively. The depletion width is required to be large enough to absorb the majority of incident light. While it is possible to increase the width of the depletion region by altering the carrier concentrations and applying an increasing potential bias, a more common method of increasing its width and thus efficiency is to introduce an intrinsic (undoped) region between the p and n regions allowing for a larger volume where carrier drift can take place. This type of device is known as a p-i-n detector.

2.1.2 Dark current

Dark current is the leakage current that the photodiode experiences when under reverse bias, in the absence of illumination. It is often caused by defects in the lattice or at the surface of the device which create localized states in the band gap allowing for the thermal generation of charge carriers. Low dark current densities are highly desirable as not only does an increase in dark current lead to an increase in power consumption of a detector it also leads to a decreased signal to noise ratio (SNR) and ultimately higher bit error rates. For a p-i-n detector the SNR is defined using the following:

$$\left. \frac{S}{N} \right|_{power} = \frac{i_p^2}{\left\langle i_s^2 \right\rangle + \left\langle i_T^2 \right\rangle} \tag{2.3}$$

where i_p is the rms photocurrent, and i_s is the shot noise and i_T is the thermal noise. Using the definition for each we obtain:

$$\left.\frac{S}{N}\right|_{power} = \frac{(1/2)(q\eta P_{opt}/h\nu)^2}{2q(I_P + I_B + I_D)B + \frac{4k_bTB}{R_{eq}}} \tag{2.4}$$

where I_p is the average photocurrent for a given signal, I_B is the background current and I_D is the dark current, k_b is the Boltzmann constant, T is the temperature, B is the bandwidth and R_{eq} the equivalent resistance is given by the following:

$$\frac{1}{R_{eq}} = \frac{1}{R_j} + \frac{1}{R_L} \tag{2.5}$$

where R_j is the resistance of the junction, and R_L is the external load resistance. From this equation it can be seen that in order to maximize the SNR, quantum efficiency and the equivalent resistance should be enhanced whereas background current and dark current must be minimized. In the context of Si photonics, the dark current for Ge detectors has been thoroughly examined and determined to be a result of bulk leakage current via lattice defects and surface leakage current. Thus, the growth of high quality Ge and passivation of its surface are key elements of processing with the goal of obtaining dark currents less than 1 μA to obtain a suitable SNR.

2.1.4 Quantum efficiency and responsivity

Quantum efficiency is a measure of charge carriers generated per number of photons. While quantum efficiency is most often defined as the external quantum efficiency which is the number of electron-hole pairs generated and collected per the number of the incident photons, it can also be defined as the internal quantum efficiency which is the number of electron-hole pairs which are collected after photons are absorbed. While both definitions have their uses, external quantum efficiency is used

more often as internal quantum efficiency is an idealized version. For a waveguide integrated (WGI) detector, the external quantum efficiency η_{ext} is given as [2]:

$$\eta_{ext} = \Gamma \frac{\alpha_{IB}}{\alpha}(1 - e^{-\alpha L})\eta_{in} \tag{2.6}$$

where Γ is the modal confinement α_{IB} is the intraband loss coefficient, L is the length of the detector, η_{in} is the internal quantum efficiency and α is the loss coefficient which is defined as:

$$\alpha = \Gamma \alpha_{IB} + \Gamma \alpha_{FC} + \alpha_s \tag{2.7}$$

where α_{FC} is the free carrier absorption loss coefficient and α_s is the scattering loss coefficient. The equation for a normal-incidence (NI) detector is very similar although one must consider the reflections from the surface, the modal confinement does not play a role and L no longer represents the length of the detector but the width of the intrinsic region for a p-i-n detector or the depletion width for a p-n detector.

Another common way of defining the efficiency of a photodetector is through the use of responsivity which is the ratio of photocurrent I_P generated as compared with the incident optical power P_{opt}. For a given detector the responsivity R is defined using the following:

$$R = \frac{I_P}{P_{opt}} = \frac{\eta_{ext} q}{h\upsilon} \tag{2.8}$$

where q is the elementary charge h is Planck's constant and υ is the frequency of the light. This expression can be reduced to the following:

$$R = \eta_{ext} \frac{\lambda}{1.24} \tag{2.9}$$

where λ is the incident wavelength in microns and the responsivity is given in A/W. For an experimental setting, responsivity is more used than quantum efficiency as its calculation is sufficiently simple.

2.1.5 Light coupling schemes

There are several different light coupling schemes which are used for photodetectors. The ones covered in this section will be NI, WGI and resonant cavity enhanced (RCE) detectors. Before discussing these schemes, a brief overview of the speed of response of detectors will be given.

For a p-i-n detector there are several properties that limit speed of operation: transit time, the RC time constant and time delay from carrier diffusion. In any given p-i-n detector the carriers generated in the intrinsic region will move at a given drift velocity $v_d = \mu E$ where μ is the mobility of the charge carrier and E is the electric field. As the electric field is increased in strength the drift velocity will eventually saturate and further increases will result in collisions from charge carriers transferring energy to the crystal lattice. For a detector which is limited by the transit time the 3-dB small-signal bandwidth is given by the following:

$$f_{3dB} = \frac{2.4}{2\pi t_r} \tag{2.10}$$

where t_r, the transit time of charge carriers is given by:

$$t_r = \frac{v_s}{W_D} \tag{2.11}$$

where v_s is the saturation velocity and W_D is the depletion width for a p-n detector or the length of the intrinsic region in a p-i-n detector.

NI detectors, an example of which is shown in Fig 2.3 [3], where light is incident on the top or bottom of the detector, are often favoured due to ease of fabrication. A main disadvantage of these detectors is that they suffer from a trade-off between quantum efficiency and response time. An increase in the speed of response through reduction of the intrinsic region results in a reduction in the quantum efficiency of the detector. For example, assuming a detector with 100% internal quantum efficiency, and using a charge carrier velocity v=6x10^6 cm/s and absorption coefficient of α=4000 cm^{-1} (consistent with Ge at 1550 nm with an intrinsic region of 0.6 μm), the 3-dB bandwidth is 40 GHz and the external quantum efficiency is limited to 25%.

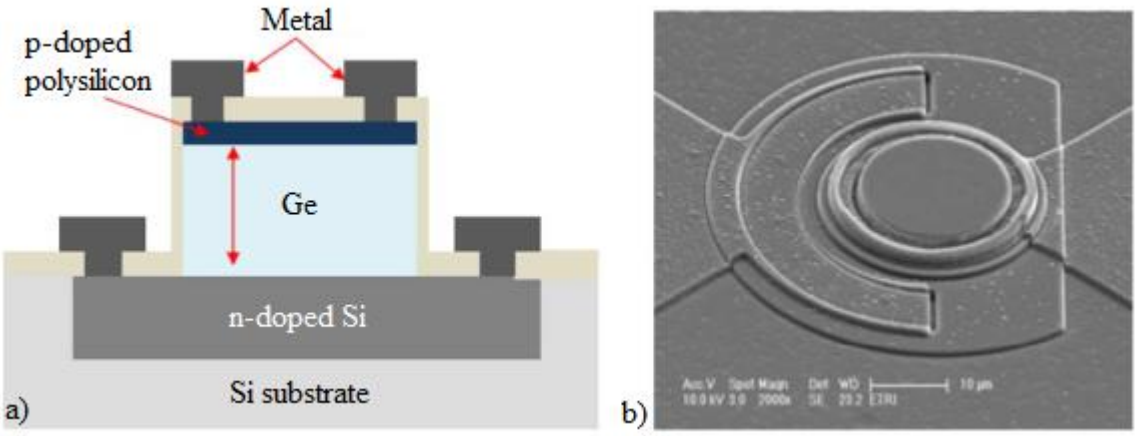

Fig. 2.3 a) Schematic diagram, and b) top view SEM of a NI detector. Figure reproduced from [3] © 2009 IEEE.

In order to enhance the efficiency while maintaining speed of response there has been some use of resonant cavity enhanced detectors in which light is trapped between two highly reflective facets allowing for increased absorption and quantum efficiency.

These detectors also have the advantage that if a Bragg-grating reflector is used, only a specific wavelength of light will be reflected which is ideal for wavelength de-multiplexing systems. An example of this is shown in Fig. 2.4 where Dosunumu et al. used a double SOI structure to create a reflective coating for the 1300-1600 nm range of

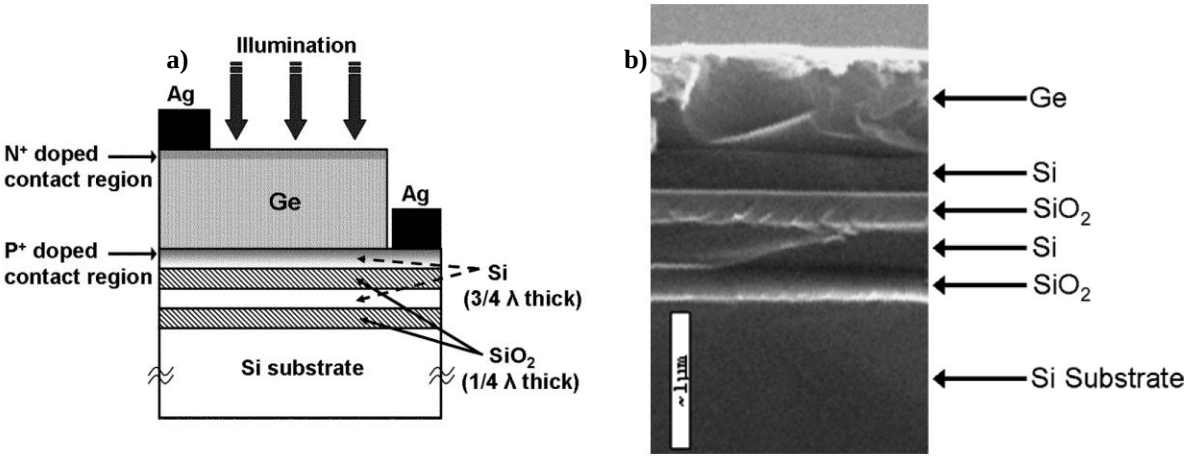

Fig. 2.4 a) Schematic diagram, and b) cross-sectional SEM of a resonant cavity enhanced Ge-on-Si detector. Figure reproduced from [4] © 2004, IEEE.

wavelengths. Doing so they were able to obtain a quantum efficiency of 76% using a layer of only 860 nm [4].

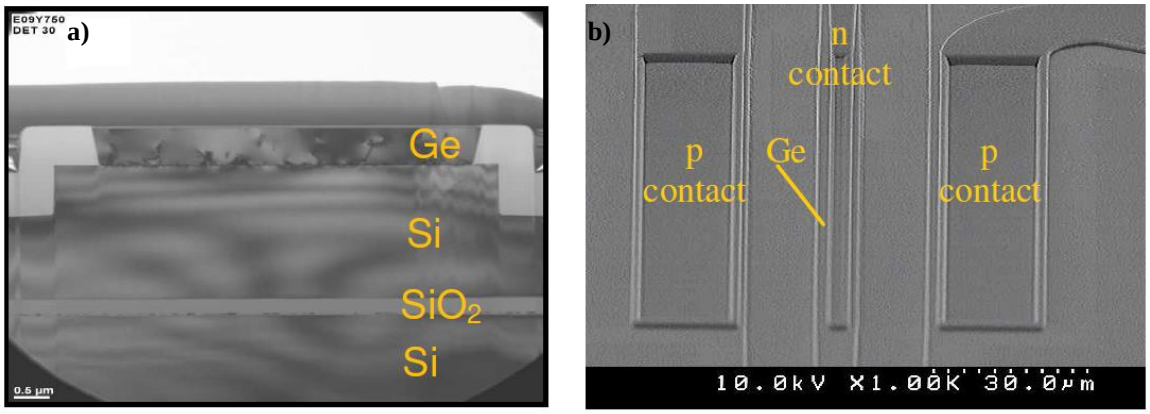

Fig. 2.5 a) Cross-sectional and b) top-view SEM of a Ge-on-Si waveguide detector. Figure reproduced from [5] © 2009 Optical Society of America

Waveguide detectors, by contrast, do not suffer from this trade-off of speed and efficiency as the quantum efficiency is related to the length of the detector as opposed to the width of the intrinsic region. An example of a waveguide detector is shown in Fig. 2.5[5]

2.2 Epitaxial growth of Ge on Si

The epitaxial growth of Ge on Si has been an area of focus for research in optical communication applications for many years [6]. The direct bandgap, which is the energy required by a photon to excite an electron to the conduction from the valence band at the same k-space value, of Ge is 0.8 eV which corresponds approximately to 1550 nm making Ge suited for photodetection in the *O, C* and *L* communication bands from 1.3 to 1.6 μm [7] and avoids the cost issues associated with bonding III-V's with Si [8]. Additionally, Ge supports superior hole, and electron mobility compared with Si (Ge has a hole and electron mobility of l900 and 3900 $cm^2V^{-1}s^{-1}$ respectively compared with 430 and 1600 $cm^2V^{-1}s^{-1}$ for Si[8]), and Ge can be used potentially as a template for growth of III-V semiconductor material [9]. However, the direct growth of Ge on Si can be a difficult process due to the mismatch of lattice spacings- the lattice constant of Ge is 5.65 Å whereas the lattice constant for Si is 5.43 Å, a relatively large mismatch of 4%. Initial work [10] found that while the planar, defect free growth of Ge on Si was possible for layer thicknesses below a critical value (approximately 3 monolayers), for thicker films there is the formation of threading dislocation defects which leads to serious device performance problems such as high leakage currents and increased recombination of

electron-hole pairs, which decreases the signal to noise ratio and increases the power consumption of the detectors. These defects also lead to the formation of islands due Stransky-Krastanov growth as shown in Fig. 2.6 which makes the material unsuitable for CMOS processing.

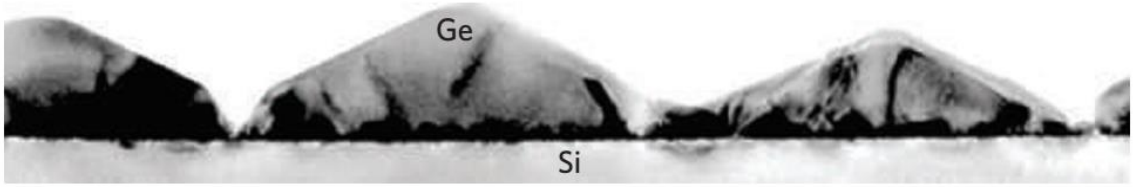

Fig. 2.6 Cross sectional TEM of Stransky-Krastanov growth of Ge on Si. Figure reproduced from [10] © 2010 NPG

In this section some methods which have been used to overcome problems associated with Ge growth on Si will be explored and interesting recent developments in the use of these techniques is reviewed.

2.2.1 Ge growth via SiGe buffer layers

The early attempts at growing planar Ge used the growth of an initial SiGe buffer layer with the concentration of Ge gradually increased to reduce the strain caused by the large lattice mismatch between Ge and Si. The first experimental demonstration of this method was by Luryi et al. in 1984 [11]. In this work, nine layers of 200 nm of $Si_{1-x}Ge_x$ was grown at 550 ºC via molecular beam epitaxy (MBE) on Si, with the Ge concentration increasing from x = 0.1 to x=1. A pure Ge structure was then grown on the buffer consisting of a 1.25 μm n^+-Ge layer, a 2 μm intrinsic Ge layer and a 1.5 μm p^+ Ge layer. The fabricated detector had a quantum efficiency of 40% with no applied bias measured using a 1310 nm laser source. However, there was an observed dark current of 90 μA at

0.6 V reverse bias for a detector with a 50 μm diameter. The dark current was subsequently reduced by a factor of four through the use of post-growth annealing at 650 to 700 °C.

A lower number of dislocation-type defects, ~ 10^6 cm^{-2}, in a grown Ge layer was demonstrated in subsequent work by Currie et al. in 1998 [12]. They determined that the surface roughness on each buffer layer increased the number of dislocations in

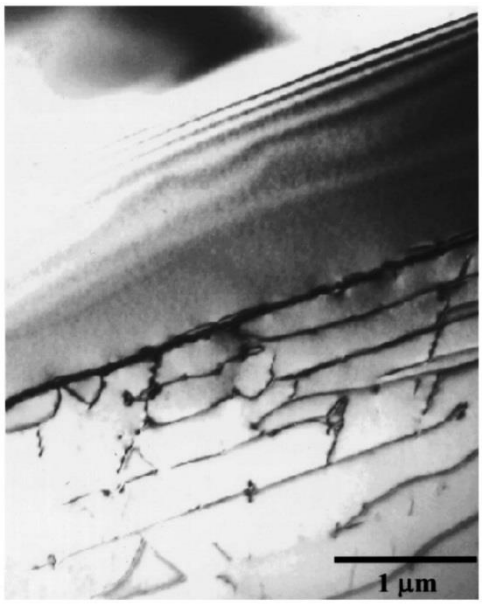

Fig. 2.7 Cross sectional TEM of Ge grown on a SiGe buffer layer. Figure reproduced from [12] © 1998 AIP.

subsequent layers, causing a pile-up of dislocations. Therefore, they introduced a chemical mechanical polishing (CMP) step in the growth process to reduce surface roughness and thus the overall number of grown-in defects. In this work 200 nm thick SiGe layers were grown via ultra-high vacuum chemical vapour deposition (UHV-CVD) where the concentration of Ge was increased by 2% for each layer. The first 5 μm was grown at 750 °C and 250 mTorr, until the Ge concentration reached 50%, at which point

a 1.5 μm cap layer of SiGe with 50% Ge was grown, 500 nm of which was then removed using CMP in order to reduce surface roughness. The buffer layer growth was resumed until the Ge concentration reached 92%. This was followed by the growth of a 1.5 μm cap layer of pure Ge. Through analysis of the sample via X-ray diffraction, cross-sectional TEM, and atomic force microscopy (AFM) the authors found that the layers grown in this way had reduced threading dislocations, by an order of magnitude as compared with samples grown without the CMP step. A TEM cross-section of the structure is shown in Fig. 2.7. Using this same method Samavedam et al.[13] demonstrated a Ge detector with a 250 μm mesa which was found to have a dark current of <1 μA up to a 3 V reverse bias, with a corresponding responsivity of 0.133 A/W for a 1310 nm laser source (measured under zero bias). No high-speed measurements were reported but based on capacitance measurements it was estimated that the -3 dB point for such a detector would be approximately 2.35 GHz.

These results were then improved upon by Oh et al.[14] who fabricated a detector with interdigitated surface contacts, by growing 1 μm of Ge on a 10 μm buffer layer using low-energy plasma enhanced chemical vapour deposition (LEP-CVD). The Ge layer was found to have a threading dislocation density of 10^{-5} cm^{-3}, however due to the design of the interdigitated contacts the dark current was found to be 3.2 μA and 5.0 μA at 3 and 5 V reverse bias respectively with a responsivity of 0.51 A/W with no bias for a 1310 nm laser source and associated electrical bandwidth of 3.8 GHz.

While the results described above are three examples of the growth of high quality Ge-on-Si, the thickness of the buffer layers makes them unsuitable for high speed

operation in the 10's GHz. Therefore, subsequent studies of Ge detectors with SiGe buffer layers focused on different growth schemes to allow for much thinner buffer layers. The first example was demonstrated by Luo et al. [15] who were able to trap a significant number of defects at the heterojunction interface by optimizing the Ge concentration. In this work they were able to cause the dislocation defects to bend and terminate with other dislocation defects rather than have the dislocations travel upwards. This technique was then used for the formation of a detector by Huang et al. [16] growing a 0.6 μm layer of SiGe with 55% Ge followed by a 0.4 μm layer of SiGe with 65% Ge follow by a 2.5 μm thick layer of Ge using UHV-CVD. As a result of this optimization scheme they were able to develop a detector with responsivities of 0.37 A/W and 0.57 A/W at 0 V and 2 V reverse bias respectively for a 1310 nm laser source that could operate at 8.1 GHz at 10 V reverse bias. While the dark current density was found to be higher for devices fabricated using this growth scheme, due to the relatively small size of the device (mesas were fabricated with a 12 μm radius) the dark current was found to be 1.07 μA at 10 V reverse bias. This was then improved upon to increase the responsivity and high-speed operation by modifying the growth scheme such that a 1.7 μm Ge layer was grown on a 0.28 μm layer of SiGe with 58% Ge and a 0.18 μm layer of SiGe with 42% Ge. For a device with a 10 μm radius they determined the responsivity to be 0.62 A/W at 0.1 V reverse bias and found that the detector could operate at 21 GHz at 10 V reverse bias for a 1310 nm laser source. They also examined the detector using a 1550 nm laser source and determined the detector had a responsivity of 0.26 A/W and could operate at 17 GHz at 10 V reverse bias [17]. The lower bandwidth is attributed to the

reduced absorption coefficient at 1550 nm resulting in fewer electron hole pairs generated near the SiGe/Ge interface as compared with 1310 nm. The dark current was measured to be 2.07 μA at 10 V reverse bias which was attributed to the small size of the mesa.

While all of the above are demonstrations of high-quality growth of Ge on Si using SiGe buffer layers, Ge integration with Si optical circuits in the paradigm of Si photonics requires direct growth of Ge on Si waveguides with light interacting with the Ge via evanescent coupling. As a result, even buffer layers of only a few 100 nm's are unsuitable for use in today's state-of-the-art devices and more sophisticated growth techniques are required.

2.2.2 Low-temperature/high-temperature growth

In 1998 it was proposed and demonstrated by Colace et al. [18], that a two-step process leads to low defect density Ge-on-Si. The first step is a short, low temperature growth of Ge to supress the formation of islands. The second is a longer, higher temperature growth which, as a result of the previous thinner layer, is no longer influenced by the lattice mismatch between Si and Ge. Growth took place using UHV-CVD growing a 50 nm layer at 330 °C followed by a growth of a 500 nm layer of Ge at 600 °C. They were able to fabricate a photodetector with a responsivity of 0.24 A/W at 1 V reverse bias for a 1310 nm laser source.

It was subsequently demonstrated by Kimerling et al. [19] that through the use of a post-growth, cyclic thermal annealing of the Ge between 900 and 780 °C, the number of threading dislocations could be reduced from 9.5×10^8 cm^{-2} to 2.3×10^7 cm^{-2}. Fig. 2.8 shows an example of the improvement in quality of the Ge after using cyclic thermal

annealing. This method was then adopted by Colace et al. [20] where they demonstrated an improvement in responsivity to 0.89 A/W for a 1310 nm laser source and 0.75 A/W for a 1550 nm laser source.

The success of this technique has led to the development of a low-temperature/high temperature growth scheme for Ge-on-Si using MBE [21] and Reduced-pressure chemical vapour deposition (RPCVD) [22]. With the elimination of the need for a thick buffer, photodetectors have increased speeds of operation, with 3-dB bandwidths of up to 38.9 GHz demonstrated for NI detectors grown in this way [23].

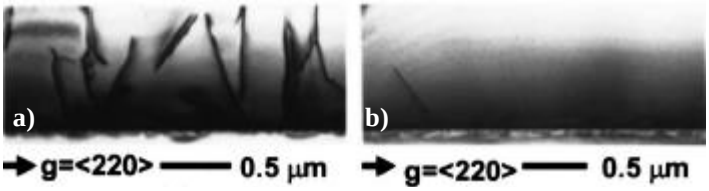

Fig. 2.8 Cross sectional TEM of Ge grown using the low and high-temperature annealing a) before and b) after cyclic thermal annealing. Figure reproduced from [19] © 1999 AIP.

Another advantage of this technique, as compared with the SiGe buffer technique, is its suitability for use in WGI devices. The relatively thin Ge structure used in the evanescent coupling geometry has produced responsivities of up to 1 A/W for 1550 nm sources with speeds of operation of 42 GHz [24].

2.2.3 Poly-crystalline Ge

The low-temperature/high-temperature growth scheme works well to produce high quality Ge-on-Si. However, it is a time consuming and challenging process. In addition to this, the high temperature step and further annealing can make the process incompatible with some standard CMOS processes. Therefore, it was proposed by Masini et al. [25] to use a low temperature evaporation of polycrystalline Ge. Using thermal

evaporation, 200 nm of Ge was deposited on Si at temperatures ranging from 25 °C to 400 °C. Analyzing their samples with Raman spectroscopy it was found that poly-crystalline Ge could be deposited at temperatures as low as 300 °C, with the samples produced at lower temperatures being amorphous. Using polycrystalline Ge in a NI detector, high-speed operation at 2.55 Gbit/s [26] and monolithic integration of CMOS devices was demonstrated [27], [28]. However, the obtained responsivity of 0.016 A/W and of 0.005 A/W for a 1310 and 1550 nm source respectively is by comparison to other Ge growth techniques very low due to the poor quality of the material. This original work was then improved upon by implementing a WGI detector and maximizing the overlap of the mode with the active region close to the Si/Ge interface allowing for a reduction in carrier recombination [29–32]. Using these WGI detectors, responsivities ranging from 0.1 A/W to 0.3 A/W and high-speed operation at 2.5 Gbit/s were demonstrated. More recent work done by Sorianello et al. [33], [34] on thermal deposition has demonstrated the growth of crystalline Ge on Si for temperatures ranging from 250 to 500 °C. In particular, samples grown at 300 °C and doped using a spin coating of phosphorus were used to fabricate a NI detector which was found to have a responsivity of 0.1 A/W at 1 V reverse bias for a 1.55 μm laser source. While these results are inferior compared to high quality Ge described in the previous two sections, the low cost and relative simplicity of this technique may make it suitable for some applications.

For clarity the characteristics of the detectors which have been discussed in this section and the previous two sections are summarized in Table 2.1

Table 2.1 Summary of Ge detector growth and detector characteristics described in this work. *Voltages recorded are reverse bias voltage. *Responsivity is calculated from reported quantum efficiency and eqn. (2.9). †Estimated 3 dB bandwidth.

Growth Process	Tool	Growth Scheme	Light coupling Scheme	Dark Current*	Responsivity	3-dB Bandwidth (GHz)	Ref.
SiGe Buffer	MBE	1.8 μm buffer layer with x=0.1 to x= 0.9, 4.75 μm Ge layer grown at 550 °C	NI	90 μA at 0.6 V	0.43 A/W** at 1310 nm	-	[11]
SiGe Buffer	UHV-CVD	9.2 μm buffer layer graded at 10% Ge/μm to 92%, 2.8 μm Ge layer, grown at 750/550 °C. CMP included during growth	NI	0.5 μA at 3 V	0.133 A/W at 1310 nm	2.35†	[13]
SiGe Buffer	LEP-CVD	10 μm buffer layer	NI	3.2 μA at 3 V	0.51 A/W at 1310 nm	3.8	[14]
SiGe Buffer	UHV-CVD	0.6 μm 55% Ge and 0.4 μm 65% Ge buffer grown at 500 °C annealed at 750 °C, 2.5 μm Ge layer grown at 400 °C	NI	1.07 μA at 10 V	0.57 at 1310 nm	8.1	[16]
SiGe Buffer	UHV-CVD	0.18 μm 42% Ge and 0.28 μm 58% Ge grown at 500 °C, 50 nm Ge layer at 350 °C and 1.7 μm Ge layer grown at 600 °C	NI	2.41 μA at 10 V	0.62 A/W at 1310 nm, 0.28 at 1550 nm	21.5 at 1310 nm, 17 at 1550 nm	[17]
LT/HT	UHV-CVD	50 nm at 300 °C, 500 nm at 600 °C	NI	-	0.24 A/W at 1310 nm	5†	[18]
LT/HT	UHV-CVD	60 nm at 350 °C, 4 μm at 600 °C. Ten cyclic anneal steps between 900 and 780 °C	NI	13 μA at 1 V	0.89 A/W at 1310 nm, 0.75 A/W at 1550 nm	2.5	[20]
LT/HT SiGe Buffer hybrid	MBE	20 nm 40% Ge at 120 °C, 40 nm 40% Ge at 550 C, 1 μm Ge at 550 °C	NI	0.2 μA at 2 V	-	38.9	[23]
LT/HT	UHV-CVD	50 nm at 375 °C, 1400 nm at 600 °C. Ten cyclic annealing steps between 900 and 780 °C	RCE	-	0.73 A/W** at 1540 nm	6.7	[4]

Table 2.1 Continued from previous page. Summary of Ge detector growth and detector characteristics described in this work. *Voltages recorded are reverse bias voltage. *Responsivity is calculated from reported quantum efficiency and eqn. (2.9). †Estimated 3 dB bandwidth.

Growth Process	Tool	Growth Scheme	Light coupling Scheme	Dark Current*	Responsivity	3-dB Bandwidth (GHz)	Ref.
LT/HT	UHV-CVD	30 nm at 375 °C, 830 nm at 600 °C. Ten cyclic annealing steps between 900 and 780 °C	RCE	-	0.95 A/W** at 1550 nm	25	[7]
LT/HT	RPCVD	40 nm layer at 400 °C, 390 nm layer at 730 °C	WGI	30 μA at 4 V	1 A/W at 1550 nm	42	[24]
Poly-Ge	Thermal Evap.	120 nm at 300 °C	NI	0.4 μA at 1 V	0.016 at 1310 nm, 0.05 A/W at 1550 nm	5.2	[26]
Poly-Ge	Thermal Evap.	120 nm at 300 °C	WGI	1.5 μA at 30 V	0.3 A/W at 1550 nm	5	[32]

2.2.4 Ge condensation

The Ge condensation technique is a method whereby Ge accumulates through the removal of Si from a low-Ge concentration SiGe thin film, via thermal oxidation. Under the appropriate conditions the Ge is rejected from the growing oxide resulting in an increasing Ge content. Of importance, the resulting SiGe layer is single crystal in nature. While most recent publications have demonstrated this technique through oxidation of SiGe epitaxially grown on SOI, the earliest work using this technique was performed by Fathy et al. [35], [36] with the Ge introduced via high-fluence implantation of Ge into bulk Si. In that case Si samples were implanted with Ge^{+} ions with doses of $1x10^{16}$ cm^{-2} and $1x10^{17}$ cm^{-2} and oxidized at temperatures ranging from 800 to a 1000 °C in a steam

environment. The samples were then analyzed using Rutherford backscattering (RBS) and TEM and it was found that high Ge content SiGe (Ge fraction = 82%) could be achieved, with the thickness ranging from 3 nm for samples implanted with a dose of

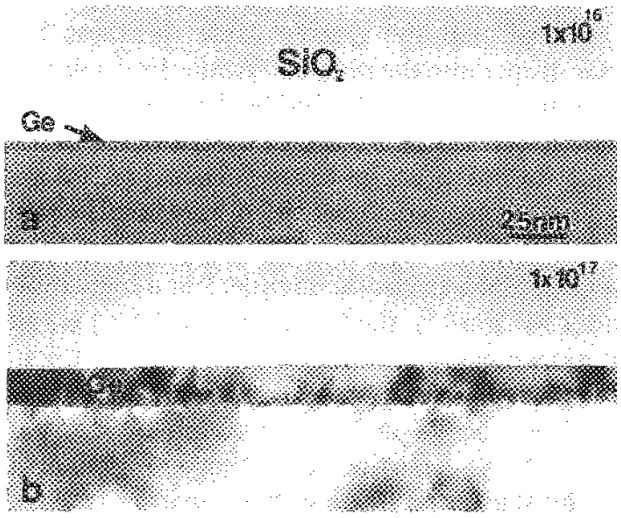

Fig 2.9 Cross sectional TEM of Ge grown via oxidation with an implantation does of a) $1x10^{16}$ cm^{-2} and b) $1x10^{17}$ cm^{-2}. Figure reproduced from [36] © 1987 AIP.. The figure has been scanned from the original paper and as a result is of low quality.

$1x10^{16}$ cm^{-2} to 20 nm for samples implanted with a dose of $1x10^{17}$ cm^{-2}. An image of these layers is reproduced in Fig. 2.9.

Furthermore, it was found that during oxidation there was a marked enhancement in the oxidation rate as compared with unimplanted Si which could not be explained by enhancement due to crystal lattice damage. Initially the pile up of Ge at the oxide/Si interface was attributed to a lack of solubility of Ge in SiO_2, as well as the slow diffusion of Ge in Si as compared with the rate of oxide growth allowing for the oxide/Si interface to move faster than the Ge could diffuse into the Si. While, the enhanced growth rate of the oxide was attributed to the weaker bond energy of Si-Ge as compared with the bond energy of Si-Si. While both of these statements are true, they do not completely reflect

the growth process, especially as mixed Si and Ge oxides have been observed previously. Therefore, subsequent publications on the oxidation of SiGe have devoted much effort to a complete description of the microscopic growth process [37–43]. From these studies it has been determined that the enhancement in the oxidation and the lack of Ge in the oxide is attributed to three key components: (1) point defects at the oxide interface, (2) the weakened bond strength of Si-Ge as compared with Si-Si and (3) the instability of GeO_2 where if the flux of Si to the oxidation interface is higher than that of oxygen the following reaction takes place:

$$Si + GeO_2 \rightarrow SiO_2 + Ge \tag{2.12}$$

Subsequent demonstrations of Ge condensation using high-fluence implants of Ge by Holland et al. [44], [45] have shown that it is possible to observe enhancement in oxidation rate with both wet and dry oxidation, and that it is possible to achieve thin films that almost entirely consist of Ge. The dose, energy of implant, and temperature/conditions of the oxidation play a significant role in the composition of the layer.

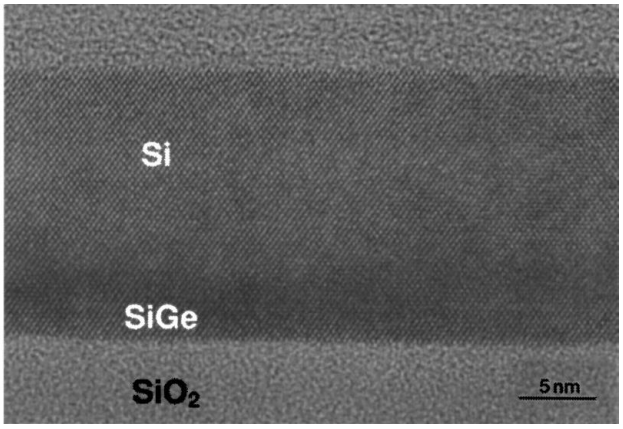

Fig 2.10 Cross sectional TEM of Si grown on SiGeOI formed via a condensation process. Figure reproduced from [47] © 2001 AIP.

These previous examples of condensation were performed using bulk Si as the starting substrate. When the condensation technique is performed on SOI the buried oxide layer can be used as a diffusion barrier for the Ge (due to the low solubility and low diffusion coefficient of Ge in SiO_2) resulting in a thin layer of pure Ge being grown. While this technique has not been used to fabricate a photodetector prior to the work described in this thesis, the ease of manufacture and compatibility of the process with photonic/electronic device fabrication makes this technique of great interest. In addition, GeOI fabricated by condensation has been used as a template for growth of GaAs [46] opening a method for straightforward integration of Si and III-V devices. The first demonstration of growth on SOI was performed by Tezuka et al. [47] in which a 9 nm layer of SiGeOI with 56% Ge was produced by oxidizing a 67 nm layer of SiGe with a Ge content of 8% originally grown on SOI via UHV-CVD, this was then followed by the growth of Si on the SiGe, the resulting layers are shown in Fig. 2.10. It was then demonstrated that this technique could be used to generate Ge-on-insulator (GeOI) as

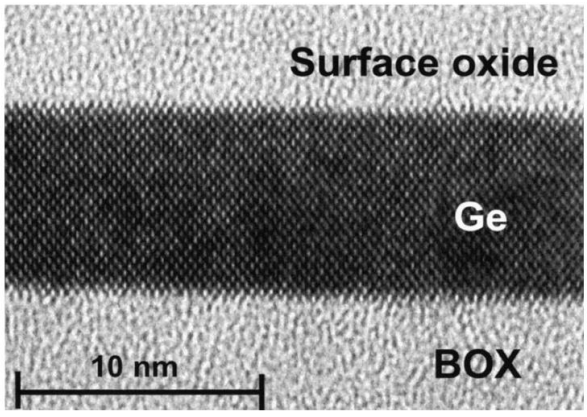

Fig 2.11 Cross sectional TEM of GeOI formed via Ge condensation process. Figure reproduced from [48] © 2003 AIP.

shown in Fig. 2.11 [48]. Analyzing the sample with Raman spectroscopy it was found that the sample was essentially pure Ge, and that the layer was compressively strained.

Subsequent publications on this topic have analyzed the mechanisms of formation of the Ge layer specifically with a focus on loss mechanisms for Ge i.e. oxidation, and diffusion into both oxide layers [49], [50], as well as the formation of defects in relation to strain relaxation such that the number of defects and strain can be efficiently controlled via the Ge content, thickness, and oxidation temperature of the process [51–59].

2.2.5 Physical deposition methods

High quality epitaxial techniques such as CVD and MBE currently dominate the growth of Ge-on-Si. However, there still has been a considerable amount of research performed on physical vapour deposition (PVD) techniques as the associated tools are often low cost and require a lower thermal budget. Examples of epitaxial grown crystalline Ge on Si via electron beam and thermal evaporation were demonstrated on Si as early as 1982 by Vitali et al. [60].

Work on sputter deposition of Ge-on-Si can also be traced back to 1982 where Bajor et al. [61] used RF sputtering to deposit 1.5 μm thick Ge films onto Si at 470 °C. To reduce the formation of defects via strain relaxation, they used low-energy ion bombardment to grade the composition of the Ge. Using X-ray diffraction and electron channelling spectra the films were confirmed to be crystalline. More recent work has been performed with both pulsed DC-magnetron sputtering and continuous DC-magnetron sputtering with both demonstrating the growth of crystalline Ge on Si [62], [63]. For pulsed DC magnetron sputtering it was found that samples deposited at 370 °C

were crystalline and that a further anneal at 400 °C could be used to improve crystalline quality. For continuous DC magnetron sputtering it was found that the growth regime of the Ge switched from amorphous to crystalline at 380 °C with islanding being observed at 410 °C as shown in Fig. 2.12. As both of these techniques are scalable to industrial levels and can incorporate doping via the sputtering target, sputter deposition of Ge offers an interesting prospect for the fabrication of devices.

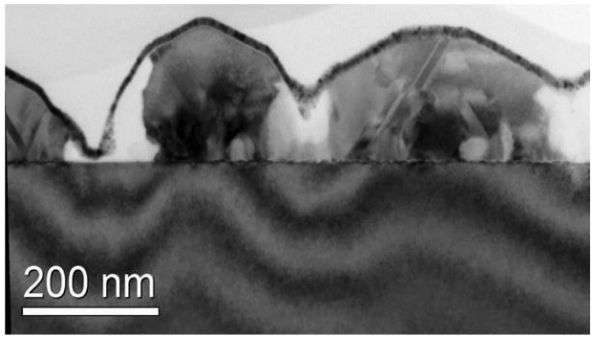

Fig 2.12 TEM of Ge grown on Si via DC magnetron sputtering. Figure reproduced from [63] © 2013 AIP.

2.2.6 Tensile strain and bandgap shrinkage

Due to the difference in the thermal expansion coefficients of Ge and Si, samples annealed at high temperature and then cooled result in a tensile strain build-up in the Ge layer. This is an advantageous effect for photodetectors as tensile strain shrinks both the direct and indirect bandgap of a material, which is of interest for extending the detection band edge of Ge devices [64]. This was first documented by Kimerling et al. [65] where they calculated that a 0.2% tensile strain corresponded to a difference in band gap energy of 0.03 eV. This resulted in an enhancement in longer wavelength detection such that the absorption coefficient of the Ge-on-Si was increased by a factor of 2 from that of bulk Ge. Additionally, the direct bandgap will shrink faster than the indirect bandgap allowing

Ge to be converted to a direct band material given sufficient tensile strain which is of interest for the development of a group IV laser [66]–[68].

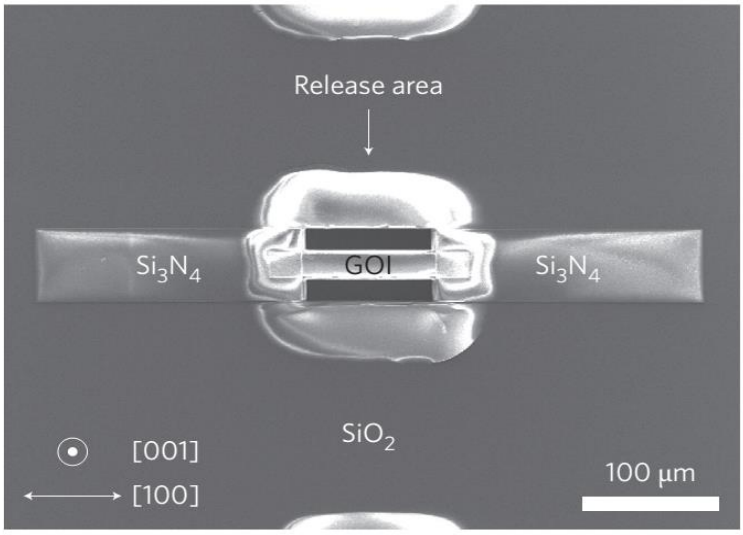

Fig 2.13 SEM of a nanowire bridge structure with Si_3N_4 stressors formed on GeOI. Figure reproduced from [69] © 2012 NPG.

Several techniques have been developed in order to enhance the strain which occurs in Ge-on-Si structures, one of the most prominent being the use of Si_3N_4 stressors with nanowire bridge structures, first demonstrated by Jain et al. using GeOI [69], as shown in Fig 2.13. In this process the Ge is etched away except for a thin nanowire, Si_3N_4 is then deposited onto either end of the Ge nanowire which is then released by etching through the BOX and then etching the Si underneath. This allows the strained Si_3N_4 pads to relax, transferring the stored energy into the nanowire resulting in enhanced tensile strain up to 1.5% and an enhanced photoluminescence by a factor of 260 over bulk Ge.

Similar trends have been reported without the use of Si_3N_4 stressors for both GeOI [70] and Ge grown on SOI [71] as shown in Fig. 2.14. Using this technique, enhancements of up to 5.7%, which is enough to cause Ge to become a direct band

material, have been demonstrated [72]. The nanowire release technique has resulted in an optically pumped Ge laser operating at 83 K [73]. The disadvantage to the enhancement of tensile strain for a Ge laser is the red shifting of the wavelength outside of currently used communication bands. However, with the rise of thulium doped fiber amplifiers there is potential for highly tensile strained Ge at higher wavelengths for use as both a photodetector and a laser source.

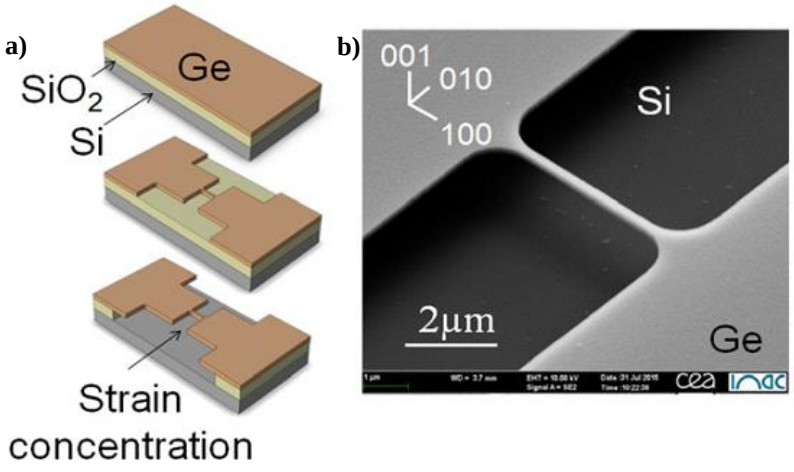

Fig 2.14 a) Schematic diagram of the processing for a Ge nanowire bridge and b) SEM of a Ge nanowire bridge. Figure reproduced from [70] © 2106 AIP.

2.3 Fabrication techniques used in this work

This section reviews the processing techniques used during the research that led to this thesis. For further background, the reader is referred to the text *Silicon VLSI technology: fundamentals, practice, and modeling* by Plummer, Deal and Griffin [74].

2.3.1 Ion implantation

Ion implantation has been one of the key components of the semiconductor industry since the 1970's. It uses are wide ranging from the formation of compound materials, where the dose can be up to 10^{18} cm^{-2}, to altering threshold voltages, where the dose can be as low as 10^{12} cm^{-2}. Ion implanters are essentially a particle accelerator, where atoms are ionized, separated using mass to charge ratios and then accelerated to a target material where they interact with the target atoms until coming to rest at some point in the target. Beam scanning is used to ensure that a uniform dose is provided to the target.

The dopant profile is dependent on several different characteristics, ion energy and mass, the target material properties and the dose. The stopping range of the dopants depends on both the ion acceleration which can range from a few keV to several MeV and the target material properties. As the dopant ion moves through the target lattice it will elastically scatter off the nuclei already present and inelastically scatter with electrons. Therefore, the whole stopping power *S* of the target material is given by:

$$S = \left(\frac{dE}{dx}\right)_{nuclear} + \left(\frac{dE}{dx}\right)_{electronic} \tag{2.13}$$

where the terms are the energy *E* loss per unit path length *x* from electronic and nuclear stopping. As the nuclear stopping is caused by collisions between atoms, the potential between the ion and the atom can be described using classic kinematics:

$$V(r) = V_c(r)\, f_s(r) \tag{2.14}$$

where *r* is the separation between the atom and the ion the $f_s(r)$ is the screening function of the electrons screening the nuclei and $V_C(r)$ is given by:

$$V_c(r) = \frac{q^2 z_1 z_2}{4\pi\varepsilon_o r} \tag{2.15}$$

where z_1 and z_2 are the atomic number of the ion and atom respectively and ε_o is the permittivity of free space. Using the above potential and a center of mass frame, the given energy loss T for a collision can be calculated based on the scattering angle θ of an incident ion:

$$T = \frac{4M_1M_2}{(M_1 + M_2)} E \sin^2\left(\frac{\theta}{2}\right) \tag{2.16}$$

where M_1 and M_2 are the mass number of the ion and atom respectively. Therefore, using the above, the energy loss per unit path length can be determined by summing energy loss multiplied by the probability of a collision occurring which is given by:

$$S_{nuclear} = \left(\frac{dE}{dx}\right)_{nuclear} = N\int_0^{T_{max}} T\, d\sigma \tag{2.17}$$

where N is the number of atoms in the target per unit volume and T_{max} is the maximum energy transfer that could occur during a collision. As the nuclear stopping is often an elastic scattering event, the energy that is lost from the moving ion is transferred to the stationary atom causing it to be ejected from its lattice site creating damage in the crystal lattice. For electronic stopping in the low energy regime the stopping power is similar to a viscous drag force and is proportional to the ion velocity. The energy lost due to electronic stopping is dissipated via thermal vibrations.

Ion implantation is a fundamentally statistical process as the path of an individual ion is random with the average path length of an ion referred to as the projected range and

the distribution of the dopants being approximated as a Gaussian around the projected range R_p:

$$n(x) = n_o \exp\left(-\frac{(x - R_p)^2}{2\sigma_p^2}\right) \tag{2.18}$$

where σ_p is the straggle around the projected range and n_o the peak concentration is given by:

$$n_o = \frac{\phi}{\sqrt{2\pi}\sigma_p} \tag{2.19}$$

where ϕ is the dose. The lateral distribution of ions is also approximated using a Gaussian:

$$n(x, y) = \frac{n(x)}{\sqrt{2\pi}\sigma_\perp} \exp\left(\frac{-y^2}{2\sigma_\perp^2}\right) \tag{2.20}$$

where $\sigma_\perp$ is the lateral straggle. While the Gaussian is a useful analytical approximation of the dopant profile, it often fails for both low and high energy implants as well as high dose implants where the material properties will change throughout the course of the implantation.

2.3.2 Oxidation and thermal annealing

Oxidation of Si is an important component of the CMOS process, as a result it is a very well understood process and can be modelled successfully using the analytical Deal-Grove model [75]. This model assumes that the oxidizing species, either O_2 or H_2O, undergoes three different phenomena: diffusion of the oxidizing species from the bulk of the ambient gas to the surface; diffusion of the oxidizing species through existing oxide layer; and the reaction of the oxidizing species with the Si. All three fluxes are set to be

equal, however, for practical purposes the flux for the diffusion from the gas to the surface is dropped as it is not a rate limiting step. As a result, the following quadratic equation is obtained:

$$t = \frac{X^2}{B} + \frac{X}{B/A} - \tau \tag{2.21}$$

where t is the time of oxidation, X is the oxide thickness, B is the parabolic rate constant representing the diffusion of the oxidizing species, and B/A is the linear rate constant representing the reaction rate between the oxidizing species and the Si. B is given by an Arrhenius equation:

$$B = B_0 e^{-E_A/kT} \tag{2.22}$$

where B_o is the pre-exponential factor E_A is the activation energy, k is the Boltzmann constant and T is the temperature of the process. The linear rate constant is given by an Arrenhius equation also with a different pre-exponential factor and activation energy.

During oxidation, impurities within the Si will diffuse. Diffusion of a Gaussian distribution (as associated with ion implantation) at high temperatures can be described using the following equation:

$$N(x,t) = \frac{Q}{\sqrt{\pi D t}} \exp\left(-\frac{(x - x_0)^2}{4 D t}\right) \tag{2.23}$$

where Q is the dose of the dopant and x_o is the peak position of the dopant. For the case where ion implantation is used to introduce the dopant this would be the projected range. D is the diffusion coefficient which is described by an Arrhenius equation with the activation energy and pre-exponential factor being dependent on the dopant species.

While the diffusion of dopants in Si is well understood, the diffusion which occurs for high dose implants is often much faster in comparison, with a rapid and short-lived component referred to as transient enhanced diffusion. It is caused by the presence of lattice defects formed during the implantation and must be carefully considered in all applications.

2.3.3 Photolithography

In the work presented in this thesis, contact photolithography was used in the processing of both detectors and Ge nanowire bridges. Fig. 2.15 shows a generic process flow using both lithography and reactive ion etching (RIE). As illustrated in the figure, photolithography operates on the principle that the photoresist's chemical properties can

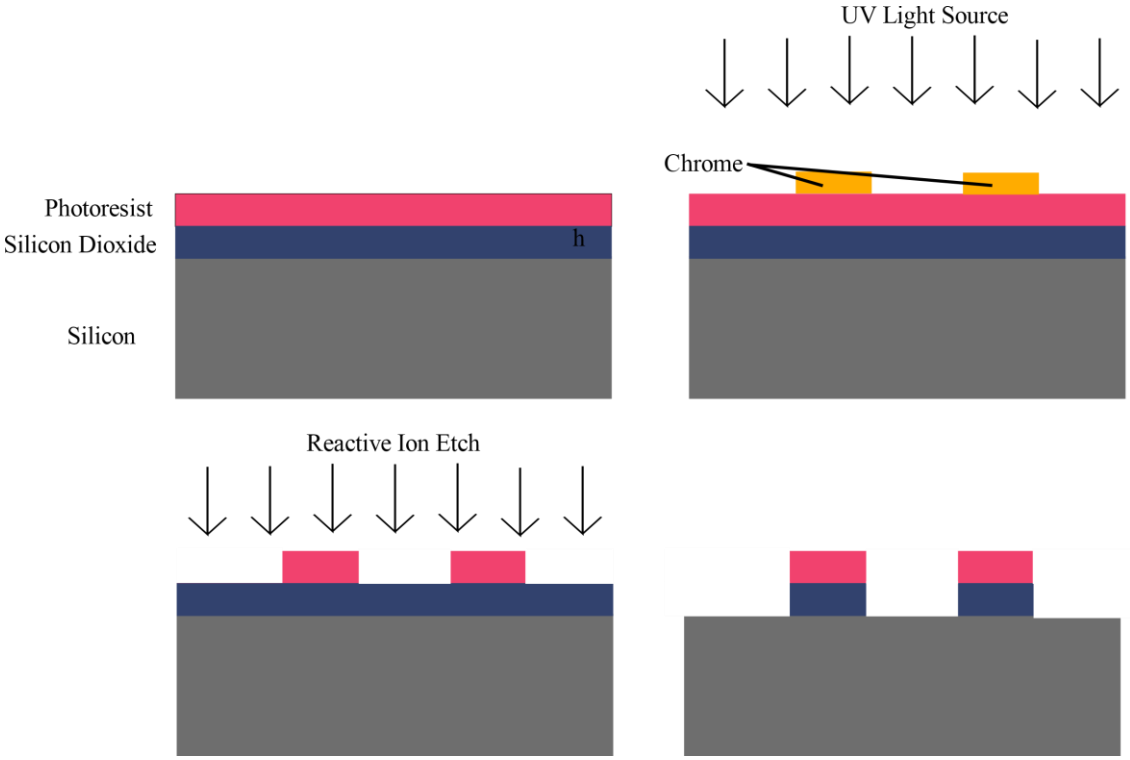

Fig 2.15 Schematic diagram of a typical CMOS process using photolithography

be altered when exposed to a UV source allowing it to be removed or as is it is more commonly referred to “developed”. By using a mask, in the case of this work a soda lime mask with patterned chrome, to prevent exposure of specific areas of photoresist, the photoresist can be selectively removed (or developed) allowing for the transfer of the pattern from the mask to the photoresist. This enables selective processing of a sample such as etching, deposition and ion implantation of specific areas.

The mask aligner used in this work was a Karl Suss MJB3 UV400, as shown in Fig 2.16, with a spectral line at 365 nm (i-line). The resists used in this work were Shipley photoresists 1808 and 1827 which provide an 800 nm and 2700 nm thick layer respectively. The samples were developed using Shipley Microposit 351 developer and deionized water in a 1:5 ratio of developer to water.

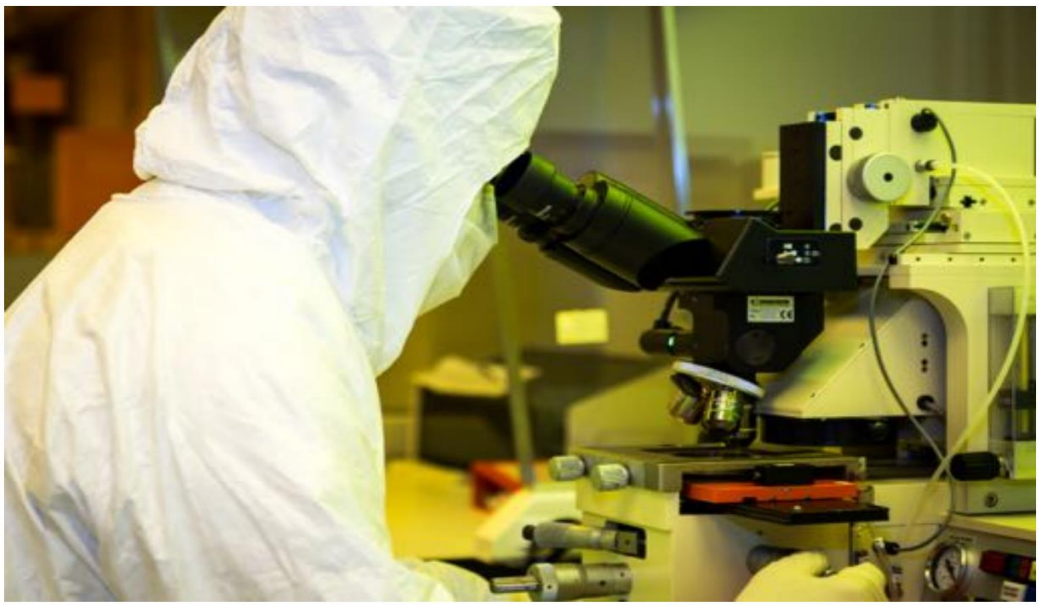

Fig 2.16 Image of a Karl Suss MJB3

2.3.4 Reactive ion etching

Etching is an important component of processing and is used in almost all integrated and photonic circuit fabrication, often multiple times for a single device. Etch methods can be divided between wet etches where the sample is immersed in a liquid and dry etches which use a reactive plasma to perform the etch. While wet etchants are often

Fig 2.17 Schematic diagram of undercutting caused by a wet etch process

inexpensive and allow for high throughput, they are also often isotropic which can lead to undercutting of the photoresist or other mask, as shown in Fig 2.17 and as a result wet etching is not suitable for some processes such as the formation of nanowire bridges. Therefore, it is necessary to use a directional etch process. One of the most common ways of doing this is RIE which uses a plasma activated from one or multiple reactive gases which cause the formation of ions, free electrons and radicals. Without a bias applied to the substrate, both inert and reactive species will come into contact with the surface of the substrate, and while the reactive species will form volatile compounds which are then pumped away the inert species will form non-volatile layers on the substrate preventing the reactive radicals from reaching the surface. When a bias is applied to the substrate this causes the ions to accelerate towards the substrate which will break up any inert species and can also cause the formation of dangling bonds which will further enhance ionization. What makes the etch directional is that while inert species will be deposited

on all surfaces, ions will only break up the species that are on surfaces that are perpendicular to the direction of travel of the ion. The etch species which are used in this thesis are SF_6, CF_4 and O_2, which are used to etch Si and Ge, oxide, and photoresist.

2.3.5 Metallization

Metallization is the general term for selective deposition of metal onto a sample, where the metal is used to form electrical contacts. A common method of metallization and the method used exclusively in this thesis is sputter deposition. For sputter deposition ions in a plasma are accelerated at a metal target. When these ions collide with the target some atoms are ejected, or "sputtered", from the target and onto the sample. In order to pattern the metal, photolithography can be employed in one of two ways. Photlithography can be used to form a mask that patterns the metal during an etching process; or it can be used to form a pattern before metal is deposited, with the entire sample subsequently immersed in a solvent which will remove the resist causing the metal to lift off as demonstrated in Fig. 2.18. Lift-off is generally more commonly used as the etchants for metal are highly corrosive. For the samples in this thesis a Kurt J. Lesker physical vapor deposition tool was used to deposite 350 nm of aluminum to form device contacts. The photolithography was done using Shipley photoresist 1827. A 2.7 μm resist is required for effective processing, and the metal was lifted off using acetone to remove the photoresist.

Fig. 2.18 Schematic diagram of a metallization and lift off process

2.4 Summary

Section 2.1 described the physics and operation of a p-i-n photodetector as well as the definitions used to describe its operation such as the signal to noise ratio, quantum efficiency, and responsivity. A consideration of the advantages and disadvantages of both waveguide coupling and NI detectors was also examined. Photodetection remains the primary use of Ge in Si photonic circuits.

Section 2.2 analyzed the growth of Ge-on-Si and its applications focusing on the different techniques which have been used to successfully grow Ge-on-Si specifically the SiGe buffer method, the low temperature/high temperature method, polycrystalline Ge, Ge condensation as well as some physical vapour deposition methods, concluding with an examination of how strain engineering can be utilized to enable Ge photodetectors and lasers at extended wavelengths.

Finally, section 2.3 examined the processing techniques which are referred to throughout the thesis: namely, photolithography, reactive ion etching and selective metallization of samples using sputtering and lift-off.

References

[1] S. M. Sze and K. K. Ng, *Physics of Semiconductor Devices Third Edition*, Third Edit. Hoboken, New Jersey: John Wiley & Sons, 2006.

[2] A. Alping, R. Tell, and S. Eng, "Photodetection properties of semiconductor laser diode detectors," *J. Light. Technol.*, vol. 4, no. 11, pp. 1662–1668, 2008.

[3] Dongwoo Suh, Sanghoon Kim, Jiho Joo, and Gyungock Kim, "36-GHz High-

Responsivity Ge Photodetectors Grown by RPCVD," *IEEE Photonics Technol. Lett.*, vol. 21, no. 10, pp. 672–674, 2009.

[4] O. I. Dosunmu, D. D. Cannon, M. K. Emsley, B. Ghyselen, J. Liu, L. C. Kimerling, and M. S. Ünlü, "Resonant cavity enhanced Ge photodetectors for 1550 nm operation on reflecting si substrates," *IEEE J. Sel. Top. Quantum Electron.*, vol. 10, no. 4, pp. 694–701, 2004.

[5] P. Dong, J. E. Cunningham, M. Asghari, N.-N. Feng, D. Zheng, A. V. Krishnamoorthy, D. Feng, S. Liao, R. Shafiiha, G. Li, and H. Liang, "Vertical p-i-n germanium photodetector with high external responsivity integrated with large core Si waveguides," *Opt. Express*, vol. 18, no. 1, p. 96, 2009.

[6] J. Wang and S. Lee, "Ge-photodetectors for Si-based optoelectronic integration," *Sensors*, vol. 11, no. 1, pp. 696–718, 2011.

[7] L. C. Kimerling, D. D. Can, M. S. Unlu, M. K. Emsley, and O. I. Dosunmu, "High-speed resonant cavity enhanced Ge photodetectors on reflecting Si substrates for 1550-nm operation," *IEEE Photonics Technol. Lett.*, vol. 17, no. 1, pp. 175–177, 2004.

[8] E. Dröge, S. Kollakowski, M. Grundmann, E. H. Böttcher, M. Herrscher, and D. Bimberg, "Epitaxial liftoff InGaAs/InP MSM photodetectors on Si," *Electron. Lett.*, vol. 31, no. 16, pp. 1383–1384, 2002.

[9] I. Rey-Stolle, E. Barrigón, B. Galiana, and C. Algora, "Analysis of germanium epiready wafers for III-V heteroepitaxy," *J. Cryst. Growth*, vol. 310, no. 23, pp. 4803–4807, 2008.

[10] J. Michel, J. Liu, and L. C. Kimerling, "High-performance Ge-on-Si

photodetectors," *Nat. Photonics*, vol. 4, no. 8, pp. 527–534, 2010.

[11] S. Luryi, A. Kastalsky, and J. C. Bean, "New infrared Detector on a Silicon Chip," *IEEE Trans. Electron Devices*, vol. 31, no. 9, pp. 1135–1139, 1984.

[12] M. T. Currie, S. B. Samavedam, T. A. Langdo, C. W. Leitz, and E. A. Fitzgerald, "Controlling threading dislocation densities in Ge on Si using graded SiGe layers and chemical-mechanical polishing," *Appl. Phys. Lett.*, vol. 72, no. 14, pp. 1718–1720, 1998.

[13] S. B. Samavedam, M. T. Currie, T. A. Langdo, and E. A. Fitzgerald, "High-quality germanium photodiodes integrated on silicon substrates using optimized relaxed graded buffers," *Appl. Phys. Lett.*, vol. 73, no. 15, pp. 2125–2127, 1998.

[14] J. Oh, J. C. Campbell, S. G. Thomas, S. Bharatan, R. Thoma, C. Jasper, R. E. Jones, and T. E. Zirkle, "Interdigitated Ge p-i-n photodetectors fabricated on a Si substrate using graded SiGe buffer layers," *IEEE J. Quantum Electron.*, vol. 38, no. 9, pp. 1238–1241, 2002.

[15] G. Luo, T. H. Yang, E. Y. Chang, C. Y. Chang, and K. A. Chao, "Growth of high-quality Ge epitaxial layers on Si (100)," *Japanese J. Appl. Physics, Part 2 Lett.*, vol. 42, no. 5 B, pp. 517–519, 2003.

[16] Z. Huang, J. Oh, and J. C. Campbell, "Back-side-illuminated high-speed Ge photodetector fabricated on Si substrate using thin SiGe buffer layers," *Appl. Phys. Lett.*, vol. 85, no. 15, pp. 3286–3288, 2004.

[17] Z. Huang, N. Kong, X. Guo, M. Liu, N. Duan, A. L. Beck, S. K. Banerjee, J. C. Campbell, and A. Backside-illuminated, "Photodiode Using Thin SiGe Buffer Layers," *IEEE J. Sel. Top. Quantum Electron.*, vol. 12, no. 6, pp. 1450–1454, 2006.

[18] L. Colace, G. Masini, F. Galluzzi, G. Assanto, G. Capellini, L. Di Gaspare, E. Palange, and F. Evangelisti, "Metal-semiconductor-metal near-infrared light detector based on epitaxial Ge/Si," *Appl. Phys. Lett.*, vol. 72, no. 24, pp. 3175–3177, 1998.

[19] H. C. Luan, D. R. Lim, K. K. Lee, K. M. Chen, J. G. Sandland, K. Wada, and L. C. Kimerling, "High-quality Ge epilayers on Si with low threading-dislocation densities," *Appl. Phys. Lett.*, vol. 75, no. 19, pp. 2909–2911, 1999.

[20] S. Famà, L. Colace, G. Masini, G. Assanto, and H. C. Luan, "High performance germanium-on-silicon detectors for optical communications," *Appl. Phys. Lett.*, vol. 81, no. 4, pp. 586–588, 2002.

[21] M. Oehme, J. Werner, M. Jutzi, G. Wöhl, E. Kasper, and M. Berroth, "High-speed germanium photodiodes monolithically integrated on silicon with MBE," *Thin Solid Films*, vol. 508, no. 1–2, pp. 393–395, 2006.

[22] J. M. Hartmann, A. Abbadie, A. M. Papon, P. Holliger, G. Rolland, T. Billon, J. M. Fédéli, M. Rouvière, L. Vivien, and S. Laval, "Reduced pressure-chemical vapor deposition of Ge thick layers on Si(001) for 1.3-1.55-μm photodetection," *J. Appl. Phys.*, vol. 95, no. 10, pp. 5905–5913, 2004.

[23] M. Jutzi, M. Berroth, G. Wöhl, M. Oehme, and E. Kasper, "Ge-on-Si vertical incidence photodiodes with 39-GHz bandwidth," *IEEE Photonics Technol. Lett.*, vol. 17, no. 7, pp. 1510–1512, 2005.

[24] L. Vivien, J. Osmond, J.-M. Fédéli, D. Marris-Morini, P. Crozat, J.-F. Damlencourt, E. Cassan, Y. Lecunff, and S. Laval, "42 GHz pin Germanium photodetector integrated in a silicon-on-insulator waveguide," *Opt. Express*, vol. 17, no.

8, p. 6252, 2009.

[25] G. Masini, L. Colace, F. Galluzzi, and G. Assanto, “Advances in the field of poly-Ge on Si near infrared photodetectors,” *Mater. Sci. Eng. B Solid-State Mater. Adv. Technol.*, vol. 69, pp. 257–260, 2000.

[26] G. Masini, L. Colace, and G. Assanto, “2.5 Gbit/s polycrystalline germanium-on-silicon photodetector operating from 1.3 to 1.55 μm,” *Appl. Phys. Lett.*, vol. 82, no. 15, pp. 2524–2526, 2003.

[27] L. Colace, G. Masini, V. Cencelli, F. DeNotaristefani, and G. Assanto, “A near-infrared digital camera in polycrystalline germanium integrated on silicon,” *IEEE J. Quantum Electron.*, vol. 43, no. 4, pp. 311–315, 2007.

[28] G. Masini, V. Cencelli, L. Colace, F. De Notaristefani, and G. Assanto, “Monolithic integration of near-infrared Ge photodetectors with Si complementary metal-oxide-semiconductor readout electronics,” *Appl. Phys. Lett.*, vol. 80, no. 18, pp. 3268–3270, 2002.

[29] G. Masini, L. Colace, and G. Assanto, “Near-infrared waveguide photodetectors based on polycrystalline Ge on silicon-on-insulator substrates,” *Opt. Mater. (Amst).*, vol. 17, no. 1–2, pp. 243–246, 2001.

[30] L. Colace, G. Masini, and G. Assanto, “Guided-wave near-infrared detector in polycrystalline germanium on silicon,” *Appl. Phys. Lett.*, vol. 87, no. 20, pp. 1–3, 2005.

[31] L. Colace, G. M. A. Altieri, and G. Assanto, “Waveguide photodetectors for the near-infrared in polycrystalline germanium on silicon,” *IEEE Photonics Technol. Lett.*, vol. 18, no. 9, pp. 1094–1096, 2006.

[32] V. Sorianello, M. Balbi, L. Colace, G. Assanto, L. Socci, L. Bolla, G. Mutinati, and M. Romagnoli, “Guided-wave photodetectors in germanium on SOI optical chips,” *Phys. E Low-Dimensional Syst. Nanostructures*, vol. 41, no. 6, pp. 1090–1093, 2009.

[33] V. Sorianello, L. Colace, G. Assanto, A. Notargiacomo, N. Armani, F. Rossi, and C. Ferrari, “Thermal evaporation of Ge on Si for near infrared detectors: Material and device characterization,” *Microelectron. Eng.*, vol. 88, no. 4, pp. 526–529, 2011.

[34] V. Sorianello, A. De Iacovo, L. Colace, A. Fabbri, L. Tortora, E. Buffagni, and G. Assanto, “High responsivity near-infrared photodetectors in evaporated Ge-on-Si,” *Appl. Phys. Lett.*, vol. 101, no. 8, 2012.

[35] O. W. Holland, C. W. White, and D. Fathy, “Novel oxidation process in Ge+-implanted Si and its effect on oxidation kinetics,” *Appl. Phys. Lett.*, vol. 51, no. 7, pp. 520–522, 1987.

[36] D. Fathy, O. W. Holland, and C. W. White, “Formation of epitaxial layers of Ge on Si substrates by Ge implantation and oxidation,” *Appl. Phys. Lett.*, vol. 51, no. 17, pp. 1337–1339, 1987.

[37] P. E. Hellberg, S. L. Zhang, F. M. D’Heurle, and C. S. Petersson, “Oxidation of silicon-germanium alloys. I. An experimental study,” *J. Appl. Phys.*, vol. 82, no. 11, pp. 5773–5778, 1997.

[38] P. E. Hellberg, S. L. Zhang, F. M. D’Heurle, and C. S. Petersson, “Oxidation of silicon-germanium alloys. II. A mathematical model,” *J. Appl. Phys.*, vol. 82, no. 11, pp. 5779–5787, 1997.

[39] F. K. LeGoues, R. Rosenberg, T. Nguyen, F. Himpsel, and B. S. Meyerson,

"Oxidation studies of SiGe," *J. Appl. Phys.*, vol. 65, no. 4, pp. 1724–1728, 1989.

[40] F. K. LeGoues, R. Rosenberg, and B. S. Meyerson, "Kinetics and mechanism of oxidation of SiGe: Dry versus wet oxidation," *Appl. Phys. Lett.*, vol. 54, no. 7, pp. 644–646, 1989.

[41] J. Eugène, F. K. LeGoues, V. P. Kesan, S. S. Iyer, and F. M. D'Heurle, "Diffusion versus oxidation rates in silicon-germanium alloys," *Appl. Phys. Lett.*, vol. 59, no. 1, pp. 78–80, 1991.

[42] H. K. Liou, P. Mei, U. Gennser, and E. S. Yang, "Effects of Ge concentration on SiGe oxidation behavior," *Appl. Phys. Lett.*, vol. 59, no. 10, pp. 1200–1202, 1991.

[43] M. A. Rabie, Y. M. Haddara, and J. Carette, "A kinetic model for the oxidation of silicon germanium alloys," *J. Appl. Phys.*, vol. 98, no. 7, 2005.

[44] K. Hossain, L. K. Savage, and O. W. Holland, "Rate enhancement during thermal oxidation of Ge+-implanted silicon," *Nucl. Instruments Methods Phys. Res. Sect. B Beam Interact. with Mater. Atoms*, vol. 241, no. 1–4, pp. 553–558, 2005.

[45] K. Hossain, O. W. Holland, F. U. Naab, L. J. Mitchell, P. R. Poudel, J. L. Duggan, and F. D. McDaniel, "Dose-dependent thermal oxidation of Ge+-implanted silicon," *Nucl. Instruments Methods Phys. Res. Sect. B Beam Interact. with Mater. Atoms*, vol. 261, no. 1–2 SPEC. ISS., pp. 620–623, 2007.

[46] H. J. Oh, K. J. Choi, W. Y. Loh, T. Htoo, S. J. Chua, and B. J. Cho, "Integration of GaAs epitaxial layer to Si-based substrate using Ge condensation and low-temperature migration enhanced epitaxy techniques," *J. Appl. Phys.*, vol. 102, no. 5, 2007.

[47] T. Tezuka, N. Sugiyama, and S. Takagi, "Fabrication of strained Si on an ultrathin

SiGe-on-insulator virtual substrate with a high-Ge fraction," *Appl. Phys. Lett.*, vol. 79, no. 12, pp. 1798–1800, 2001.

[48] S. Nakaharai, T. Tezuka, N. Sugiyama, Y. Moriyama, and S. I. Takagi, "Characterization of 7-nm-thick strained Ge-on-insulator layer fabricated by Ge-condensation technique," *Appl. Phys. Lett.*, vol. 83, no. 17, pp. 3516–3518, 2003.

[49] Z. Y. Xue, Z. F. Di, L. Ye, Z. Q. Mu, D. Chen, X. Wei, M. Zhang, and X. Wang, "Study of Ge loss during Ge condensation process," *Thin Solid Films*, vol. 557, pp. 120–124, 2014.

[50] S. Balakumar, S. Peng, K. M. Hoe, A. Agarwal, G. Q. Lo, R. Kumar, N. Balasubramanian, D. L. Kwong, and S. Tripathy, "SiGeO layer formation mechanism at the SiGe/oxide interfaces during Ge condensation," *Appl. Phys. Lett.*, vol. 90, no. 3, pp. 2005–2008, 2007.

[51] N. Sugiyama, T. Tezuka, T. Mizuno, M. Suzuki, Y. Ishikawa, N. Shibata, and S. Takagi, "Temperature effects on Ge condensation by thermal oxidation of SiGe-on-insulator structures," *J. Appl. Phys.*, vol. 95, no. 8, pp. 4007–4011, 2004.

[52] S. W. Bedell, K. Fogel, D. K. Sadana, and H. Chen, "Defects and strain relaxation in silicon-germanium-on-insulator formed by high-temperature oxidation," *Appl. Phys. Lett.*, vol. 85, no. 24, pp. 5869–5871, 2004.

[53] W. Liu, S. Luo, Z. Song, Z. Di, M. Zhang, C. Lin, P. K. Chu, and A. Huang, "Fabrication and mechanism of relaxed SiGe-on-insulator by modified Ge condensation," *J. Vac. Sci. Technol. B Microelectron. Nanom. Struct.*, vol. 23, no. 4, p. 1637, 2005.

[54] Z. Di, P. K. Chu, M. Zhang, W. Liu, Z. Song, and C. Lin, "Germanium movement

mechanism in SiGe-on-insulator fabricated by modified Ge condensation," *J. Appl. Phys.*, vol. 97, no. 6, 2005.

[55] T. Shimura, M. Shimizu, S. Horiuchi, H. Watanabe, K. Yasutake, and M. Umeno, "Self-limiting oxidation of SiGe alloy on silicon-on-insulator wafers," *Appl. Phys. Lett.*, vol. 89, no. 11, pp. 10–13, 2006.

[56] S. Nakaharai, T. Tezuka, N. Hirashita, E. Toyoda, Y. Moriyama, N. Sugiyama, and S. Takagi, "Formation process of high-purity Ge-on-insulator layers by Ge-condensation technique," *J. Appl. Phys.*, vol. 105, no. 2, 2009.

[57] B. G. Min, J. H. Yoo, H. C. Sohn, D. H. Ko, M. H. Cho, K. B. Chung, and T. W. Lee, "Behavior of strain at a thin Ge pile-up layer formed by dry oxidation of a Si0.7Ge0.3 film," *Thin Solid Films*, vol. 518, no. 8, pp. 2065–2069, 2010.

[58] T. Shimura, T. Inoue, D. Shimokawa, T. Hosoi, Y. Imai, O. Sakata, S. Kimura, and H. Watanabe, "Characterization of sige layer during ge condensation process by X-ray diffraction methods," *Jpn. J. Appl. Phys.*, vol. 50, no. 1, 2011.

[59] Y. Zhang, K. Cai, C. Li, S. Chen, H. Lai, and J. Kang, "Strain Relaxation in Ultrathin SiGeOI Substrates Fabricated by Multistep Ge Condensation Method," *J. Electrochem. Soc.*, vol. 156, no. 2, pp. H115–H118, 2009.

[60] M. Garozzo, G. Conte, F. Evangelisti, and G. Vitali, "Heteroepitaxial growth of Ge on 〈111〉 Si by vacuum evaporation," *Appl. Phys. Lett.*, vol. 41, no. 11, pp. 1070–1072, 1982.

[61] G. Bajor, K. C. Cadien, M. A. Ray, J. E. Greene, and P. S. Vijayakumar, "Growth of high quality epitaxial Ge films on (100)Si by sputter deposition," *Appl. Phys. Lett.*,

vol. 40, no. 8, pp. 696–698, 1982.

[62] S. M. Pietralunga, M. Feré, M. Lanata, D. Piccinin, G. Radnóczi, F. Misják, A. Lamperti, M. Martinelli, and P. M. Ossi, "Heteroepitaxial sputtered Ge on Si (100): Nanostructure and interface morphology," *Europhys. Lett.*, vol. 88, no. 2, 2009.

[63] M. Steglich, C. Patzig, L. Berthold, F. Schrempel, K. Füchsel, T. Höche, E. B. Kley, and A. Tünnermann, "Heteroepitaxial Ge-on-Si by DC magnetron sputtering," *AIP Adv.*, vol. 3, no. 7, 2013.

[64] J. Liu, D. D. Cannon, K. Wada, Y. Ishikawa, S. Jongthammanurak, D. T. Danielson, J. Michel, and L. C. Kimerling, "Tensile strained Ge p-i-n photodetectors on Si platform for C and L band telecommunications," *Appl. Phys. Lett.*, vol. 87, no. 1, 2005.

[65] Y. Ishikawa, K. Wada, D. D. Cannon, J. Liu, H. C. Luan, and L. C. Kimerling, "Strain-induced band gap shrinkage in Ge grown on Si substrate," *Appl. Phys. Lett.*, vol. 82, no. 13, pp. 2044–2046, 2003.

[66] J. Liu, X. Sun, R. Camacho-Aguilera, L. C. Kimerling, and J. Michel, "Ge-on-Si laser operating at room temperature," *Opt. Lett.*, vol. 35, no. 5, p. 679, 2010.

[67] J. Liu, X. Sun, D. Pan, X. Wang, L. C. Kimerling, T. L. Koch, and J. Michel, "Tensile-strained, n-type Ge as a gain medium for monolithic laser integration on Si," *Opt. Express*, vol. 15, no. 18, p. 11272, 2007.

[68] J. Liu, L. C. Kimerling, and J. Michel, "Monolithic Ge-on-Si lasers for large-scale electronic-photonic integration," *Semicond. Sci. Technol.*, vol. 27, no. 9, 2012.

[69] J. R. Jain, A. Hryciw, T. M. Baer, D. A. B. Miller, M. L. Brongersma, and R. T.

Howe, “A micromachining-based technology for enhancing germanium light emission via tensile strain,” *Nat. Photonics*, vol. 6, no. 6, pp. 398–405, 2012.

[70] A. Gassenq, S. Tardif, K. Guilloy, G. Osvaldo Dias, N. Pauc, I. Duchemin, D. Rouchon, J. M. Hartmann, J. Widiez, J. Escalante, Y. M. Niquet, R. Geiger, T. Zabel, H. Sigg, J. Faist, A. Chelnokov, F. Rieutord, V. Reboud, and V. Calvo, “Accurate strain measurements in highly strained Ge microbridges,” *Appl. Phys. Lett.*, vol. 108, no. 24, 2016.

[71] M. J. Süess, R. Geiger, R. A. Minamisawa, G. Schiefler, J. Frigerio, D. Chrastina, G. Isella, R. Spolenak, J. Faist, and H. Sigg, “Analysis of enhanced light emission from highly strained germanium microbridges,” *Nat. Photonics*, vol. 7, no. 6, pp. 466–472, 2013.

[72] D. S. Sukhdeo, D. Nam, J.-H. Kang, M. L. Brongersma, and K. C. Saraswat, “Direct bandgap germanium-on-silicon inferred from 57% ⟨100⟩ uniaxial tensile strain [Invited],” *Photonics Res.*, vol. 2, no. 3, p. A8, 2014.

[73] S. Bao, D. Kim, C. Onwukaeme, S. Gupta, K. Saraswat, K. H. Lee, Y. Kim, D. Min, Y. Jung, H. Qiu, H. Wang, E. A. Fitzgerald, C. S. Tan, and D. Nam, “Low-threshold optically pumped lasing in highly strained germanium nanowires,” *Nat. Commun.*, vol. 8, no. 1, pp. 1–7, 2017.

[74] J. D. Plummer, M. D. Deal, and M. P. Griffin, *Silicon VLSI Technology: Fundamentals Practice and Modeling.* Upper Saddle River, New Jersey: Prentice Hall, 2000.

[75] B. E. Deal and A. S. Grove, “General relationship for the thermal oxidation of

silicon," *J. Appl. Phys.*, vol. 36, no. 12, pp. 3770–3778, 1965.

Chapter 3 – Ge condensation via High Fluence Ion Implantation

Overview

This chapter presents work done on Ge condensation using high fluence ion implantation. The work is performed using SOI as the starting substrate. Material analysis determined the crystalline quality of the layer, the distribution of Ge and the enhancement in the rate of oxidation. Building on this analysis is a comprehensive review of the condensation process in SOI and description of a physical and predictive model. The chapter also contains detailed analysis of induced strain. The final section of this chapter then describes the use of the implantation and condensation process to fabricate a detector, with both electrical and loss measurements of the detector included. Results from this work have been reported by the author in the following journal publication:

R. Anthony, Y. M. Haddara, I. F. Crowe and A. P. Knights, "SiGe-on-insulator fabricated via germanium condensation following high-fluence Ge^+ ion implantation," *J. Appl. Phys.*, vol. 122, no. 6, 2017

3.1 Experimental methods

Samples of single crystal 220 nm SOI with a 2000 nm BOX were implanted with Ge^+ ions to a fluence of $5x10^{16}$ cm^{-2} and at an energy of 33 keV. Following implantation,

thermal oxidation was performed in a tube furnace in a steam ambient which was produced by passing O_2 gas through a H_2O heated to 95 °C. The samples were initially oxidized at 870 °C for 70 minutes (primary oxidation) and then oxidized again (secondary oxidation) at either 900 °C, 1000 °C, or 1080 °C with the secondary oxidation being performed incrementally in time using multiple samples. Samples were oxidized from 15 to 150 minutes in 15 minute increments at 900 °C; 10 to 80 minutes in 10 minute increments at 1000 °C and 5 to 35 minutes in 5 minute increments at 1080 °C. The furnace was calibrated by oxidizing unimplanted, low doped reference Si samples simultaneously with the Ge-implanted samples followed by comparison with the Deal-Grove oxidation model [1]. The primary 870 °C oxidation was introduced after preliminary work indicated that direct high temperature oxidation of the Ge implanted SOI resulted in majority evaporation of the Ge before any formed oxide layer could act as a diffusion barrier. This is consistent with the work reported in Ref. [2]. It is noted that minority dose loss occurs during the primary oxidation of the two-stage oxidation process; which has been quantified and is reported on in section 3.2 and 3.3 of this work.

The fabrication process is summarized schematically in Fig. 3.1. The fabricated films were analysed using RBS performed at the 1.7 MV Tandetron Accelerator Facility at Western University. RBS is ideally suited for the extraction of concentration profiles of dissimilar materials from multiple samples, albeit producing results with relatively modest resolution. The probe was a 1.5 MeV He^+ ion beam incident at 7° to the normal of the sample surface with a Si charged particle detector mounted at 170°, with an average counts per sample approximately 27,000. The RBS spectra were analyzed using

simulation software SIMNRA (SIMulation of Nuclear Reaction Analysis) [3] in order to determine the composition and thickness of both the oxide and SiGe layers. The system under study is amenable to RBS analysis due to the high Ge content and the significant difference in mass between Ge and Si. The uncertainties in Ge concentration, Ge layer thickness and SiO_2 thickness obtained through RBS analysis and fitting are estimated to be on the order of 5%. The grown oxide thicknesses were independently measured optically. The tool used was a Woollam M-2000 automated angle spectroscopic ellipsometer. This allowed confidence in the extracted profiles obtained from RBS by reducing the number of variables in the SIMNRA simulation. In order to facilitate Raman

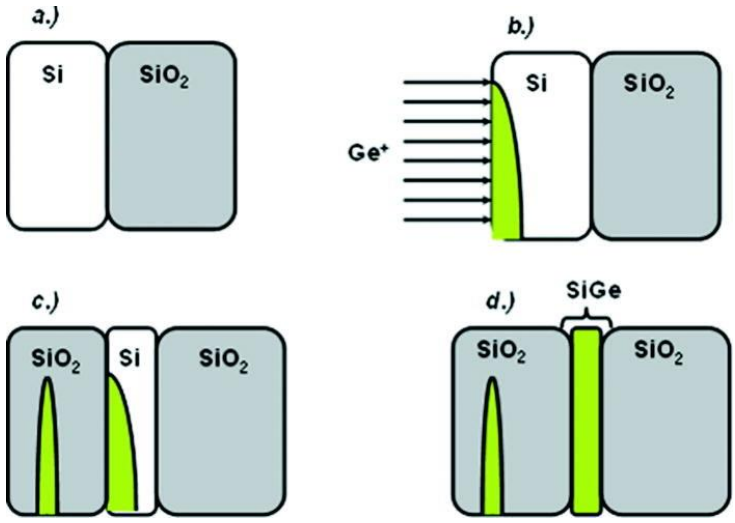

Fig. 3.1. Schematic description of the two-step oxidation process: a.) starting substrate consists of 220 nm thick Si on 2000 nm BOX SOI; b.) implantation of $5x10^{16}$ cm^{-2} Ge^{+} at 33 keV; c.) primary oxidation at 870 °C used to cap the SiGeOI, resulting in a mixed oxide; d.) secondary oxidation at either 900, 1000 or 1080 °C to form final SiGeOI structure.

spectroscopy of a subset of the prepared samples, optical excitation was provided by the 325nm line of a He:Cd laser and the scattered light was collected, confocally using a Thorlabs LMU-40x NUV objective lens with a numerical aperture, NA = 0.5, dispersed

using a Horiba LabRAM HR Evolution spectrometer and detected with a thermoelectrically cooled Charge-Coupled Device (CCD) camera. It should be noted that for excitation at longer wavelengths, i.e. at 488nm, the Raman scattering spectra was entirely dominated by the main Si-Si optical phonon peak (~520 cm^{-1}), presumably from the unconsumed thin underlying Si layer. For 488nm, the relative optical penetration depths in bulk Si and Ge are 569 nm and 19 nm, respectively, whereas at 325 nm, this is ~10 nm, for both Si and Ge. The dramatic increase in the Ge-Ge and Si-Ge scattering peaks (and relative suppression of the Si-Si substrate scattering) that were observed for 325 nm excitation therefore implies an upper limit on the condensed SiGeOI layer thickness of ~20 nm for the samples probed, which will be shown as consistent with the RBS analysis. TEM was performed on a representative sample as a means to assess the crystallinity of the SiGe layer and to provide a verification of the Ge profile in the structures. Scanning-transmission electron microscopy (STEM) and energy dispersive X-ray spectroscopy (EDS) analysis was also performed on the same sample. The electron microscopy and analysis was performed using a JEOL JEM-2010F Field Emission Electron Microscope equipped with an Oxford Instruments EDS analyzer. The sample was exposed to an electron beam accelerating voltage of 200 kV. Elemental maps for Ge, O and Si were obtained. The profile of Ge was obtained using INCAEnergy EDS software, and was plotted together with the STEM images to confirm the location of the Ge. No attempt was made to quantify the Ge concentration using the EDS, and as such the profiles only provide the relative depth distribution of the Ge in the grown oxide and the SiGe layer.

3.2 Model description

Modeling of the implantation-condensation process was performed using the commercially available SENTAURUS Technology Computer Aided Design (TCAD) platform provided by Synopsys® [4]. The nature of the model is semi-empirical, however, the fits to the experimental data yield important insights into the underlying processes at work. The model can be described using three parameters: (1) a segregation coefficient; (2) an enhanced Ge diffusion coefficient (both 1 and 2 are used to model the incorporation of Ge into the oxide as well as the profile of the Ge in the SiGe-On-Insulator layer) and (3) a modified linear rate constant describing the thermal oxidation.

It has been established previously that the presence of Ge enhances the rate of thermal SiO_2 growth [5–8], although Ge should only affect the linear rate constant (as described by the Deal-Grove model [1]) since this is determined by the reaction rate at the growth interface. The presence of Ge should not affect the parabolic rate constant since that is determined by the diffusivity of the oxidizing species through the oxide given that the oxide grown is predominantly SiO_2. As a result, the oxidation is modelled using a linear rate constant that is a function of temperature only. Fig. 3.2 shows the values of the linear rate constant used in simulation of the experimental data, compared with the constant used to describe the oxidation of low-doped, (100) Si. The activation energy for the enhanced linear rate constant (deduced from the Arrhenius relationship) is 1.52 eV, consistent with the predictive modeling by Rabie et al. [9].

The most important aspect in modeling and deriving a physical understanding of the experimental measurements is the simulation of the Ge pile-up in the remaining

SiGeOI layer after thermal oxidation. In this respect, the Ge segregation coefficient (i.e. the ratio of Ge in the SiGe to that in the oxide at the $SiGe/SiO_2$ interface) is only important insofar as it determines the total dose of Ge in the oxide and the SiGeOI layer. Several authors have modeled Ge pile-up by assuming a rejection of Ge from SiO_2 into the Si: effectively an infinite segregation coefficient [see, e.g., Ref. [10]].

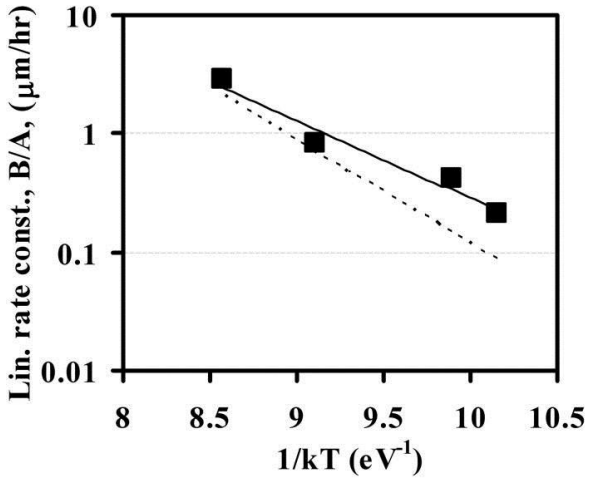

Fig. 3.2 Simulated linear rate constant for oxidation of Ge implanted SOI samples fabricated in this study (solid square markers) in the temperature range 870-1080 °C. The solid line is an Arrhenius fit to the experimental data yielding an activation energy of 1.52eV. The dashed line represents the Arrhenius description of the linear rate constant for low doped Si, with associated activation energy of 2.05eV.

Others have used a segregation coefficient that is a function of the Ge fraction [4]. Neither of these approaches accounts for the observed formation of mixed oxides under certain experimental conditions (see Ref. [11] and references therein). In the experimental data (for example see Fig. 3.6 and Fig. 3.11 in section 3.3) a complex pattern is observed whereby during oxidation at 870 °C there is an initial oxide layer with no Ge content, followed by the incorporation of Ge in a thin layer, followed by rejection of Ge from the oxide at all subsequent times (and at all higher temperatures). To simulate this pattern, an empirical approach in modeling the incorporation of Ge into the oxide is used.

Specifically, the segregation model incorporated in SENTARUS is used as an ON/OFF 'switch' for the incorporation of Ge in the growing oxide. With segregation ON, a constant segregation coefficient = 1000 is used. This is sufficient to exclude all Ge from the growing oxide. There was no requirement to make the segregation coefficient dependent on Ge concentration or temperature. With segregation OFF, a segregation boundary condition is still used but with a segregation coefficient = 1. This ON/OFF

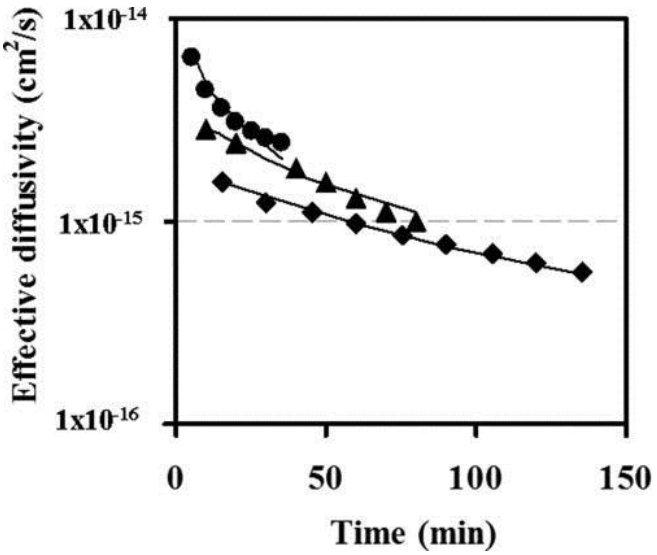

Fig. 3.3. Simulated effective diffusivities of Ge in the SiGeOI layer versus oxidation time at 900 °C (diamonds), 1000 °C (triangles), and 1080 °C (circles). The lines are calculated based on the assumption of an enhanced diffusivity decaying exponentially to equilibrium.

switch is used only to describe the experimental results obtained for the primary 870 °C oxidation. For all higher, secondary oxidations, which take place following the capping 870 °C oxidation, the segregation coefficient was set to ON with a value of 1000. The use of the segregation switch in this purely empirical portion of the model ironically allows us to conclude that segregation is not the dominant mechanism responsible for the

incorporation of Ge in the growing oxide. This conclusion is supported through detailed discussion in section 3.3.

To simulate the Ge profile in the SiGeOI layer at different times and temperatures an effective interdiffusivity of Si and Ge is used as a fitting parameter. The peak concentration of Ge at the growth interface is almost entirely determined by the bulk diffusion behavior [4] whereas the details of the flux of Ge across the growth interface plays only a minor role, primarily in determining the dose of Ge left in the SiGeOI layer. The effective Ge diffusivity at each oxidation temperature, needed to obtain an acceptable fit, is shown in Fig. 3.3. The lines are fits to the experimental data assuming that the instantaneous diffusivity decays exponentially from an initial value that is significantly higher than equilibrium. While there are differences in previous work regarding the effective interdiffusivity of Si and Ge (see Ref. [12] and references therein) the values in Fig. 3.3 are seen to correspond to diffusion enhancements on the order of 1000, 10, and 1 for anneals at 900, 1000, and 1080 °C, respectively. The time constants for the decay in the diffusion enhancement are 41, 21, and 3.4 minutes, respectively.

Assuming an equilibrium diffusivity, $D = 310 \exp(-4.65/k_bT)$ [4], this behavior is fully consistent with Transient Enhanced Diffusion (TED) due to the increased defect density caused by the Ge^+ implantation. Most often, TED is associated with residual end-of-range (EOR) defects following amorphizing ion implantation. It is generally assumed that such defects do not play a significant role in enhanced diffusion on the time-scales of the experiment because dissolution of such defects is assumed to take place in a matter of a few seconds at such elevated temperatures [13]. However, recent work on the impact of

amorphizing implantation on the performance of solar cells has suggested that extended thermal budgets, used both in solar cell fabrication and in this work, are not sufficient to remove clustered defects even for anneal temperatures >950 °C and duration of >10 minutes [14]. An alternative explanation for the observation of enhanced diffusion is the phenomenon of concentration dependent diffusion. For example, Ref. [15] describes an experimental study of Ge diffusion in $Si_{1-x}Ge_x$ with x ranging from 0 to 0.5. The activation energy for diffusion decreased from 4.7 eV to 3.2 eV across this range, a result of increased diffusion via a vacancy mechanism with increasing Ge content. The simulated values of diffusivity (Fig. 3.3) are consistent with the values obtained in Ref. [15] while the steep gradient of Ge in the SiGe layer (and its temporal evolution) may explain the simulated decrease in Ge diffusivity with time. The diffusion of Ge in the samples is complex and a study of the detailed kinetics is beyond the scope of this work. It should be noted though that there is no doubt that an enhancement of the (apparent) effective diffusivity of the Ge exists on a timescale that decreases with increasing temperature.

3.3 Results and discussion

3.3.1 As-implanted profile and that following the primary 870 °C oxidation

Figs. 3.4 and 3.5 show the as-acquired RBS spectra and the simulated profile generated using SIMNRA for an as-implanted sample and a sample after the primary 70 minute oxidation at 870 °C. The agreement of the fitted curves with the experimental data is typical of all of those obtained and thus these serve as representative examples. The

experimentally determined as-implanted fluence is 4.8×10^{16} cm^{-2}, (i.e. 4% lower than the nominal implanted fluence of $5x10^{16}$ cm^{-2}), likely reflecting a combination of implantation fluence calibration, measurement uncertainty and sample sputtering during

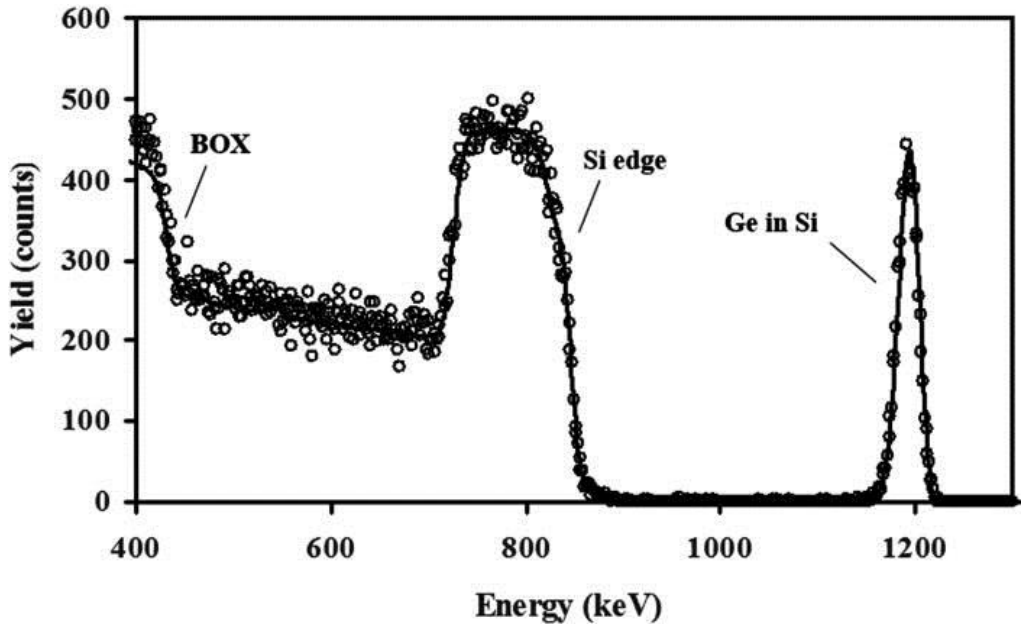

Fig. 3.4 RBS spectrum of the as-implanted sample. The markers are the experimental data and the line is generated using SIMNRA.

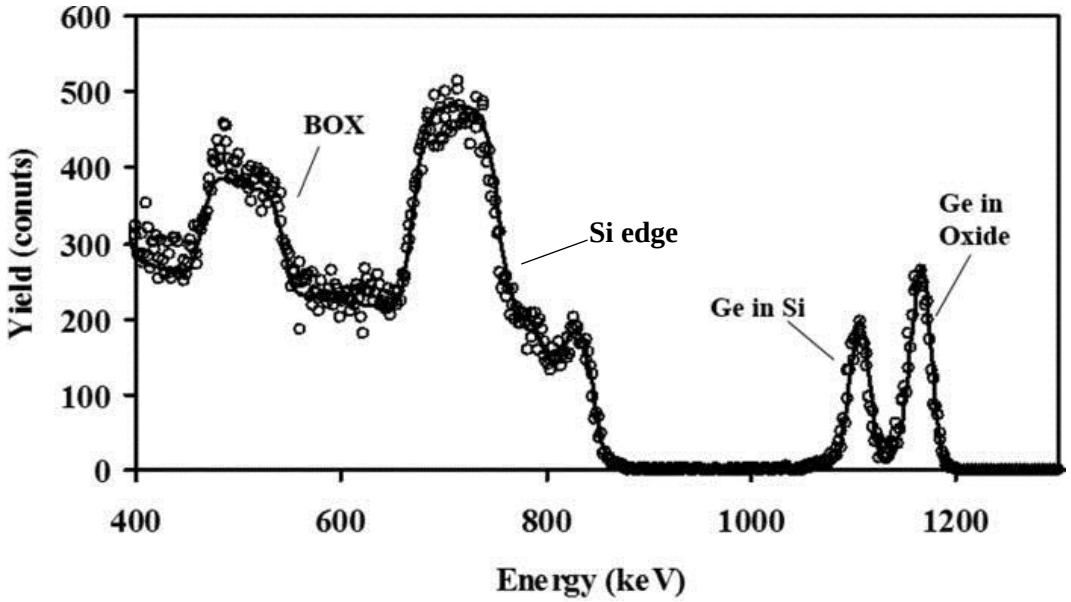

Fig. 3.5 RBS spectra of a 220 nm sample implanted and subsequently oxidized for 70 minutes at 870 °C. The markers are the experimental data and the line is the spectra generated using SIMNRA.

the implantation process. The two Ge peaks in Fig. 3.5 show the incorporation of Ge into the growing oxide layer, and the retention of Ge in the SiGeOI layer. The total retained Ge following the 870 °C oxidation is 4.7×10^{16} cm^{-2}, suggesting an approximate further 3% Ge loss during the primary oxidation step, due to Ge evaporation in the early stages of the process. Of the total retained Ge dose, post- 870 °C oxidation, approximately 60% was incorporated into the oxide.

Fig. 3.6 shows the profile of Ge for the 870 °C oxidized sample determined by fitting the RBS data, while the solid line represents simulated results obtained from the TCAD modeling described in section 3.2. Using the segregation 'switch' it was found that Ge was rejected from the growing oxide for the first 27 minutes of oxidation time at

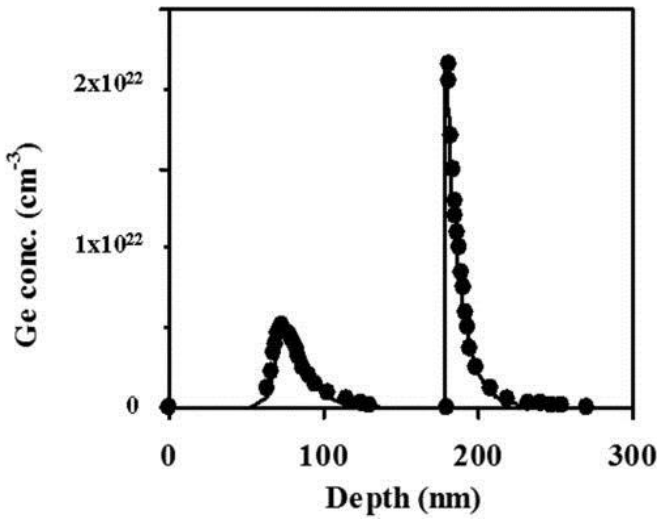

Fig. 3.6 Measurement and simulation of the Ge profile following wet oxidation at 870 °C for 70 minutes. The markers are experimental data and the line the simulation.

870 °C (segregation switch set to ON); incorporated into the oxide for 6 minutes (segregation switch set to OFF); then rejected from the oxide for the remaining 36 minutes (segregation switch returned to ON). The quality of the fit to the experimental

data, shown in Fig. 3.6, obtained with this binary empirical simulation leads to two important conclusions. First, the fit to the Ge profile in the oxide with no segregation at all during the narrow time window when Ge is incorporated in the growing oxide supports the thesis that segregation alone is not the dominant process determining Ge incorporation into the growing oxide. While it should be noted that the ON/OFF segregation switch can be useful as an empirical tool to fit the data, not only is segregation consideration not predictive of the conditions for Ge incorporation/rejection but it is actually physically incorrect in that when Ge is incorporated into the oxide it is incorporated at the same concentration as the Ge present at the surface. Second, if the top 65 nm of the sample (SiO_2) where there is no Ge in the oxide is momentarily ignored, the behavior of the Ge is more consistent with the predictions of the kinetic model of Rabie et al. [9]. That model is based on the assumption that Ge and Si are both oxidized simultaneously at similar rates (although Si oxidation is moderately faster) but that a portion of the Ge is then replaced in the oxide through a replacement reaction that removes GeO_2 and forms SiO_2 in its place. The amount of Ge in the oxide is determined by the rate of this reaction, the instantaneous oxidation rate, and the availability of Si at the growth interface, which is in turn controlled by the diffusion behavior of Si in the SiGe layer. The incorporation of Ge is therefore better explained by a rapid oxidation rate compared with the diffusion of Si to the interface and then drops as the oxide thickness increases slowing the arrival rate of oxidant at the interface compared with that of Si. This explanation also provides insight regarding the initial 65 nm Ge-free oxide for the 870 °C oxidation. The first 27 minutes of oxidation occur during a period that includes

the solid phase regrowth of the implantation amorphized SiGeOI layer, and subsequently a period in which residual defects persist. In the highly defective layer, both the reaction rate and the diffusivity of Si to the surface would be significantly higher than for the recrystallized layer [16] so that the replacement reaction would be sufficient to replace any Ge in the oxide. Similar enhanced diffusivity is evidenced by the data in Fig. 3.3 for a time period consistent with 27 minutes, i.e. the period of time in which excess defects are present in the SiGeOI layer for the 900 °C oxidation.

3.3.2 Oxide growth and Ge profiles for 900, 1000, 1080 °C secondary oxidations

As previously explained, it was deemed preferable to initially oxidize all samples at 870 °C for 70 minutes in order to cap the SiGe layer and thus prevent majority evaporation of Ge during the condensation process. Even so, it should be noted that this primary oxidation results in ~60% of the implanted Ge being incorporated into the grown oxide in a somewhat complex process for which detailed, quantitative explanation is beyond the physically meaningful capabilities of the TCAD model used. It is anticipated that future experimental and theoretical work will permit an optimized primary oxidation in which suitable capping is achieved without a relatively large fraction of Ge-oxide incorporation.

The Ge profile measured following the primary oxidation becomes the starting condition for all subsequent secondary oxidations. In Fig. 3.7 the experimentally determined profile of Ge in the SiGeOI layer of the sample which was subjected to a secondary oxidation at 1080 °C for 20 minutes is shown. The Ge is piled-up at the

$SiGe/SiO_2$ interface, here located at 395nm from the sample surface (i.e. the grown oxide has a thickness of 395nm). The solid line is the simulated profile obtained using the model described in section 3.2, albeit with the segregation switch ON during the secondary oxidation, thus enforcing a complete rejection of the Ge from the oxide. It is

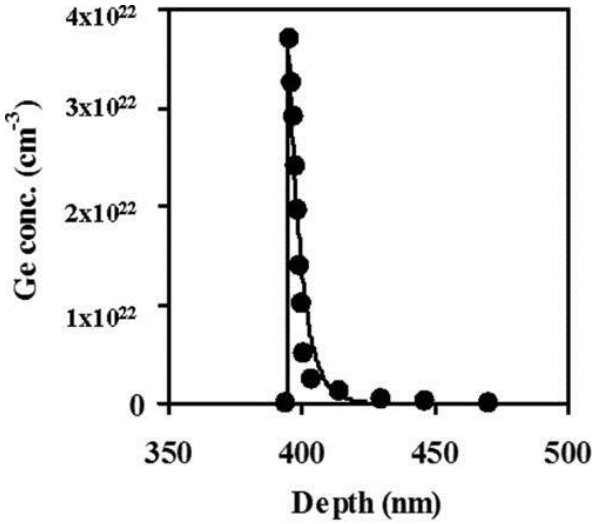

Fig. 3.7 Measurement and simulation of the Ge profile in SiGe layer, following secondary oxidation at 1080 °C for 20 minutes. The markers are experimental data and the line is simulation.

noted that Ge remains present in the oxide with the same profile as that shown in Fig. 3.6 (following primary oxidation) although it is not shown in Fig. 3.7 as to highlight the agreement of the experimental and simulated profiles. Such agreement is representative of that obtained for all secondary oxidations indicating that the model (which in this case is determined by the fitted oxidation rate and Ge diffusivity) is physically representative of the processes which determine the Ge concentration profile, and thus offer a means for predictive determination.

Fig. 3.8 shows the peak Ge concentration at the $SiO_2/SiGe$ interface as a function of temperature and secondary oxidation time, while Fig. 3.9 shows the simulated oxide thickness and experimental values as a function of temperature and oxidation time.

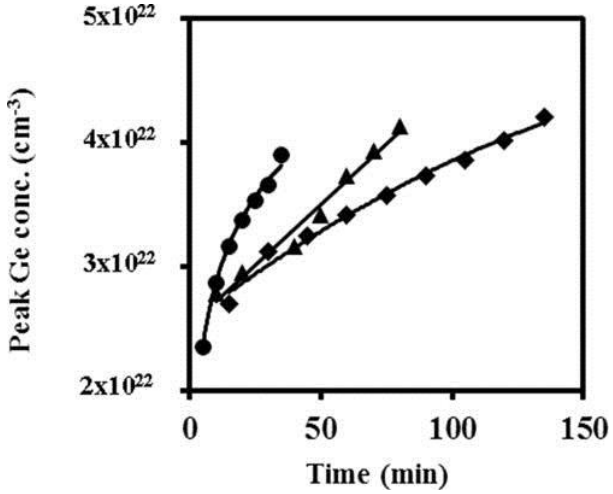

Fig. 3.8 Peak concentration of Ge at the oxide/SiGeOI interface as a function of secondary oxidation time for 900 °C (diamonds), 1000 °C (triangles), and 1080 °C (circles). The lines are guides to the eye. The model described in section 3.2 replicated the experimental values by using the effective Ge diffusivity values summarised in Fig. 3.3.

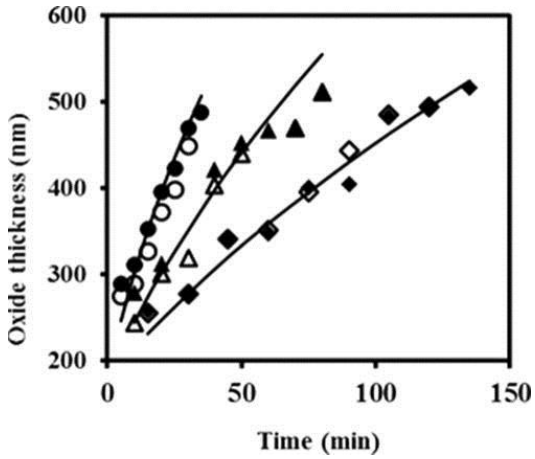

Fig. 3.9 Measured using RBS (solid markers); measured using ellipsometry (open markers); and simulated (lines) oxide thickness as a function of time following secondary oxidations at 900 °C (diamonds), 1000 °C (triangles), and 1080 °C (circles). The simulated values were obtained using the modified linear rate constant values summarised in Fig. 3.2.

3.3.3 TEM and STEM images

Fig. 3.10 shows a representative High Resolution-TEM (HR-TEM) image; in this case for the SiGe layer formed after annealing at 1080 °C for 20 minutes where the peak concentration of Ge is approximately 75 at- %. The image confirms the crystalline nature

of the sample indicating the successful seeding of the SiGe layer from the underlying Si not amorphised by the Ge^+ implantation. While no attempt was made in this work to quantify residual defects (such as dislocations) the volume probed was found to be predominantly defect free, and as such the image is representative of the quality of this sample.

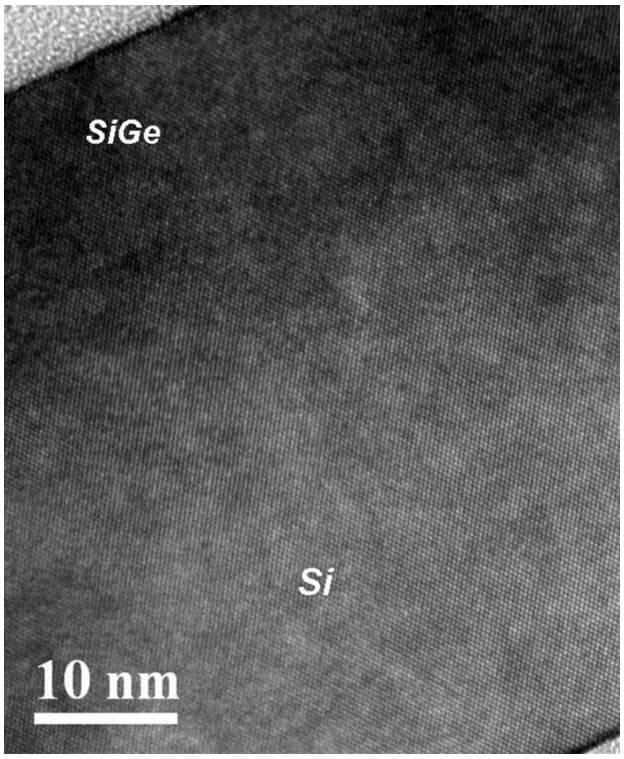

Fig. 3.10 HR-TEM image of sample annealed at 1080 °C for 20 minutes. The region associated with the SiGe is indicated, as is that which predominantly consists of Si. The SiGe region extends approximately 20nm from the oxide/SiGe interface with a profile consistent with the images shown in Fig. 3.11.

Fig. 3.11 shows STEM images of the same sample in both low and moderate magnification. The nature of the STEM measurement emphasizes contrast for species of different mass. Further, the species giving rise to the contrast can be determined using EDS. Fig. 3.11 shows the EDS spectra for Ge superimposed onto the STEM images thus providing an unambiguous confirmation that the contrast in the STEM is due to the

incorporated Ge. In this way, STEM images can be compared with profiles obtained via RBS to confirm the presence of the mixed Ge/Si band. In the case of STEM the band is

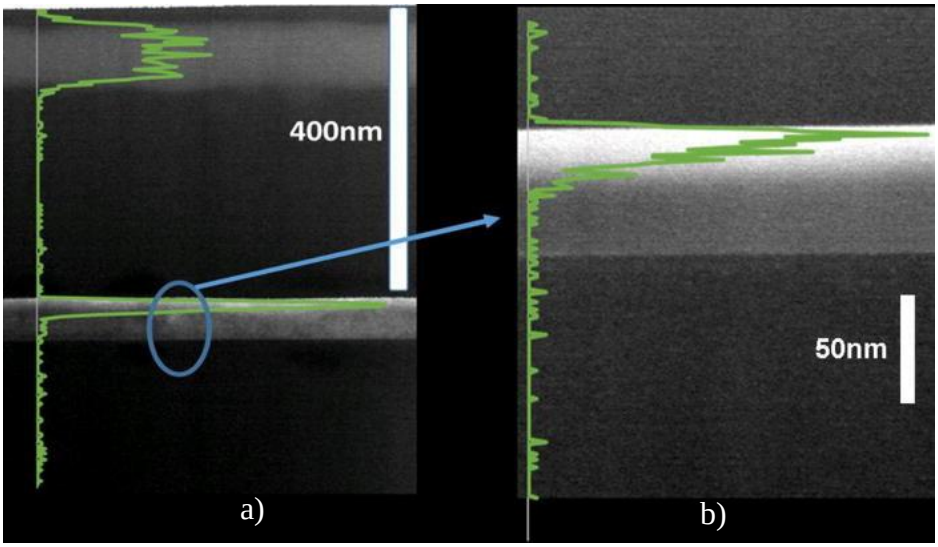

Fig. 3.11 a) STEM image of sample oxidized at 1080 °C for 20 minutes with Ge EDS spectra superimposed (green solid line) indicating a mixed oxide band and Ge profile in SiGe layer and b) higher magnification STEM image of same sample indicating SiGe layer only, again with Ge profile superimposed. The Ge EDS profile indicates the relative depth distribution only with no attempt to provide a quantification of the Ge concentration.

measured to have a width ~85nm in the grown oxide at a depth of ~30nm from the sample surface. It is noted that for the lower magnification image in Fig 3.11 the Ge contained in the oxide shows signs of non-uniformity. The high concentration of Ge in these samples gives rise to an oxidation temperature that would increase in excess of the compound melt temperature for the 1080 °C oxidations. This has been shown previously to result in non-uniform agglomeration of condensed Ge [17]. No such agglomeration within the SiGe is seen in the samples shown in Fig. 3.11.

3.3.4 Raman spectroscopy

Fig. 3.12 shows the evolution of the Raman scattering spectra with thermal budget for samples receiving secondary oxidation anneals at 900 °C, for 135 minutes, 1000 °C

for 60 minutes and 1080 °C for 35minutes. Raman measurements were performed after removal of the top (grown) oxide via etching in dilute HF acid. In order to enable direct comparison of the Si-Si alloy scattering in the SiGe layer with the Ge-Ge scattering peak, contributions from the underlying (pure) Si layers, owing to their different frequency, were subtracted from the total scattering spectra, after fitting these with a Lorentzian line-shape function. All of the samples exhibit peaks associated with the Ge-Ge, Si-Si and SiGe scattering with the peak positions varying during the oxidation. In SiGe alloys the scattering peak positions are known to be sensitive to both strain and composition, in this work the Ge-Ge, Si-Si and SiGe peaks vary from 284-295 cm^{-1}, 402-413 cm^{-1} and 497-511 cm^{-1} respectively. As a result of the variation it is difficult to extract reliable values for either strain or concentration as both may be changing. However, one can use the relative scattering intensities as a means to determine the compositional fraction because, in a simplified treatment of the SiGe layer as a purely random mixture of Si and Ge atoms, the probability of finding either Si-Si or Ge-Ge vibrating pairs as a function of the Ge composition, is simply proportional to the relative numbers of corresponding bond types [18]. If the Raman scattering intensity for either of these modes is then assumed to be proportional to the number of these vibrating pairs within the layer, then the ratio of scattering intensities should vary according to:

$$\frac{I_{\mathrm{Ge-Ge}}}{I_{\mathrm{Si-Si}}} = \frac{x^2}{1-x^2} \tag{3.1}$$

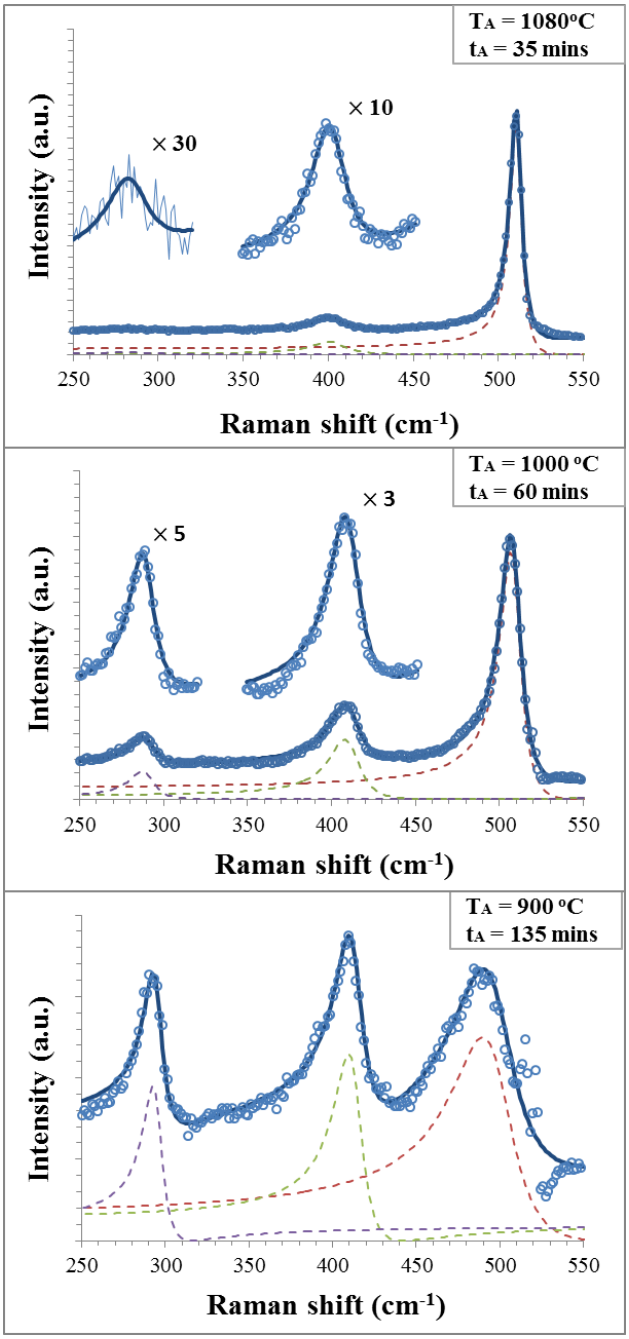

Fig. 3.12 Evolution of the scattering spectra from the SiGe layer as a function of thermal budget during oxidation annealing. The contribution from the Si substrate has been subtracted to enable direct comparison of the Si-Si alloy scattering in the SiGe layer with the Ge-Ge scattering peak. Integrated peak intensities and frequencies were determined from the fitted lines, which are asymmetric (Fano) line-shape functions, after Ref. [23].

This function reveals the Ge concentration in the SiGe layers to be ~44 at-% at 900 °C, ~26 at-% at 1000 °C and ~12 at-% at 1080 °C. This result appears to be in disagreement with the RBS measurements which indicate (for example) that the peak concentration for a sample annealed at 900 °C for 135 minutes, is close to 95 at-%. The consistently lower Ge composition determined using single wavelength excitation (UV) Raman scattering is attributed to the narrow width of the SiGe layer and a consequent optical probing of the tail of the Ge distribution. That is to say, although the two techniques appear to be reporting very different Ge compositional fractions, this is most likely only the result of probing different regions of the highly non-uniform (that is, non-uniform in depth) thin SiGe layer. Having determined the Ge compositional fraction at a specific depth using the ratio of integrated Raman peaks, the peak positions of the three main scattering modes; Si-Si, Si-Ge and Ge-Ge were examined in order to determine whether and to what degree there is any inherent strain in the SiGe layer. The precise scattering frequency of these peaks depends on both layer composition and strain, ε according to the following empirical relations [19], [20]:

$$\omega(x,\varepsilon)_{\mathrm{Si-Si}} = 520.5 - 70\,x + b_{\mathrm{Si}}\,\varepsilon \tag{3.2}$$

$$\omega(x,\varepsilon)_{\mathrm{Si-Ge}} = 400.1 - 24.5\,x - 4.5\,x^{2} - 33.5\,x^{3} + b_{\mathrm{SiGe}}\,\varepsilon \tag{3.3}$$

$$\omega(x,\varepsilon)_{\mathrm{Ge-Ge}} = 282.5 + 19\,x + b_{\mathrm{Ge}}\,\varepsilon \tag{3.4}$$

where the coefficients b_m are phenomenological parameters that depend on the elastic constants of the specific materials; Si, SiGe and Ge. Taking the coefficients determined previously by Pezzoli et al [21] to be: b_{Si} = -730 cm^{-1}, b_{SiGe} = -570 cm^{-1} and b_{Ge} = -450 cm^{-1} the strain for all three modes is found to be in highly consistent

agreement. Fig. 3.13 is the graphical representation of Eqs. (3.2)-(3.4) illustrating the Raman shift with Ge alloy composition and strain for the three main optical phonon modes in SiGe. The measured peak positions and Ge alloy compositions that have been determined here indicate that where the Ge fraction is highest, (i.e. for the measurement taken from the sample annealed at 900 °C for 135 minutes) there exists a significant compressive strain ε ~1%. As the thermal budget is increased, the combined intermixing of the Si with the SiGe layer (or out diffusion of Ge from that region) acts to reduce this compressive strain so that for annealing at 1000 °C for 60 minutes, ε is reduced to ~0.7% and for the sample annealed at 1080 °C for 35 minutes, it is almost completely relaxed (within experimental error). These increased values of compressive strain with Ge composition in ultra-thin SiGeOI layers are in very good agreement with previous work on similar ultra-thin SiGe layers [22], although contrary to the implantation-condensation samples of Ref. [2].

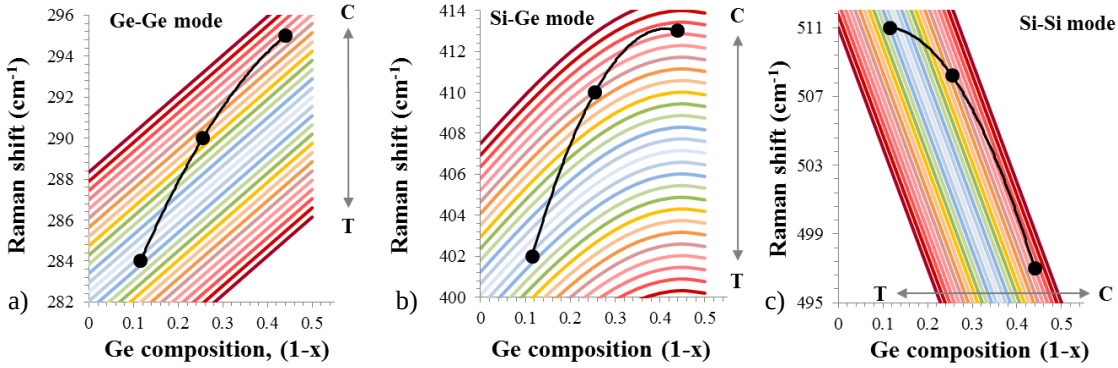

Fig. 3.13 Predicted Raman shift for a) Ge-Ge, b) Si-Ge and c) Si-Si alloy modes as function of Ge concentration (1-x) for various values of strain, either tensile (T) or compressive (C) in the range of 1.3% tensile strain to 1.3% compressive strain in 0.1% increments. The points determined for the samples studied here (connected by lines to guide the eye) show a strongly correlated behaviour for all three modes; a significant (~1%) compressive strain in the sample with the highest Ge content, ~44 at-% (annealed at 900 °C for 135 minutes) is gradually relaxed as the Ge fraction diminishes with thermal budget during annealing.

3.3.5 Discussion

The data in Fig. 3.7 demonstrate that a maximum peak concentration approaching 95 at-% has been obtained which suggests a technique capable of producing high Ge content SiGeOI. In order to construct a completely predictive, physically-based model, a full system of equations must be solved as in Py et al. [24] and Uematsu [25] to take into account the behavior of point defects and conservation of lattice site density as in the model of Hasanuzzaman et al. [26], [27]. For the concentrations of Ge used here and in other similar experiments, ignoring the conservation of lattice site density can lead to the unphysical result of a greater number of substitutional atoms than lattice points, for example. Further, it was not attempted in this study to model the diffusion behavior of Ge in the oxide or to experimentally determine the state of Ge in the oxide to confirm the mixed oxide expected if the Rabie model [9] is correct. In order to produce such results a full model of the process described here would require the use of kinetic oxidation simulation, the full interdiffusion of Si and Ge, including the conservation of lattice site density, and the diffusion of Ge in the oxide. However, the preliminary model presented does shed light on the dominant physical processes of the implantation condensation process, and in a limited sense the model provides predictive capabilities.

3.4 Application of condensation technique in the formation of waveguide photodetectors

3.4.1 Detector fabrication and experimental Methods

Structures (essentially partially fabricated devices) suitable for Ge incorporation via implantation/condensation were fabricated using the IME *A*-Star 220 nm SOI platform. The processing done at IME consisted of Si patterning, N+ and P+ implants to form the p-i-n detector region and a frontside oxide etch to allow for implantation of Ge. Post processing was performed at McMaster University where samples were implanted with a fluence of 2.7×10^{16} cm^{-2} of Ge^{+} ions at 30 KeV. These samples were then oxidized at 900 °C in wet O_2 environment for 5, 15, and 30 minutes respectively. For comparison, unimplanted samples were also oxidized for 5, 15, 30 and 45 minutes. Completion of device fabrication was achieved through contact metallization performed using a Kurt J Lesker sputtering system where 350 nm of aluminum was deposited. Fig. 3.14.a shows a schematic diagram of the final detector where *L* refers to the length of the device and Fig. 3.14.b shows a schematic cross section of the final detector. All devices were characterized using a Luminent laser diode with a central wavelength of 1301.6 nm with a spectral width of 2.9 nm, and an output power of 5.3 mW, driven by a ILX Lightwave LDX-3270B Precision Current Source. Optical coupling was achieved using grating couplers centered around 1310 nm with the coupling loss estimated to be 8.5 dB. Electrical measurements were taken using a Keithly 2400 Source Meter.

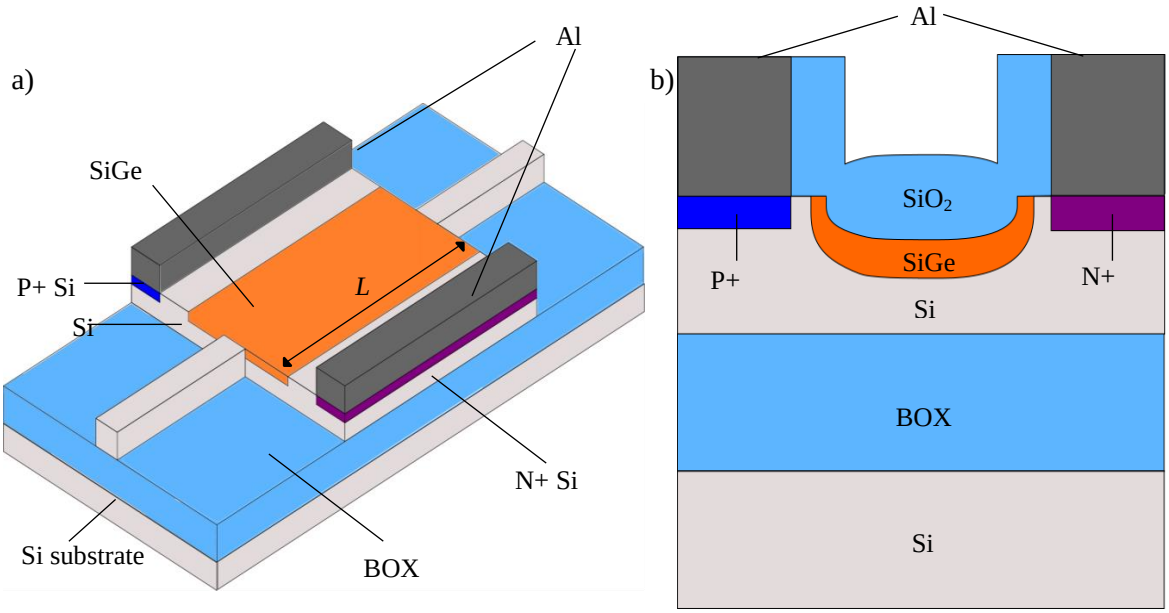

Fig. 3.14 a) Schematic diagram of a detector fabricated via Ge implantion and condensation with top oxide removed for clarity and b) cross-sectional schematic of device.

3.4.2 Optical loss measurements

Loss measurements allow for the comparison of loss due to the presence of Ge, and parasitic loss due to waveguide reduction [28].

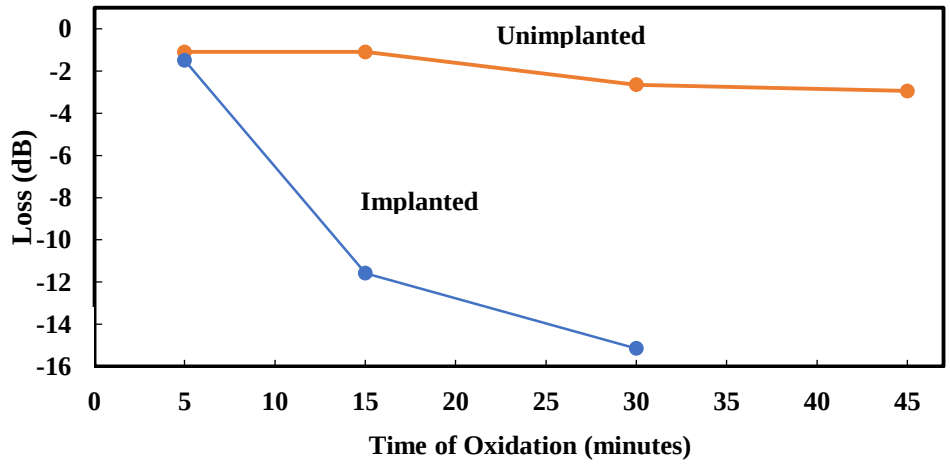

Fig. 3.15 Loss for unimplanted and implanted devices with *L*=250 µm after different lengths of oxidation.

Fig. 3.15 shows the optical loss measurements for both Ge^+ implanted and unimplanted devices with L=250 μm oxidized for various times. Loss increases with oxidation time and while this is consistent with increasing absorption due to an increasing concentration of Ge, additional possible sources of loss must be considered. The size reduction of the waveguide would likely be the largest source of such parasitic loss. Specifically, increasing oxidation will lead to loss caused by modal mismatch between the unoxidized waveguide and the implantated waveguide due to the consumption of Si. While loss for lower oxidation times is comparable for an unimplanted and Ge^+ implanted sample (-1.0dB and -1.5 dB), for longer oxidations the loss is significantly less for an unimplanted sample. This strongly suggests that the dominant loss mechanism is associated with the presence of Ge in the waveguide, and not the reduction of the waveguide size.

3.4.3 Optical to electrical conversion

Fig. 3.16 shows the current-voltage characteristics for a detector with L=250 μm oxidized for 15 minutes and Fig. 3.17 shows the current-voltage characteristics for a detector with L=200 μm oxidized for 30 minutes. As can be seen in both figures, photocurrent is generated under illumination with significantly more photocurrent, a factor of 4, being generated for the sample undergoing the 15 minute oxidation. This is believed to result from a combination of increased detector length, reduced parasitic loss and results from section 3.3.1 where it can be seen that the Ge reaches a peak concentration, inferred from the Ge profile in the oxide, before gradually decreasing and Ge being at a higher concentration at 15 minutes which is consistent with Ref. [29]

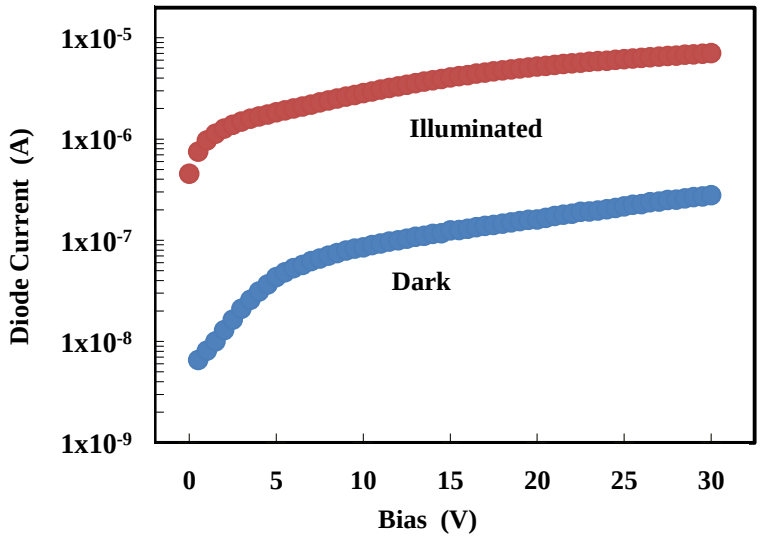

Fig. 3.16 Current – voltage characteristics for a detector with *L*=250 µm, oxidized for 15 minutes, for dark and illuminated conditions.

While these detectors are the first to be reported, to the author's knowledge, demonstrating use of the condensation technique in fabricating a detector,the responsivity of these detectors is quite low, ~0.01 A/W at 30 V reverse bias. Comparatively, Ge-on-Si detectors utilizing directly grown Ge have been demonstrated with responsivities of up to 1 A/W at similar wavelengths [30]. It is noted that such grown Ge detectors are on the order of 1µm in thickness, whereas the Ge layer in the condensation case is on the order of 20nm. While the high speed response of these devices was deemed to be outside the scope of this study we estimate the 3 dB frequency to be approximately 7.6 GHz. This is based on an estimation of the field strength in the depletion region to be $6x10^4$ Vcm^{-1}, which is high enough that the velocity of charge carriers should saturate to ~$1x10^7$ cm/s. Using eqn. 2.11 the transit time across the intrinsic region which is approximately 5 µm should be $5x10^{-11}$ s which corresponds with the 3 dB frequency given above. While the estimated field strength should be sufficient to cause avalanche effects, the impact of

avalanche has been ignored for this calculation as the number of impact ionizations at this field strength will be relatively low. Indeed, the presence of avalanche is difficult to distinguish in Fig. 3.16 suggesting it should not be an important consideration. As might be expected, the 3 dB bandwidth of 7.6 GHz is significantly lower than those for Ge-Si

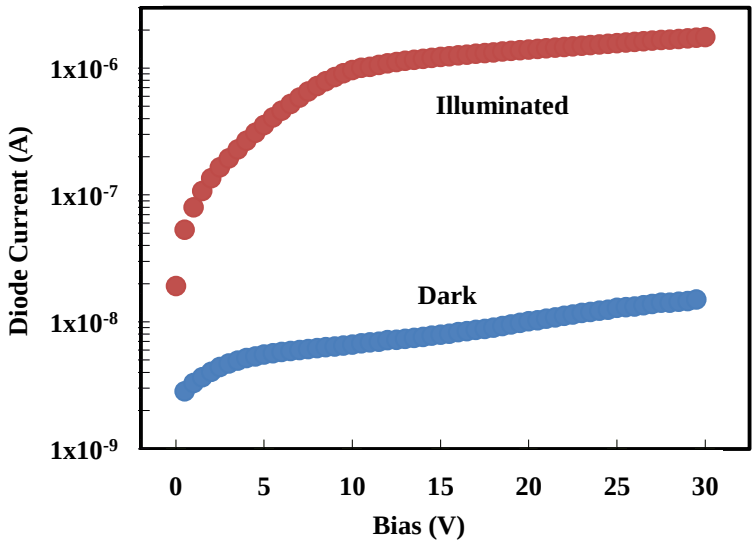

Fig. 3.17 Current – voltage characteristics for a detector with *L*=200 µm, oxidized for 30 minutes, for dark and illuminated conditions.

devices in which the transit distance is <1 µm (compared to the 5 µm in the current detectors) which have been shown to exceed 40 GHz[31]. These results do however demonstrate the first photodetector to be fabricated using the implantation-condensation technique, and suggest that if scaling of the Ge can be achieved, comparable performance with grown Ge devices may be obtained.

3.5 Conclusion

A Ge implantation-condensation technique using Ge-implanted SOI utilizing a two-step wet oxidation process has been demonstrated in this chapter. The experimental

matrix is preceded by an initial oxidation at 870 °C to minimize evaporation of Ge, followed by a higher temperature oxidation at either 900 °C, 1000 °C or 1080 °C for incremental periods of time in order to examine the formation of the oxide and Ge layer over time. Samples were characterized using RBS analysis to examine the composition and thickness of the oxide and Ge layer and then compared with a semi-empirical model. The dominant fitting parameters in this model are a modified segregation boundary condition and a linear oxidation rate enhancement which are attributed to the replacement reaction of Ge in oxide with Si; and an enhanced diffusion coefficient for Ge which is consistent with transient enhanced diffusion. TEM and STEM analysis of a representative sample shows that the SiGe is relatively uniform and defect free, while EDS profile data is consistent with the RBS anaylsis of the same sample. Raman spectroscopy shows that significant compressive stress can be induced in the SiGe layers at levels consistent with previous condensation studies in which epitaxially grown SiGe provided the primary structure. Furthermore, using the ion implantation and condensation of Ge technique a CMOS compatible detector at 1310 nm was fabricated. Both loss and electrical measurements of these devices were taken, with the sample oxidized for 15 minutes found to have the highest photocurrent which is attributed to several different factors.

References

[1] B. E. Deal and A. S. Grove, “General relationship for the thermal oxidation of silicon,” *J. Appl. Phys.*, vol. 36, no. 12, pp. 3770–3778, 1965.

[2] D. Y. Choi, B. Luther-Davies, T. Kim, and R. Elliman, “Germanium-on-insulator

fabricated by ion implantation and dry oxidation technique," *Proc. IEEE Conf. Nanotechnol.*, pp. 1668–1672, 2011.

[3] M. Mayer, *SIMNRA User's Guide, Report IPP 9/113*. Max-Planck-Institute fur Plasmaphysik, Garching, Germany, 1997.

[4] Synopsys, *Synopsys User Manuals, Advanced Calibration for Process Simulation UserGuide*. 2016.

[5] F. K. LeGoues, R. Rosenberg, T. Nguyen, F. Himpsel, and B. S. Meyerson, "Oxidation studies of SiGe," *J. Appl. Phys.*, vol. 65, no. 4, pp. 1724–1728, 1989.

[6] E. C. Frey, N. R. Parikh, N. Yu, M. L. Swanson, B. Patnaik, and W. K. Chu, "Transition between Ge segregation and trapping during high-pressure oxidation of Ge x Si 1− x /Si," *J. Appl. Phys.*, vol. 74, no. 7, pp. 4750–4755, 1993.

[7] M. Nicolet, W. S. Liu, N. M. Abuhadba, C. R. Aita, E. W. Lee, V. Arbet-Engels, and K. L. Wang, "Wet oxidation of GeSi at 700 °C," *J. Appl. Phys.*, vol. 71, no. 8, pp. 4015–4018, 1992.

[8] J. P. Zhang, P. L. F. Hemment, S. M. Newstead, A. R. Powell, T. E. Whall, and E. H. C. Parker, "A comparison of the behaviour of Si0.5Ge0.5 alloy during dry and wet oxidation," *Thin Solid Films*, vol. 222, no. 1–2, pp. 141–144, 1992.

[9] M. A. Rabie, Y. M. Haddara, and J. Carette, "A kinetic model for the oxidation of silicon germanium alloys," *J. Appl. Phys.*, vol. 98, no. 7, 2005.

[10] T. David, A. Benkouider, J. N. Aqua, M. Cabie, L. Favre, T. Neisius, M. Abbarchi, M. Naffouti, A. Ronda, K. Liu, and I. Berbezier, "Kinetics and Energetics of Ge Condensation in SiGe Oxidation," *J. Phys. Chem. C*, vol. 119, no. 43, pp. 24606–

24613, 2015.

[11] M. A. Rabie, “Kinetics of the oxidation of Silicon Germanium,” McMaster University, 2006.

[12] Y. Dong, Y. Lin, S. Li, S. McCoy, and G. Xia, “A unified interdiffusivity model and model verification for tensile and relaxed SiGe interdiffusion over the full germanium content range,” *J. Appl. Phys.*, vol. 111, no. 4, 2012.

[13] A. Claverie, T. Fühner, F. Cristiano, P. Pichler, N. E. B. Cowern, C. J. Ortiz, and B. Colombeau, “A physically based model for the spatial and temporal evolution of self-interstitial agglomerates in ion-implanted silicon,” *J. Appl. Phys.*, vol. 96, no. 9, pp. 4866–4877, 2004.

[14] F. A. Wolf, A. Martinez-Limia, D. Stichtenoth, and P. Pichler, “Modeling the annealing of dislocation loops in implanted c-Si solar cells,” *IEEE J. Photovoltaics*, vol. 4, no. 3, pp. 851–858, 2014.

[15] N. R. Zangenberg, J. Lundsgaard Hansen, J. Fage-Pedersen, and A. Nylandsted Larsen, “Ge Self-Diffusion in Epitaxial Si1-xGex Layers,” *Phys. Rev. Lett.*, vol. 87, no. 12, p. 125901, 2001.

[16] F. Strauß, L. Dörrer, T. Geue, J. Stahn, A. Koutsioubas, S. Mattauch, and H. Schmidt, “Self-Diffusion in Amorphous Silicon,” *Phys. Rev. Lett.*, vol. 116, no. 2, pp. 1–6, 2016.

[17] H. J. Oh, K. J. Choi, W. Y. Loh, T. Htoo, S. J. Chua, and B. J. Cho, “Integration of GaAs epitaxial layer to Si-based substrate using Ge condensation and low-temperature migration enhanced epitaxy techniques,” *J. Appl. Phys.*, vol. 102, no. 5, 2007.

[18] F. Pezzoli, L. Martinelli, E. Grilli, M. Guzzi, S. Sanguinetti, M. Bollani, H. D. Chrastina, G. Isella, H. Von Känel, E. Wintersberger, J. Stangl, and G. Bauer, "Raman spectroscopy of Si1-xGex epilayers," *Mater. Sci. Eng. B Solid-State Mater. Adv. Technol.*, vol. 124–125, no. SUPPL., pp. 127–131, 2005.

[19] G. Capellini, M. De Seta, Y. Busby, M. Pea, F. Evangelisti, G. Nicotra, C. Spinella, M. Nardone, and C. Ferrari, "Strain relaxation in high Ge content SiGe layers deposited on Si," *J. Appl. Phys.*, vol. 107, no. 6, 2010.

[20] F. Pezzoli, E. Bonera, E. Grilli, M. Guzzi, S. Sanguinetti, D. Chrastina, G. Isella, H. von Känel, E. Wintersberger, J. Stangl, and G. Bauer, "Raman spectroscopy determination of composition and strain in Si1 - x Gex / Si heterostructures," *Mater. Sci. Semicond. Process.*, vol. 11, no. 5, pp. 279–284, 2008.

[21] F. Pezzoli, E. Bonera, E. Grilli, M. Guzzi, S. Sanguinetti, D. Chrastina, G. Isella, H. Von Känel, E. Wintersberger, J. Stangl, and G. Bauer, "Phonon strain shift coefficients in Si1-x Gex alloys," *J. Appl. Phys.*, vol. 103, no. 9, 2008.

[22] T. Tezuka, N. Hirashita, Y. Moriyama, S. Nakaharai, N. Sugiyama, and S. I. Takagi, "Strain analysis in ultrathin SiGe-on-insulator layers formed from strained Si-on-insulator substrates by Ge-condensation process," *Appl. Phys. Lett.*, vol. 90, no. 18, 2007.

[23] Naoki Fukata, Keisuke Sato, Masanori Mitome, Yoshio Bando, Takashi Sekiguchi, Melanie Kirkham, J. Hong, Z. L. Wang, and R. L. Snyder, "Doping and Raman characterization of boron and phosphorous atoms in Ge nanowires ," *ACS Nano*, vol. 4, no. 7, pp. 3807–3816, 2010.

[24] M. Py, J. P. Barnes, P. Rivallin, A. Pakfar, T. Denneulin, D. Cooper, and J. M.

Hartmann, “Characterization and modeling of structural properties of SiGe/Si superlattices upon annealing,” *J. Appl. Phys.*, vol. 110, no. 4, 2011.

[25] M. Uematsu, “Self-diffusion and dopant diffusion in germanium (Ge) and silicon-germanium (SiGe) alloys,” in *Silicon Germanium (SiGe) Nanostructures*, Y. Shiraki and N. Usami, Eds. Cambridge, UK: Woodhead Publishing, 2011, pp. 299–337.

[26] M. Hasanuzzaman and Y. M. Haddara, “Modeling silicon-germanium interdiffusion by the vacancy exchange and interstitial mechanisms,” *J. Mater. Sci. Mater. Electron.*, vol. 19, no. 6, pp. 569–576, 2008.

[27] M. Hasanuzzaman, Y. M. Haddara, and A. P. Knights, “Modeling germanium diffusion in Si1-x Gex /Si superlattice structures,” *J. Appl. Phys.*, vol. 105, no. 4, 2009.

[28] J. K. Doylend, P. E. Jessop, and A. P. Knights, “Silicon photonic resonator-enhanced defect-mediated photodiode for sub-bandgap detection,” *Opt. Express*, vol. 18, no. 14, pp. 14671–14678, 2010.

[29] K. Hossain, O. W. Holland, F. U. Naab, L. J. Mitchell, P. R. Poudel, J. L. Duggan, and F. D. McDaniel, “Dose-dependent thermal oxidation of Ge+-implanted silicon,” *Nucl. Instruments Methods Phys. Res. Sect. B Beam Interact. with Mater. Atoms*, vol. 261, no. 1–2 SPEC. ISS., pp. 620–623, 2007.

[30] M. Morse, O. Dosunmu, T. Yin, Y. Kang, H. D. Liu, G. Sarid, E. Ginsburg, R. Cohen, S. Litski, and M. Zadka, “Performance of Ge/Si receivers at 1310 nm,” *Phys. E Low-Dimensional Syst. Nanostructures*, vol. 41, no. 6, pp. 1076–1081, 2009.

[31] L. Vivien, J. Osmond, J.-M. Fédéli, D. Marris-Morini, P. Crozat, J.-F. Damlencourt, E. Cassan, Y. Lecunff, and S. Laval, “42 GHz pin Germanium

photodetector integrated in a silicon-on-insulator waveguide," *Opt. Express*, vol. 17, no. 8, p. 6252, 2009.

Chapter 4 – Photodetection at extended wavelengths around 2 μm

Overview

This chapter presents results of work to develop p-i-n Ge detectors suitable for extended wavelength operation. An initial hypothesis (following previous work by past members of the Knights research group) was that mid-bandgap lattice defects would enhance the absorption of Ge at wavelengths close to and beyond its optical bandgap. This is shown to be incorrect, but the experimental work to reach this conclusion resulted in the discovery that as-grown Ge-on-Si does have a reasonable responsivity up to a wavelength of 2000 nm.

First in this chapter is a discussion presenting the interest in a new optical communication window based on the use of a Thulium Doped Fiber Amplifier (TDFA). The design and fabrication of Ge-on-Si waveguide detectors is then described (both with and without intentionally defected lattices). The operation of the implanted Ge detectors is then described. This is followed by an examination of the high-speed operation, responsivity, and absorption coefficient for an undefected detector between 1550 to 1640 nm and 1850 to 2000 nm. The chapter concludes with a discussion on the potential uses of Ge in the TDFA enabled optical communication band. Results from this work have been reported by the author in the following Journal publication and Conference proceedings:

R. Anthony, D. Hagan, D. Genuth-Okon, J. Mullins, I. F. Crowe, M. P. Halsall, and A. P. Knights, "Extended wavelength responsivity of a germanium photodetector integrated with a silicon waveguide" *IEEE Journal of Lightwave Technology*, 2019 (Submitted)

4.1 Detection using Ge beyond 1550 nm

4.1.1 Introduction

The interest in integrated functionality around wavelengths of 2 μm is fueled by the relatively recent suggestion that a new communication window at these extended wavelengths could be developed [1]. Such a band would be centered on the output of the Thulium-Doped-Fiber-Amplifier (TDFA) [2] which has been shown to provide broad amplification potentially from 1700 nm to 2100 nm, a range wider than that associated with the EDFA.

The optical bandgap of Ge provides for excellent responsivity in the *O* and *C* bands, detection in the *L*-band (particularly at longer wavelengths) is reduced, demonstrating considerable "roll-off". Increasing the responsivity of integrated Ge detectors beyond the optical direct band-edge has been achieved previously through the introduction of tensile strain, which has the effect of shrinking the optical bandgap of Ge [3]. For detection of wavelengths beyond the *L*-band, it is generally assumed that the reduced bandgap of binary, Ge-based alloys is required. For example, Dong et al. have shown that GeSn can be integrated with Si substrates, with surface illuminated detectors providing a response of 0.04 A/W at a wavelength of 1900 nm [4]. However, very little work has been done on characterizing Ge at wavelengths beyond 1620 nm.

4.1.2 Defect Mediated Detection

A technique which has seen considerable success for detection in Si in both EDFA and TDFA bands is that of defect mediated detection [5]. This technique operates on the principle that when defects are introduced into a crystal lattice so called "deep-level states" are introduced in between the conduction and valence bands. Electrons can then be thermally excited from the valence band to the deep level, and then optically excited to the conduction band as shown in Fig. 4.1. The same process can also occur in reverse with an optical excitation to the deep level followed by a thermal excitation to the conduction band. This allows for detection in Si at sub-band gap wavelengths. Using this technique monolithic waveguide detectors in Si have been fabricated with bandwidths in excess of 30 GHz, while the excellent amplifying properties of Si permit high-field responsivities in excess of 5 A/W [6] for a wavelength of 1550 nm. More recently, this technique has been shown to permit detection of wavelengths up to 2800 nm [7]. Despite the successes of defect mediated detection in Si, there has been no work exploring the potential of defect mediated detection in Ge.

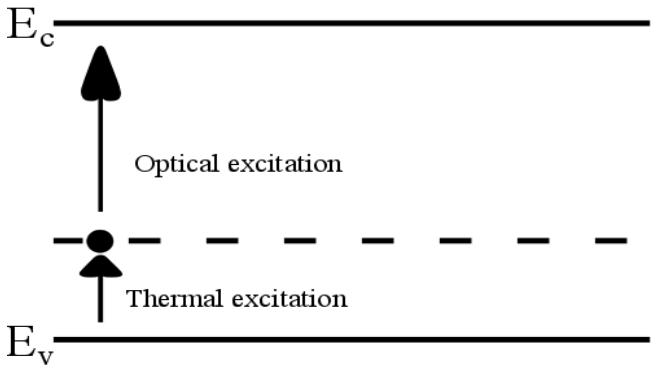

Fig. 4.1 A schematic diagram of the optical process that occurs in defect mediated detection.

4.1.3 Device Fabrication and Characterization

Devices for which results are reported in this study were fabricated at IME A-Star, Singapore using their Silicon Photonics MPW process, based on 248 nm deep-ultraviolet lithography. Access to the MPW was facilitated by CMC Microsystems. Fig. 4.2 shows schematic representation of the detector structures used in this work. The buried oxide (BOX) is 2 μm thick, the Si layer is 220 nm and the Ge layer is 500 nm. An oxide cladding of 2.1 μm thickness (not represented in Fig. 4.2) was used to encapsulate the structure. The direct growth of Ge on the Si allows for integration of the detector with a Si waveguide formed in the Si layer. The waveguide tapers from a width of 5 μm to 0.5 μm over a length of 250 μm, and eventually terminates at a nanotaper coupler, designed for efficient coupling of light from a single-mode-fiber. In this way, light from the input fiber is evanescently coupled into the Ge via the Si waveguide and taper. In some cases, prior to the Ge detector carrier extraction region, (labelled as L_{DET} in Fig. 4.2) a passive Ge layer was incorporated (labelled in Fig. 4.2 as L_{Ge}). The length of the detector (L_{DET}) varied from 5 to 500 μm; while L_{Ge} was varied from 0 to 492 μm. The width of the Ge was 5 μm (consistent with the wider end of the Si waveguide taper). Low impedance connection to the Ge detector was achieved via top doping of the Ge using phosphorus (*n*-type); and side doping of the Si using boron (*p*-type). Similar devices have been described previously in some detail [8].

The detectors were characterized at two wavelength ranges: 1550 to 1640 nm, supplied by a Keysight 8164A Tunable Laser; and 1850 to 2000 nm, supplied by a Sacher Lasertechnik tuneable Littman/Metcalf laser. In both ranges, linearly-polarized light was

launched into single-mode fiber, polarization-controlled using polarization-paddles, and edge coupled via tapered fiber into the detector via a 180 nm wide inverse-nanotaper. For the short wavelength range, the amount of optical power coupled to the Ge-integrated waveguides was determined by applying a 3.1 dB insertion loss, measured independently using Si waveguide test structures. For the long wavelength range, a similar method was employed by applying a 5.1 dB insertion loss, also determined using Si test waveguides. The relative increase in coupling loss for the longer wavelength range reflects the difference in mode size for each range.

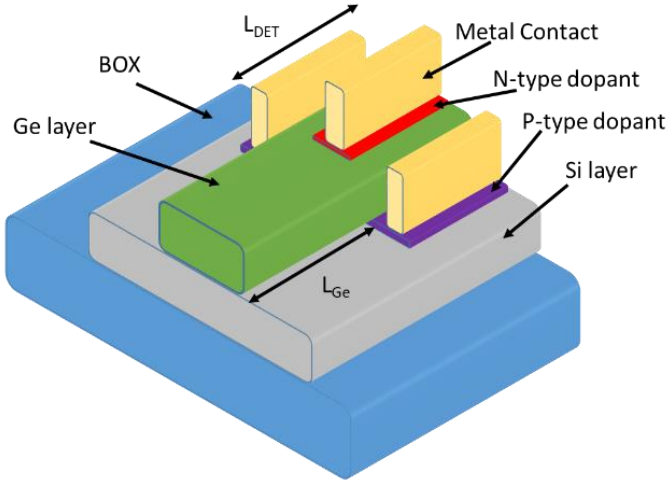

Fig. 4.2 – Schematic layout of the detector structure used in this work.

To introduce defects into the structures, B^+ ions were implanted into the samples at an energy of 1.5 MeV, which was determined using Stopping and Range of Ions in Matter simulations [9]. The dose of implantation was chosen to be similar to previous studies done on Si and ranged from $1x10^{12}$ to $3x10^{13}$ cm^{-2}[10]. Implantation was performed using the 1.7 MV Tandetron Accelerator Facility at Western University.

4.1.4 Defect Mediated Detection in Ge

Following implantation, dark current is seen to increase as a function of implantation dose, as shown in Fig 4.3, indicating that defects were successfully introduced into the Ge.

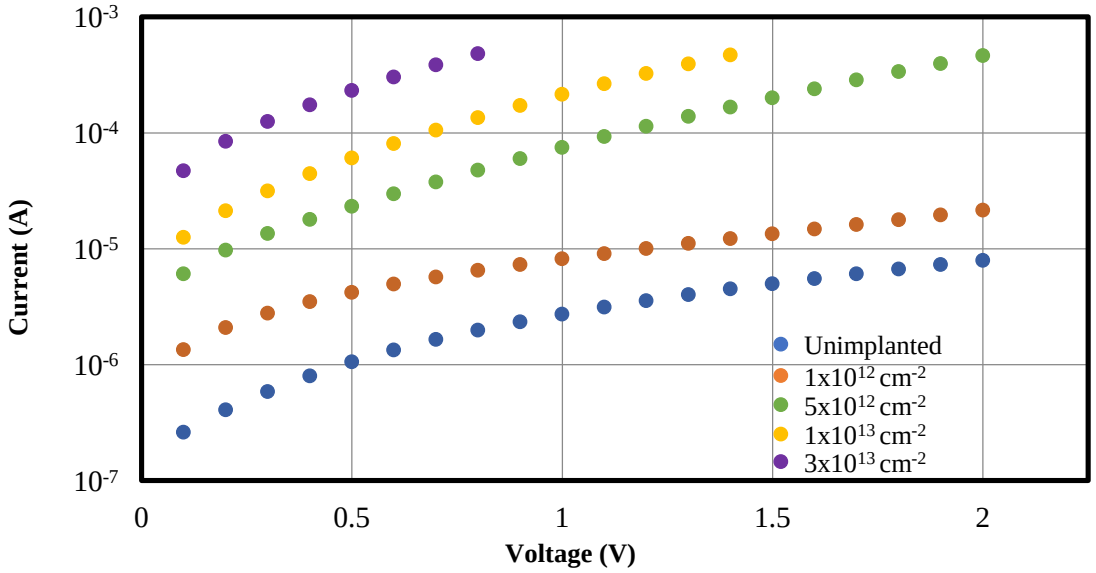

Fig. 4.3 Dark Current for detectors in Reverse Bias.

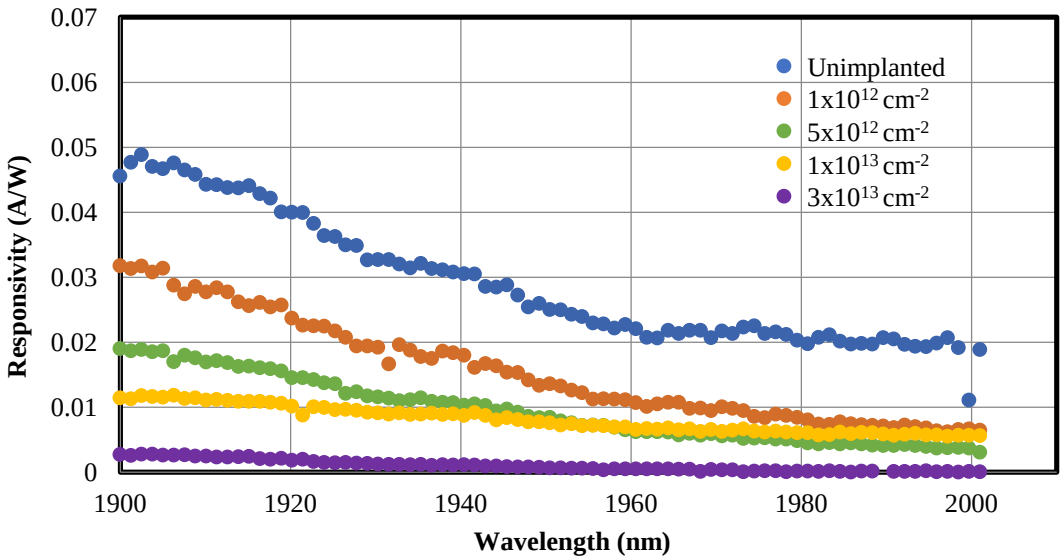

Fig. 4.4 Responsivity of detectors at 0 V bias.

However, as is shown in Fig. 4.4, with no bias applied, responsivity decreases with increasing implantation dose. The decrease in responsivity is attributed to an increase in concentration of recombination centers caused by ion implantation and defect formation, and a subsequent increase in recombination rate for any optically generated carriers. Such an increase is greater than any increase in optical absorption due to the introduction of deep-levels. Furthermore, even with a bias applied as shown in Fig. 4.5 and 4.6 where a reverse bias of 1 and 2 V is applied respectively, the responsivity of the implanted detectors is still less than that of an unimplanted device. It is reasonable to anticipate that the extraction rate of charge carriers should increase considerably with applied bias, and thus defect mediated detection does not seem to be a promising route to extended wavelength detection in germanium-based devices.

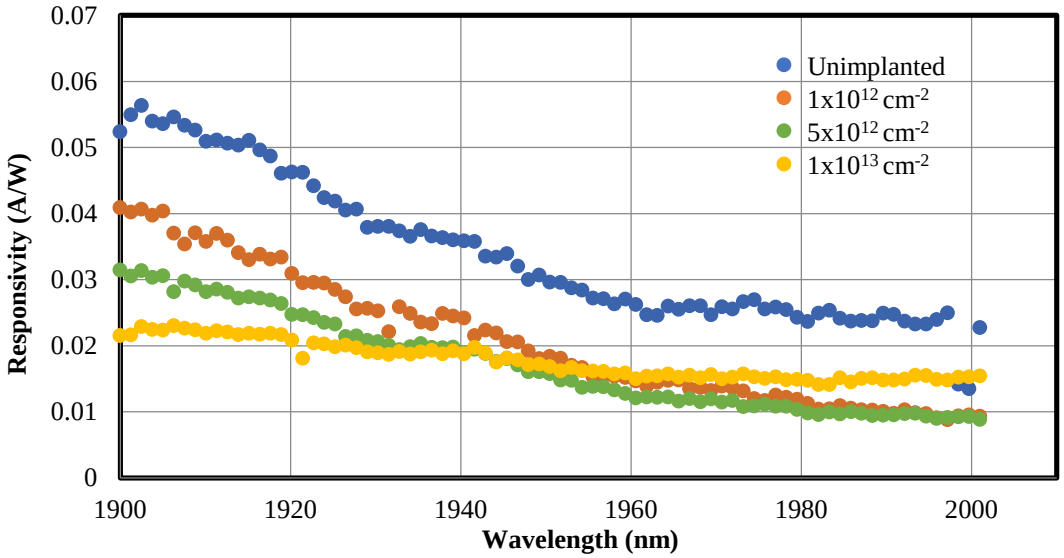

Fig. 4.5 Responsivity of detectors at 1 V reverse bias

It is thus concluded from these results that the absorption via the indirect bandgap transition, and subsequent charge separation, is the dominant mechanism in generating photocurrent. There is some suggestion due to the shape of the responsivity curve that

defect mediated generation of charge carriers may play a small role in enhancing photocarrier generation (especially at higher wavelengths), although rapid recombination of carriers strongly suppresses photocurrent generation beyond that seen for the unimplanted device. This is illustrated in Fig. 4.5 as the detector implanted with a dose of

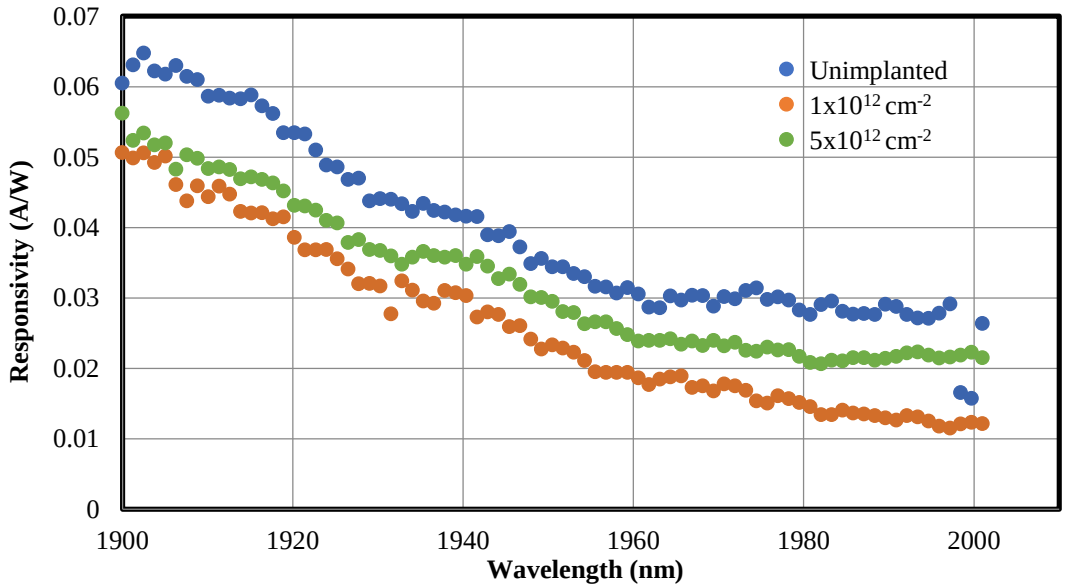

Fig. 4.6 Responsivity of detectors at 2 V reverse bias

$1x10^{13}$ cm^{-3} has a much flatter response across the investigated range and a better responsivity for wavelengths greater than 1950 nm when compared with samples with a lower implant dose at 1 V reverse bias. Furthermore, as shown in Fig. 4.6 at 2 V reverse bias the responsivity of the device implanted with a dose of $5x10^{12}$ is higher than that of the device implanted with a dose of $1x10^{12}$ across the entire range of wavelengths which shows that absorption has increased with dose in this case.

While these results indicate that it may be possible to improve the responsivity beyond that of an unimplanted device by applying larger biases, the increase in dark current makes this unfeasible for commercial applications due to the large power

consumption as well as the poor SNR. As a result, defect mediated detection in Ge appears to be an ineffective method for detection in the TDFA band (at least for the experimental conditions used here), although the response of the unimplanted device is surprisingly strong. Therefore, more study of Ge-on-Si detectors at higher wavelengths was performed using unimplanted devices and is detailed in the following section.

4.1.5 Electro-optical response of unimplanted devices

To allow comparison with the large body of work reporting evanescent Ge/Si waveguide detectors, the steady-state (*DC*) *I-V* characteristic of the device with detector length (L_{DET} in Fig.4.2) = 50 μm, and length of the passive Ge waveguide preceding the detector (L_{Ge} in Fig. 4.2) = 0 μm was measured first, with no coupled light and with light at a wavelength of 1550 nm and input power of 1.5 mW. The optical power interacting the Ge detector is estimated to be ~0.65 mW. The data is shown in Fig. 4.7. For a reverse

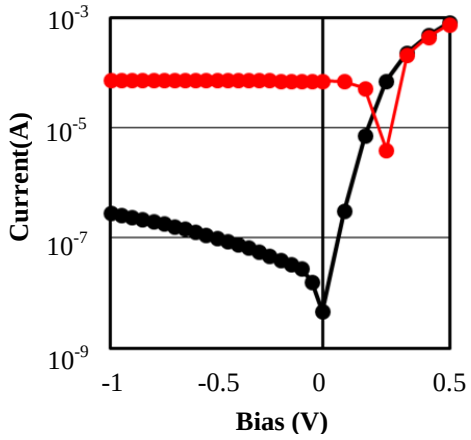

Fig. 4.7 I-V characteristic of detector with L_{DET} = 50 μm and L_{Ge} = 0 μm. Black circles: dark current. Red circles: under input of 1550nm with optical power at the detector structure estimated to be 0.65 mW.

bias of 1 V an internal responsivity of 0.74A/W is observed, with an associated dark current <1 μA which is comparable with previous work using a similar detector design [8].

An identical device was subjected to a high-speed modulation at 1550 nm using a PRBS31 electrical signal from an Anritsu MP1800A SQA driving an Anritsu MP9681A E/O converter with eye diagrams obtained using an Agilent Infiniium DCA-J 86100C with an 86116C module for electrical measurement of the device probe signal. Eye diagrams for data-rates of 5 and 12.5 Gb/s are shown in Fig. 4.8. Despite the relatively long L_{DET} for this device, open eyes are clearly observed. Based on similar device designs reported in [8], the 3 dB bandwidth for this 50 μm detector is estimated to be ~10 GHz.

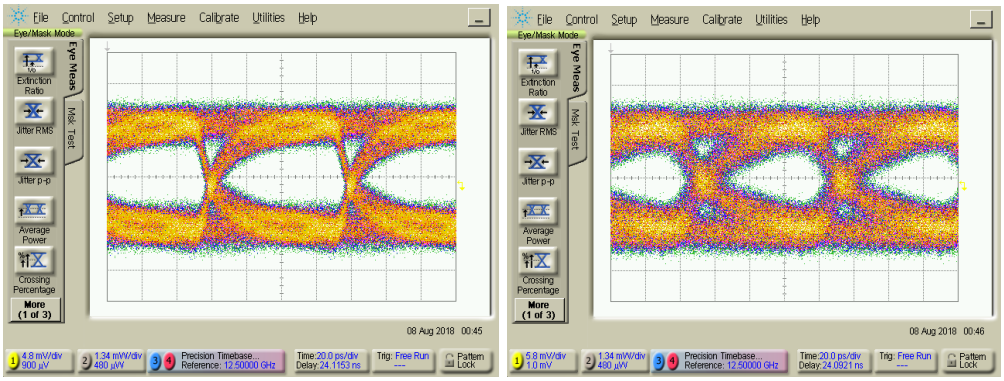

Fig. 4.8 Eye diagrams obtained for 5 Gb/s and 12.5 Gb/s for the device with L_{DET} = 50 μm and L_{Ge} = 0 μm. Optical signal was at a wavelength of 1550 nm with optical power at the detector structure estimated to be 0.65 mW.

The responsivity of the same detector was determined, for reverse bias of 1V, as a function of wavelength for the two ranges 1550 nm -1640 nm and 1850 nm -2000 nm. The calculated responsivity, assuming coupling losses of 3.1 dB and 5.1 dB respectively for the two wavelength ranges accounts for the variation in laser output power across each range.

The resulting data is plotted in Fig. 4.9. For the shorter wavelength range the roll-off behavior is consistent with that previously observed [3], with an internal responsivity of 0.74 A/W at 1550 nm which decreases with increasing wavelength until at 1640 nm it is 0.11 A/W. In the longer wavelength range the detector has a responsivity that falls from 0.02 A/W to 0.005 A/W with increasing wavelength. The exponential decay in responsivity with increasing wavelength is consistent with indirect band to band transitions [11].

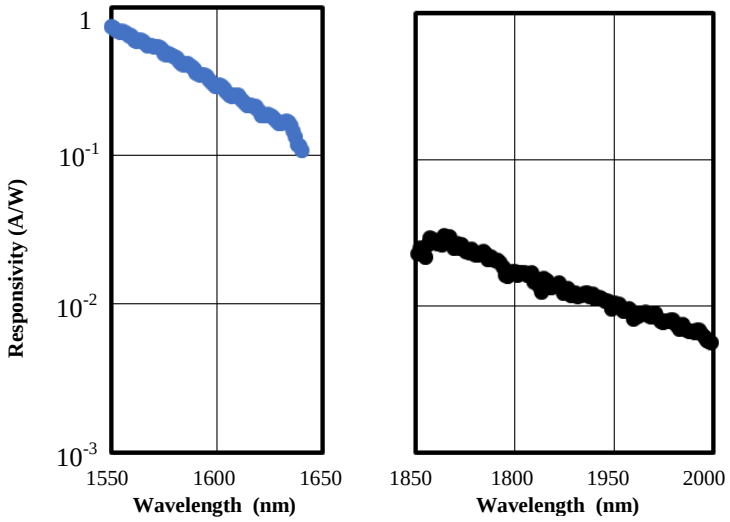

Fig. 4.9 Detector responsivity versus wavelength for L_{DET} = 50µm and L_{Ge} = 0 µm.

To ascertain the significance of the indirect bandgap on optical absorption, measurements of photocurrent for a range of devices with varying values of L_{DET} and L_{Ge} were made. In the case of extended wavelength measurements, this provides for an estimation of optical loss in the Ge/Si waveguide without the need for an independent determination of parasitic loss due to Ge doping and metallization, as is the case for L_{DET}.

Specifically, the photocurrent for devices with L_{Ge}=0 μm, measured as a function of detector length L_{DET} can be approximated by:

$$i_{pc} = A\,[1-exp\,(-L_{DET}\,\alpha_{sum})] \quad (4.1),$$

where i_{pc} is the measured photocurrent, α_{sum} is the absorption length and A is the saturation photocurrent. In this case, α_{sum} results from a combination of loss mechanisms [12], which include: intrinsic optical absorption in the Ge/Si waveguide; absorption via the free carriers that result from doping in both the Ge and the Si; and absorption via the metallic contact on the surface of the L_{DET} region. Finite element simulation, using the commercial Synopsis software package RSoft FEMSIM, of the structure shown in Fig. 4.2 as L_{DET}, and reference to previous work on optical absorption in bulk Ge [13], suggests that the dominant loss mechanism for wavelengths in excess of 1700 nm is via free carrier absorption. Thus, for these extended wavelengths, using devices consisting of L_{DET} only to determine the optical absorption within the Ge/Si waveguide proves challenging. Whereas, in the case where L_{DET} is fixed and L_{Ge} is varied, the photocurrent is approximated by:

$$i_{pc} = B\,[exp\,(-L_{Ge}\,\alpha_{GeSi})] \quad (4.2),$$

where i_{pc} is the measured photocurrent, α_{GeSi} is the absorption length in the Ge/Si waveguide and B is the photocurrent for $L_{Ge} = 0$.

Fig. 4.10 shows photocurrent measurements as well as the fits derived from eqns. (4.1) and (4.2) for a wavelength of 1900nm and input power at the chip of 1 mW. The fits yield α_{sum} = 0.03 μm^{-1}; and α_{GeSi} = 0.003 μm^{-1}, confirming intrinsic absorption is not the dominant loss mechanism at 1900 nm. It should be noted that determination of α_{GeSi} could

be achieved also via the use of passive Ge/Si waveguide structures and external photocurrent detection. However, this experiment is performed for Ge/Si formed during the fabrication of functioning detectors and thus the results demonstrate faithful representation of the Ge/Si absorption. Further, using the same samples, detection at extended wavelengths is demonstrated.

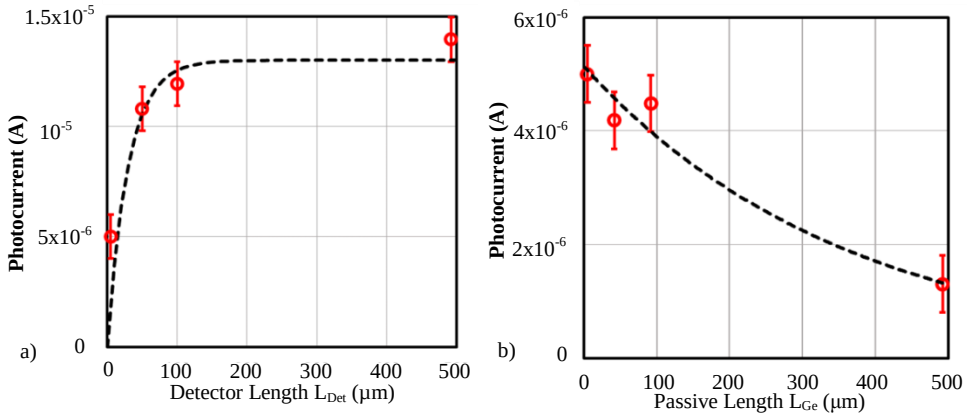

Fig. 4.10 a) Photocurrent for devices with L_{Ge} = 0 and varying L_{DET}; b) photocurrent for devices with L_{DET} = 5µm and varying L_{Ge}. For all measurements the input wavelength and power at the input coupler was 1900 nm and 1 mW respectively. The error bars are calculated from measurement of multiple devices and are a consequence of variation in coupling efficiency.

The value of α_{GeSi} = 0.003 µm^{-1} is in excess of that expected for bulk Ge via an indirect bandgap transition of 0.65 eV (1900 nm), which is reported to be ~0.0001 µm^{-1} [13]. Rather, the measured value indicates a band-gap narrowing (consistent with an equivalent indirect transition) of ~0.05 eV. Together with the form and extent of the roll-off data shown in Fig. 4.9, it is postulated that this enhanced absorption is the result of strain induced narrowing of the indirect bandgap; a similar conclusion as was described for direct transitions in [3]. A bandgap narrowing of this degree is consistent with a strain less than 1%, as indicated by theoretical calculation [14].

The enhancement of responsivity of integrated Ge detectors has been well-described previously for operation in the *L*-band [for example see Ref. [3]]. The raised temperature epitaxial growth, together with the different thermal expansion coefficients for Ge and Si, results in the introduction of tensile strain in the Ge when the sample is cooled at the completion of the growth cycle. The effective reduction in the direct optical bandgap has been reported to be on the order of 0.1 eV.

4.2 Summary and Conclusion

In this chapter the use of evanescently coupled Ge waveguide detectors in the wavelength range of 1850-2000 nm is examined. The devices described were fabricated in a commercial Si photonics foundry using a process flow designed for detection in the *O*, *C* and *L* bands with some detectors being implanted post fabrication in order to introduce defects to examine the role of defect mediated detection in Ge. For samples that have been implanted with ions it is shown that while defects may play a small role in the detection especially at higher wavelengths the introduction of defects degrades the responsivity of the devices at low applied biases. It is possible that higher bias can be applied to improve responsivity, however, this will reduce the SNR and increase the power consumption due to high dark current. While the responsivity of unimplanted detectors with a length of 50 μm at 1850 and 2000 nm is modest for the devices described here (0.02 and 0.005 A/W respectively), it has been shown that this is an enhancement of absorption as compared with that of bulk Ge and could be increased significantly by reducing the parasitic absorption, which dominates for the current design. Specifically, by

removing the doped contact from the Ge waveguide, the intrinsic absorption of the indirect bandgap is likely to dominate. Such a detector design is described in [15]. Due to the decreased responsivity of implanted detectors it is theorized that the enhancement of absorption of these Ge detectors as compared with bulk Ge is due to bandgap shrinkage caused by tensile strain in Ge, which will be explored further in the following chapter. This strain could be further enhanced either through geometrical design or the addition of a dielectric stressor [16]. The use of Ge in a separate absorption, charge and multiplication (SACM) avalanche detector would also provide for order of magnitude improvements in the responsivity, with high electrical bandwidth compared with the linear devices reported here [17]. Certainly, the use of Ge detectors is a feasible route to integrated detection in Si PIC design for use in the extended wavelength range, which overlaps with the TDFA gain band.

References

[1] R. Sheehan, E. Russell, N. Kavanagh, J. O'Callaghan, B. Corbett, and F. C. Garcia Gunning, "Key enabling technologies for optical communications at 2000 nm," *Appl. Opt.*, vol. 57, no. 22, pp. E64–E70, 2018.

[2] Y. Jung, P. C. Shardlow, M. Belal, Z. Li, A. M. Heidt, J. M. O. Daniel, D. Jain, J. K. Sahu, W. A. Clarkson, B. Corbett, J. O'Callaghan, S. U. Alam, and D. J. Richardson, "First demonstration of a 2μm Few-mode TDFA for mode division multiplexing," *Opt. Express*, vol. 22, no. 9, pp. 10544–10549, 2014.

[3] Y. Ishikawa, K. Wada, D. D. Cannon, J. Liu, H. C. Luan, and L. C. Kimerling, "Strain-induced band gap shrinkage in Ge grown on Si substrate," *Appl. Phys. Lett.*, vol.

82, no. 13, pp. 2044–2046, 2003.

[4] Y. Dong, W. Wang, S. Xu, D. Lei, X. Gong, X. Guo, H. Wang, S.-Y. Lee, W.-K. Loke, S.-F. Yoon, and Y.-C. Yeo, "Two-micron-wavelength germanium-tin photodiodes with low dark current and gigahertz bandwidth," *Opt. Express*, vol. 25, no. 14, pp. 15818–15827, 2017.

[5] J. J. Ackert, "High-speed silicon detector structures for photonic integrated circuits," McMaster University, 2015.

[6] M. Casalino, G. Coppola, R. M. De La Rue, and D. F. Logan, "State-of-the-art all-silicon sub-bandgap photodetectors at telecom and datacom wavelengths," *Laser Photonics Rev.*, vol. 10, no. 6, pp. 895–921, 2016.

[7] J. J. Ackert, D. J. Thomson, L. Shen, A. C. Peacock, P. E. Jessop, G. T. Reed, G. Z. Mashanovich, and A. P. Knights, "High-speed detection at two micrometres with monolithic silicon photodiodes," *Nat. Photonics*, vol. 9, no. 6, pp. 393–396, 2015.

[8] K.-W. Ang, T.-Y. Liow, M.-B. Yu, Q. Fang, J. Song, G.-Q. Lo, and D.-L. Kwong, "Low Thermal Budget Monolithic Integration of," *IEEE J. Quantum Electron.*, vol. 16, no. 1, pp. 106–113, 2010.

[9] J. F. Ziegler, M. D. Ziegler, and J. P. Biersack, "SRIM - The stopping and range of ions in matter (2010)," *Nucl. Instruments Methods Phys. Res. Sect. B Beam Interact. with Mater. Atoms*, vol. 268, no. 11–12, pp. 1818–1823, 2010.

[10] J. K. Doylend, P. E. Jessop, and A. P. Knights, "Silicon photonic resonator-enhanced defect-mediated photodiode for sub-bandgap detection," *Opt. Express*, vol. 18, no. 14, pp. 14671–14678, 2010.

[11] S. M. Sze and K. K. Ng, *Physics of Semiconductor Devices Third Edition*, Third Edit. Hoboken, New Jersey: John Wiley & Sons, 2006.

[12] H. Liang, D. Feng, R. Shafiiha, Y. Liu, M. Asghari, W. Qian, P. Dong, S. Liao, N.-N. Feng, J. Fong, J. E. Cunningham, Y. Luo, and C.-C. Kung, "36 GHz submicron silicon waveguide germanium photodetector," *Opt. Express*, vol. 19, no. 11, pp. 10967–10972, 2011.

[13] W. C. Dash and R. Newman, "Intrinsic Optical Absorption in single-Crystal Ge and Si," *Phys. Rev.*, vol. 99, no. 4, pp. 1151–1154, 1955.

[14] K. Guilloy, N. Pauc, A. Gassenq, Y. M. Niquet, J. M. Escalante, I. Duchemin, S. Tardif, G. Osvaldo Dias, D. Rouchon, J. Widiez, J. M. Hartmann, R. Geiger, T. Zabel, H. Sigg, J. Faist, A. Chelnokov, V. Reboud, and V. Calvo, "Germanium under High Tensile Stress: Nonlinear Dependence of Direct Band Gap vs Strain," *ACS Photonics*, vol. 3, no. 10, pp. 1907–1911, 2016.

[15] H. T. Chen, P. Verheyen, P. De Heyn, G. Lepage, J. De Coster, P. Absil, G. Roelkens, and J. Van Campenhout, "High-responsivity low-voltage 28-Gb/s Ge p-i-n photodetector with silicon contacts," *J. Light. Technol.*, vol. 33, no. 4, pp. 820–824, 2015.

[16] S. Sauvage, X. Checoury, M. El Kurdi, M. Prost, I. Sagnes, A. Ghrib, R. Ossikovski, G. Beaudoin, P. Boucaud, and G. Picardi, "Direct Band Gap Germanium Microdisks Obtained with Silicon Nitride Stressor Layers," *ACS Photonics*, vol. 3, no. 3, pp. 443–448, 2016.

[17] Y. Kang, H. D. Liu, M. Morse, M. J. Paniccia, M. Zadka, S. Litski, G. Sarid, A. Pauchard, Y. H. Kuo, H. W. Chen, W. S. Zaoui, J. E. Bowers, A. Beling, D. C. McIntosh,

X. Zheng, and J. C. Campbell, “Monolithic germanium/silicon avalanche photodiodes with 340GHz gain-bandwidth product,” *Nat. Photonics*, vol. 3, no. 1, pp. 59–63, 2009.

Chapter 5 – Raman Spectroscopy of Ge and SiGe Thin Films

Overview

This chapter presents the results of Raman spectroscopy on Ge and SiGe films. The first section of the chapter details the analysis of Ge films, beginning with the examination of the Ge detectors described in the previous chapter. This is followed by an examination of Ge nanowire bridges formed from Ge-on-SOI. The second section of the chapter examines the SiGe fabricated via Ge implantation and condensation. The chapter then concludes with a summary. Results from this work have been reported by the author in the following journal publication and conference proceedings:

R. Anthony, D. Hagan, D. Genuth-Okon, J. Mullins, I. F. Crowe, M. P. Halsall, and A. P. Knights, "Extended wavelength responsivity of a germanium photodetector integrated with a silicon waveguide" *IEEE Journal of Lightwave Technology*, 2019 (Submitted)

R. Anthony, A. Gilbank, I. Crowe, A. Knights, "Strain Analysis of SiGe Microbridges" *Proc. of SPIE*, 10537, Silicon Photonics XIII, San Francisco, 2018.

5.1 Raman analysis of Ge Detectors

5.1.1 Sample characterization

Raman spectroscopy was performed on both the exposed Ge (with cladding oxide removed) from two of the Ge detectors described in the previous chapter (spatially

separated but on the same chip, schematically described in Fig. 4.2) and nanowire bridges formed from samples of Ge-on-SOI (similar in design to those described schematically in Fig. 2.14). These measurements were done to confirm the presence, and estimate the magnitude and type of strain (postulated to be the source of the enhanced detection at wavelengths close to 2000 nm), and to investigates methods to further effect a band narrowing through strain engineering. The samples were excited using a 633 nm HeNe laser via 50x objective lens (0.75 N.A.) and the Raman signal was collected in backscattering configuration using a Renishaw *in-via* system equipped with a 1800 g/mm grating. The laser power was kept below 0.1 mW to avoid sample heating and a large number of measurements were taken from the L_{Ge} region; from a bulk (unstrained) Ge wafer; and unstrained bulk Si (the latter measurements used for precision instrument calibration).

5.1.2 Raman determination of strain of Ge detectors

In order to evaluate the presence, and estimate the magnitude and type of any strain in the integrated Ge photodetectors, the dominant Ge-Ge Raman scattering peak obtained from two detector samples was compared with that of a sample of bulk, unstrained Ge. Fig. 5.1 gives a schematic representation of the collection of the Raman spectra. The scattering peaks were fit with a single Lorentzian function to determine the precise peak position. In total, 45 measurements (randomly selected from across the wafer surface) were taken from the bulk unstrained Ge, from which a histogram of peak positions was generated, shown in Fig. 5.2 (purple dataset). A normally distributed fit to the histogram yields an average peak position of 300.84 cm^{-1} with a standard deviation

(σ) of 0.07 cm^{-1}, which is in excellent agreement with the literature value for unstrained Ge [1].

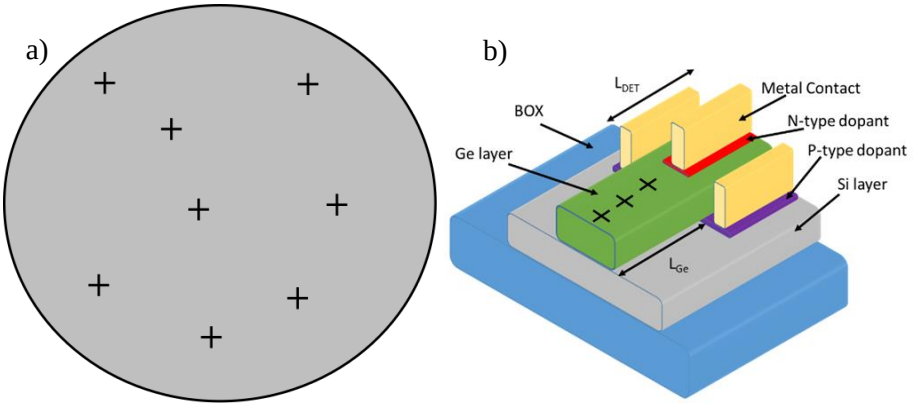

Fig. 5.1 Schematic representation of the collection of Raman spectra from the a) Bulk Ge wafer and b) the passive length of Ge which did not have a cladding oxide. Crosses are meant to indicate the area which were of interest for Raman spectroscopy.

A similar approach was used to determine the average peak position for the Ge/Si waveguides (L_{Ge}). For the first sample (sample 1), a total of 28 measurements, and for the second sample (sample 2) 25 measurements were taken. Similar histograms (and fits) were generated, and are also shown in Fig. 5.2 (blue and orange datasets), yielding average peak positions of 300.22 cm^{-1} (σ = 0.04 cm^{-1}) and 300.37 cm^{-1} (σ = 0.04 cm^{-1}), respectively. These measurements indicate a (statistically significant) peak shift of between -0.47 cm^{-1} and -0.62 cm^{-1} (indicating the presence of tensile strain) in the detector sample(s), relative to the bulk unstrained Ge. It is difficult to determine the strain precisely from these peak shifts because of the variation in the linear strain-shift coefficient, *b* (= Δω/Δε) with the angle that is formed between the long axis of the detector sample(s) and the underlying crystallographic orientation of the material [2]. However, if the strain is assumed to be predominantly uniaxial, then *b* will be in the range; -130 to -175 [2], which indicates a peak (tensile) strain for sample 1 of between

0.35 and 0.48 %; and for sample 2 of between 0.27 and 0.36 %. The strain measured from these detectors is slightly larger than that commonly reported (0.2 to 0.25%) after high temperature annealing of epitaxial Ge on Si [3]. For the largest measured strain this corresponds to a band gap of approximately 0.62 eV. It is well known that the tensile strain in Ge layers grown or deposited on Si develops, after recovery from high temperature thermal treatments, as a result of the mismatch of the thermal expansion coefficients of the two materials. Larger values of tensile strain (0.3 to 0.4%) were previously reported for Ge on Si wires grown by Lateral Liquid Phase Epitaxy as a result of the higher (close to melting) temperatures involved [4].

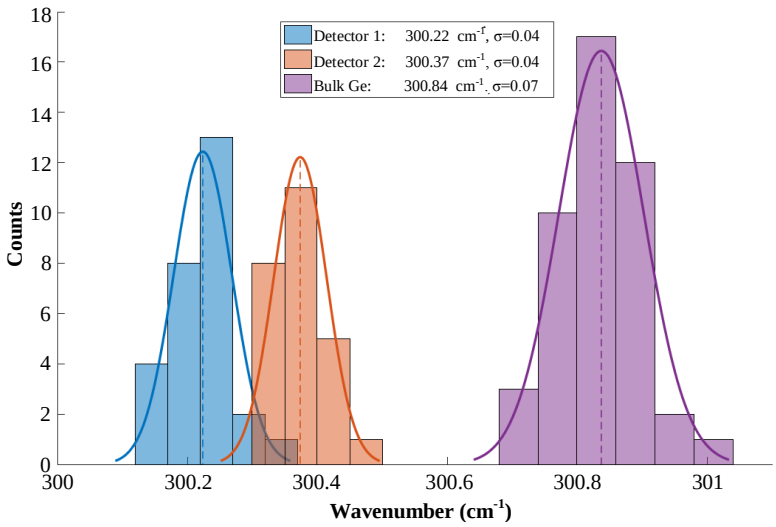

Fig. 5.2 Histograms depicting the peak positions determined for unstrained bulk Ge (purple, n = 45) and samples 1 (blue, n = 28) and 2 (orange, n = 25) along with Gaussian fits used to obtain the average and standard deviation for each.

Although it should be noted that for sample 1, L_{Ge} is 492 µm whilst for sample 2, L_{Ge} is only 92 µm, the small difference in average Raman peak positions between samples 1 and 2 is marginally statistically significant, and thus it is concluded that the detector length has little physical effect on the degree of strain. The larger average Raman

shift for both the detectors, relative to that of the unstrained Ge peak, on the other hand does imply that, despite differences in device geometry and relative position on the chip, the Ge-Si material exhibits a consistent level of relatively large tensile strain. Furthermore, given the uncertainty in the theoretical expectation of the band-gap narrowing with tensile strain and that associated with the determination of the optical loss in the passive section of the waveguide detectors, that these Raman measurements are entirely consistent with the interpretation from the previous chapter that the enhanced responsivity at extended wavelengths in these devices results from the same strain induced band-gap narrowing mechanism as that reported in [5].

5.2 Raman Characterization of Ge Nanowire Bridges

As the above results confirm, the Ge-on-SOI from the detectors in Chapter 4 are strained and the strain enhancement is consistent with the absorption at longer wavelengths. This confirms that further enhancement of the strain in Ge is a viable method for producing a detector in the TDFA band. As is discussed in chapter 2 there are multiple methods of enhancing the strain in Ge. The following sections will examine the use of the nanowire bridge technique, where the oxide beneath the nanowire is etched away allowing for energy transfer into the nanowire, to enhance strain in Ge-on-SOI.

5.2.1 Fabrication and Characterization

To fabricate nanowire bridges, samples of <100> Ge-on-SOI were patterned using a contact lithography system. The samples were then etched to the top of the BOX using an inductively coupled plasma system. The nanowire was then released by etching away

the BOX using a buffered HF solution. Following processing, images were taken using a JEOL JCM-6000Plus NeoScope Benchtop SEM. Fig. 5.3 shows a typical suspended bridge structure with a 2 µm wide and 10 µm long nanowire.

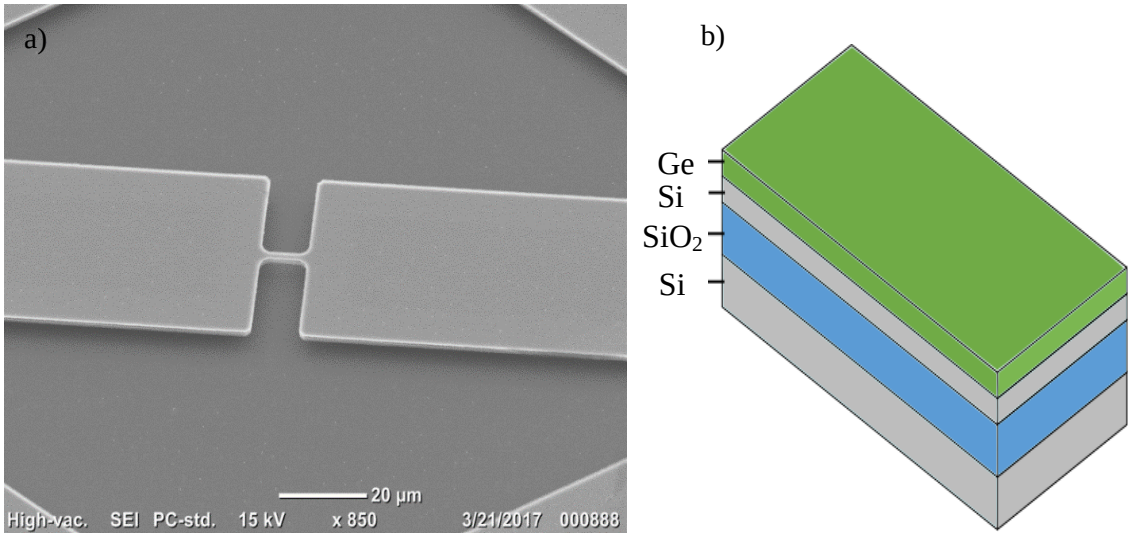

Fig. 5.3 a) SEM of a Ge nanowire Bridge and b) schematic diagram of the layers from samples used in this work.

Raman spectroscopy was performed using the same system detailed in section 5.1. An important characteristic of nanowire bridges is that of the enhancement factor of the strain (*EF)*, which is the ratio of biaxial strain in the as grown material to the uniaxial strain introduced in the nanowire. The *EF* is a function of the relative sizes of the nanowire and pad with *EF* being given by the following:

$$EF = \eta \frac{2L+B}{B}\left[1+\frac{A}{B-A}\right] / \left[\frac{b}{a}+\frac{A}{B-A}\right] \tag{5.1}$$

where A is the length of the nanowire, B the length of the bridge, a is the width of the nanowire, b is the width of the bridge, L is the length of oxide etched from around the bridge and η is given by the following equation:

$$\eta = \frac{t_{Ge} Y_{Ge}}{t_{Ge} Y_{Ge} + t_{Si} Y_{Si}} \tag{5.2}$$

where *t* refers to the thickness of either Si or Ge and *Y* refers to the modulus of either Ge or SiGe for the samples used in this work it 0.8 for the Ge-on-SOI samples.

5.2.2 Determination of Strain for Ge Bridges

Raman spectroscopy maps were created for two bridges, one for a bridge with a 6 μm wide, 8 μm long nanowire as shown in Fig. 5.4 and another for a bridge with a 2 μm wide, 10 μm long nanowire shown in Fig. 5.5. Similar to the Ge detector measurements each Ge-Ge mode from the Raman spectra obtained from the maps was then fit with a Lorentzian to determine peak position. As with the Ge detectors it is difficult to determine the precise strain of the bridges as there is variation between the axis of the bridge and crystallographic orientation of the Ge. Similar to the Ge detectors it can be assumed that the strain in the pad is predominantly uniaxial, while calculating the enhancement factor eliminates some of the variability as both the nanowire and pad will both be oriented in the same direction.

For both bridges it can clearly be seen that there is an enhancement in the strain across the nanowire with an *EF* of approximately 5.5 for the 6 μm wide 8 μm long nanowire and an *EF* of 13.5 for the 2 μm wide 10 μm long nanowire when calculating using the point of max strain, which is a relatively large deviation from the *EF* calculated from Eqn. 5.1 which are 11 and 20.8 respectively. The difference in the calculated and experimental values is attributed to the variation in patterning caused by diffraction effects that are associated with contact lithography. Using the raman spectra measured

from the center of the 2 µm wide 10 µm long bridge and assuming the largest value of *b* the strain in the bridge is calculated to be 1.7% which corresponds to a indirect bandgap of approximately 0.58 eV[6].

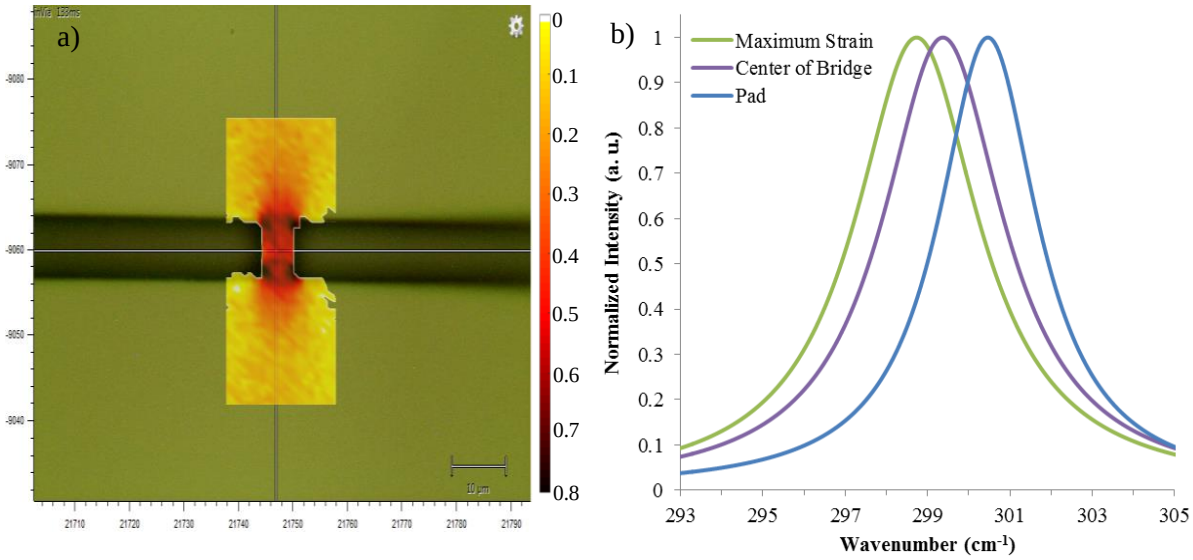

Fig. 5.4 a) Optical micropscope image with strain map overlayed on a bridge with a 6 µm wide 8 µm long nanowire and b) Raman Spectra from the bridge and nanowire

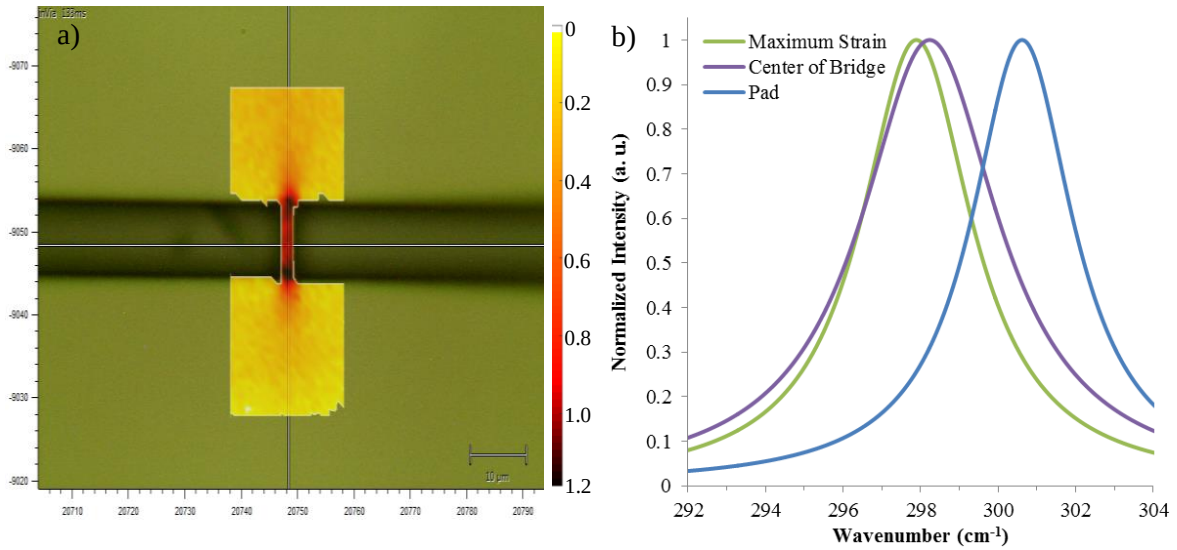

Fig. 5.5 a) Optical micropscope image with strain map overlayed on a bridge with a 2 µm wide 10 µm long nanowire and b) Raman spectra from the bridge and nanowire

5.3 Raman analysis of SiGe

As demonstrated in chapter 3 the implantation and condensation method can be used in a detector however, the responsivity is relatively low. Therefore similar to the nanowire bridges created using Ge it is of great interest to see if the same technique can be incorporated to increase tensile strain

5.3.1 Fabrication

Samples of single crystal 250 nm SOI with a 2000 nm BOX were implanted with 33 keV Ge^{+} ions to a fluence of $1x10^{17}$ cm^{-2}. Following implantation a thermal oxidation was performed in a tubed furnace in a wet O_2 ambient at 1000 °C for 4 minutes. The thermal oxide was removed via etching using a buffered HF solution before microbridge patterning was performed using contact lithography. Subsequent SiGe and Si etching was performed using an inductively coupled plasma reactor. The microbridges were then released by etching the BOX in a buffered HF solution. Following processing, images

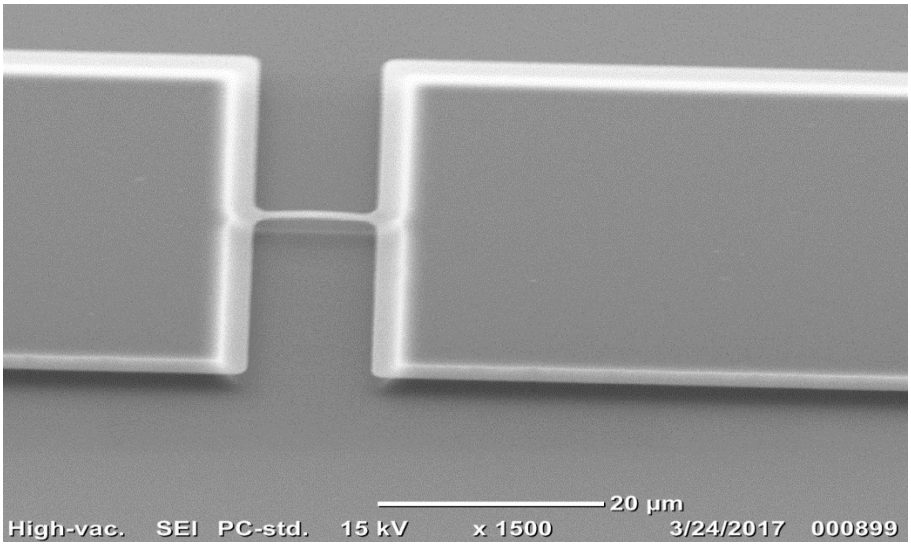

Fig. 5.6 SEM Image of a bridge device with a 1 µm thick nanowire.

were taken using a JEOL JCM-6000Plus NeoScope Benchtop SEM. Fig. 5.6 shows a typical bridge structure with a 1 μm wide nanowire. The lighter areas under the bridge and pad indicate BOX removal confirming that the nanowire has been completely released.

5.3.2 Raman strain analysis

The SiGe was optically excited using a 325nm line of a He:Cd laser and the scattered light was collected, confocally using a Thorlabs LMU-40x NUV objective lens with a numerical aperture, NA = 0.5, dispersed using a Horiba LabRAM HR Evolution spectrometer and detected with a thermoelectrically cooled CCD camera. The collected Raman spectra were fitted using a multi-peak Fano function of the form [7]:

$$I(\omega) = \sum_i \frac{(q_i + [(\omega - \omega_{0i}) / \Gamma_i])^2}{1 + [(\omega - \omega_{0i}) / \Gamma_i]^2} I_{0i} \ , \qquad (5.3)$$

where the peak position and width are determined from ω_0 and Γ respectively and the direction and degree of asymmetry is determined by the sign and magnitude of the Fano parameter, q. Each sample exhibited peaks associated with Si-Si (~500 cm^{-1}), SiGe (~400 cm^{-1}), and Ge-Ge (~300 cm^{-1}) scattering from the SiGe as well as a Si-Si peak from pure SOI (~520 cm^{-1}). Analysis of the SOI peak from unpatterned samples shows that the samples have a tensile strain of 0.22%, however, for patterned samples this peak has been removed for clarity. Fig. 5.7a and 5.7b are examples of spectra from the pad of a bridge of bond types which is either x^2 for Ge or $(1-x)^2$ for Si. Therefore it can be assumed that the Raman scattering intensity is proportional to the number of vibrating pairs and that the ratio of scattering intensities as a function of Ge composition is thus [8]:

$$\frac{I_{Ge-Ge}}{I_{Si-Si}}(x) = \frac{x^2}{(1-x)^2}\ , \tag{5.4}$$

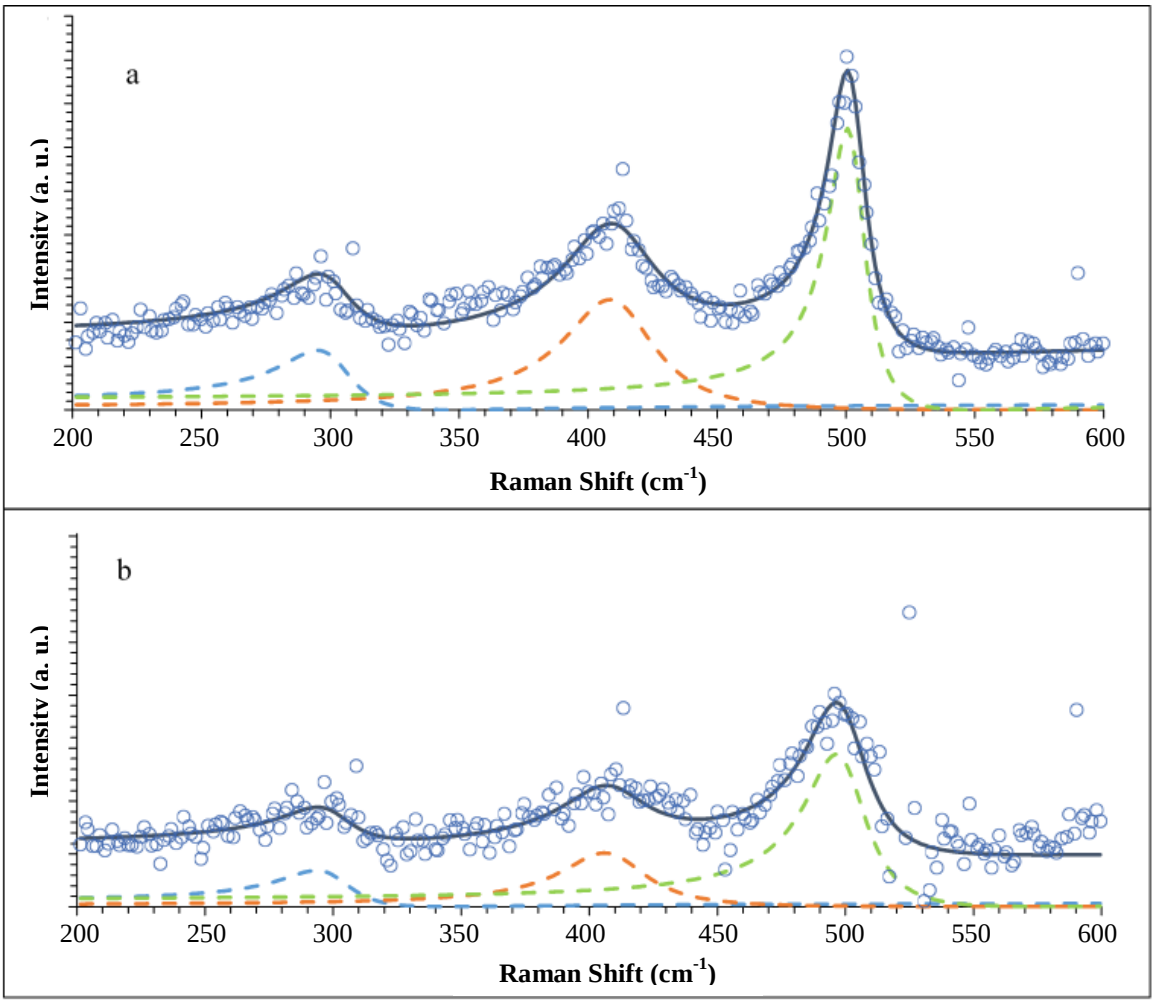

Fig. 5.7 Scattering spectra from the SiGe layer, with background peaks removed, of a) a microbridge pad and b) a 3 μm nanowire fitted with asymmetric fano functions for the Si-Si, Ge-Ge and SiGe scattering peaks. Integrated peak intensities and frequencies were determined from these fitted peaks.

Using the integrated intensities from the fitted peaks the composition of the SiGe layer was found to vary from x=0.38 -0.40. Using the composition, the strain was then determined using the following empirical relations[9–11]:

$$\omega(x,\varepsilon)_{Si-Si} = 520.5 - 70x + b_{Si}\varepsilon\ , \tag{5.5}$$

$$\omega(x,\varepsilon)_{Si-Ge} = 400.1 + 24.5x - x^2 - 33.5x^3 + b_{SiGe}\varepsilon \ , \tag{5.6}$$

$$\omega(x,\varepsilon)_{Ge-Ge} = 282.5 + 19x + b_{Ge}\varepsilon \ , \tag{5.7}$$

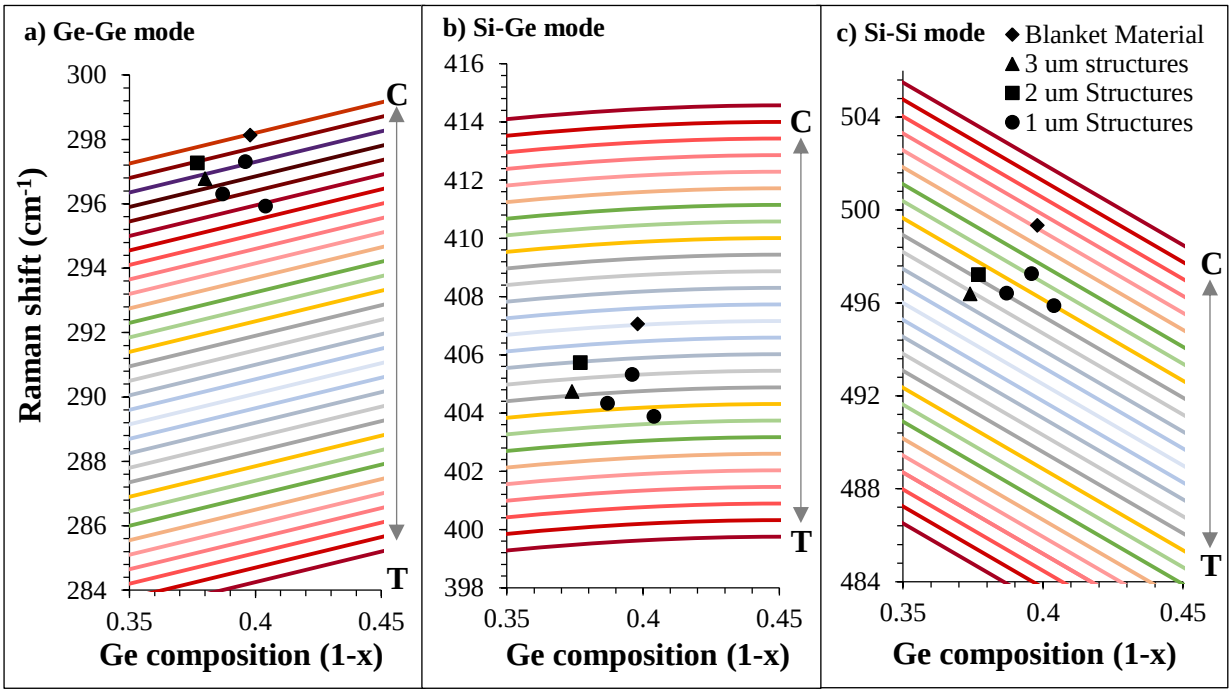

Fig. 5.8 Predicted Raman shift for a) Ge-Ge, b) Si-Ge and c) Si-Si alloy modes as a function of Ge composition, (1-*x*) for various values of strain, either tensile (T) or compressive (C) in the range of 1.3% tensile strain to 1.3% compressive strain in 0.1% increments for the Si-Ge and Si-Si modes and 1.3% tensile strain to 1.8% compressive strain in 0.1% increments for the Ge-Ge mode.

where the coefficient b_m are parameters that depend on the elastic constants of Si, SiGe and Ge. The parameters used for these calculations are from Ref [10]. Fig. 5.8 shows the graphical representation of eqs (5.5) – (5.7). As can be seen in the figure, while there is only a small change in composition of the SiGe, which varies by 2%, there is a quite a large decrease in strain in the nanowire bridge structures. For example, in the Si-Si mode there is a strain reduction from 0.9% compressive strain on the pad to 0.3% compressive strain for a nanowire. It can also be seen that while the strain of each mode varies between Si-Si, SiGe and Ge-Ge the relative strain for each structure remains the same.

This relaxation indicates that the strain in these layers can be controlled via appropriate design of the bridge structure.

5.4 Summary and conclusion

In this chapter Raman spectroscopy has been used to examine the strain of Ge-on-SOI in both detectors and nanowire bridges and SiGe. Examination of the Ge-on-SOI detectors from the previous chapter has confirmed that there is tensile strain in Ge grown on Si with the amount of strain in the detectors being consistent with enhanced optical absorption at extended wavelengths. In addition, it has been shown that by fabricating nanowire bridges and then releasing the nanowires via etching, the strain in the nanowire can be enhanced. This technique has been demonstrated for Ge-on-SOI and SiGe-on-SOI formed via implantation and condensation. This enhancement in strain is of great interest for the development of a Ge detector at extended wavelengths specifically those of the TDFA band.

References

[1] A. V. Baranov, A. V. Fedorov, T. S. Perova, R. A. Moore, V. Yam, D. Bouchier, V. Le Thanh, and K. Berwick, "Analysis of strain and intermixing in single-layer Ge Si quantum dots using polarized Raman spectroscopy," *Phys. Rev. B - Condens. Matter Mater. Phys.*, vol. 73, no. 7, pp. 1–6, 2006.

[2] T. Etzelstorfer, A. Wyss, M. J. Süess, F. F. Schlich, R. Geiger, J. Frigerio, and J. Stangl, "Determining the directional strain shift coefficients for tensile Ge: A combined x-ray diffraction and Raman spectroscopy study," *Meas. Sci. Technol.*, vol. 28, no. 2, 2017.

[3] J. Liu, J. Michel, W. Giziewicz, D. Pan, K. Wada, D. D. Cannon, S. Jongthammanurak, D. T. Danielson, L. C. Kimerling, J. Chen, F. Ö. Ilday, F. X. Kärtner, and J. Yasaitis, "High-performance, tensile-strained Ge p-i-n photodetectors on a Si platform," *Appl. Phys. Lett.*, vol. 87, no. 10, pp. 75–78, 2005.

[4] T. Shimura, Y. Suzuki, M. Matsue, K. Kajimura, K. Tominaga, T. Amamoto, T. Hosoi, and H. Watanabe, "Fabrication of High-quality Ge-on-insulator Structures by Later Liquid Phase Epitaxy," *ECS Trans.*, vol. 69, no. 5, pp. 305–311, 2015.

[5] Y. Ishikawa, K. Wada, D. D. Cannon, J. Liu, H. C. Luan, and L. C. Kimerling, "Strain-induced band gap shrinkage in Ge grown on Si substrate," *Appl. Phys. Lett.*, vol. 82, no. 13, pp. 2044–2046, 2003.

[6] J. Petykiewicz, D. Nam, D. S. Sukhdeo, S. Gupta, S. Buckley, A. Y. Piggott, J. Vučković, and K. C. Saraswat, "Direct Bandgap Light Emission from Strained Germanium Nanowires Coupled with High-Q Nanophotonic Cavities," *Nano Lett.*, vol. 16, no. 4, pp. 2168–2173, 2016.

[7] Naoki Fukata, Keisuke Sato, Masanori Mitome, Yoshio Bando, Takashi Sekiguchi, Melanie Kirkham, J. Hong, Z. L. Wang, and R. L. Snyder, "Doping and Raman characterization of boron and phosphorous atoms in Ge nanowires ," *ACS Nano*, vol. 4, no. 7, pp. 3807–3816, 2010.

[8] F. Pezzoli, L. Martinelli, E. Grilli, M. Guzzi, S. Sanguinetti, M. Bollani, H. D. Chrastina, G. Isella, H. Von Känel, E. Wintersberger, J. Stangl, and G. Bauer, "Raman spectroscopy of Si1-xGex epilayers," *Mater. Sci. Eng. B Solid-State Mater. Adv. Technol.*, vol. 124–125, no. SUPPL., pp. 127–131, 2005.

[9] F. Pezzoli, E. Grilli, M. Guzzi, S. Sanguinetti, D. Chrastina, G. Isella, E. Wintersberger, J. Stangl, and G. Bauer, “Strain-induced shift of phonon modes in Si 1 À x Ge x alloys,” vol. 9, pp. 541–545, 2006.

[10] F. Pezzoli, E. Bonera, E. Grilli, M. Guzzi, S. Sanguinetti, D. Chrastina, G. Isella, H. Von Känel, E. Wintersberger, J. Stangl, and G. Bauer, “Phonon strain shift coefficients in Si1-x Gex alloys,” *J. Appl. Phys.*, vol. 103, no. 9, 2008.

[11] G. Capellini, M. De Seta, Y. Busby, M. Pea, F. Evangelisti, G. Nicotra, C. Spinella, M. Nardone, and C. Ferrari, “Strain relaxation in high Ge content SiGe layers deposited on Si,” *J. Appl. Phys.*, vol. 107, no. 6, 2010.

Chapter– 6 Summary and Future Work

6.1 Summary

This thesis has focused on the use of both SiGe and Ge in silicon photonics with an emphasis on using these mediums for detection. It has established the compatibility of SiGe with CMOS processing and it's use as a detection medium and has shown that Ge, specifically tensile strained Ge, is a suitable material for extended wavelength detection.

In Chapter 2 a brief summary of the theoretical operation of a detector was presented, followed by a literature review of the growth of Ge-on-Si and the use of Ge-on-Si as a platform for detection.

In chapter 3 the formation of SiGeOI layers via high fluence implantation and condensation was detailed. Samples were implanted with Ge^{+} ions to a fluence of $5x10^{16}$ cm^{2} and oxidized in a steam ambient at 900 °C, 1000 °C and 1100 °C for incremental lengths of time in order to examine the formation of the layer over time. Samples were characterized using RBS to confirm thickness and composition of the layers; and spectroscopic ellipsometry to confirm oxide thickness. This data was then used to create a semi-empirical model to simulate the growth of the SiGe films, using a modified segregation boundary condition, an enhanced linear oxidation constant to model the replacement reaction of Ge in oxide with Si as well as the decreased bond strength between Si and Ge as compared with Si and Si, and an enhanced diffusion coefficient which is consistent with transient enhanced diffusion seen in implantation and annealing processes. In addition, TEM and STEM were used to confirm the films were uniform and relatively defect free, while EDS was performed to confirm the profiles obtained from RBS. Finally, Raman spectroscopy was used to characterize the SiGe thin film, finding the

SiGe to be compressively strained with increasing amounts of Ge associated with higher compressive strain. This process was then used to form optical detectors. Partially fabricated structures from IME A-Star were implanted to a fluence of $2.7x10^{16}$ cm^{2} and were oxidized at 900 °C for 5, 15 and 30 minutes respectively. Optical loss measurements of the samples were taken at 1310 nm and compared with unimplanted samples which had been oxidized for similar times to confirm the source of the loss was absorption by Ge. Detectors were then fabricated from the 15 and 30 minute oxidation samples and electrical measurements were taken with the device oxidized at 15 minutes found to have the highest generated photocurrent. This was attributed to an increased Ge concentration, increased detector length and reduced parasitic loss from waveguide size reduction.

In chapter 4 optical detectors formed via the IME Ge growth process were implanted with B^{+} ions to introduce defects into the lattice to examine if Ge is a suitable platform for defect mediated detection. Both unimplanted and implanted samples with detector lengths of 500 µm were characterized using wavelengths from 1850 to 2010 nm. Originally it was thought that unimplanted detectors would have little to no response at these wavelengths, however, when compared to the implanted samples it was found that the unimplanted sample had a higher responsivity. In addition to this the implanted samples had high dark currents which would make them unsuitable for use in a photonic circuit. As a result of this finding, the unimplanted detectors were further characterized from 1600-1640 nm as well as from 1850 – 2010 nm to examine the roll-off of the responsivity. Detectors with lengths of passive Ge were examined to determine the optical absorption length of Ge at these extended wavelengths. Based on both the characterization of the responsivity and the absorption length, the response was theorized to be

due to the indirect transition of Ge with the enhancement at higher wavelengths caused by tensile strain introduced during the growth process of Ge on Si.

In chapter 5 the Raman spectra of the Ge p-i-n detector from chapter 4 was examined and compared with a bulk Ge sample. Doing so it was found that the grown Ge was under tensile strain and the enhanced absorption at higher wavelengths of Ge examined in the previous chapter was consistent with the experimentally determined strain. As a result, Ge nanowire bridges were fabricated and examined with Raman spectroscopy to determine if the grown-in strain could be further enhanced in order to shrink the band gap of Ge to improve the response of a detector at higher wavelengths. Using this technique strain enhancements of up to 13.5 were demonstrated. This technique was also successfully demonstrated to reduce the compressive strain found in SiGe-on-SOI formed via implantation and condensation, which could be of interest for both a detector and for CMOS electronics, specifically for mobility engineering.

6.2 Suggested future work

6.2.1 SiGeOI formed via implantation and condensation

While the formation of the SiGeOI is well documented in chapter 3 there are several experimental and theoretical aspects which should be further explored in future work. For future experimental work there are several aspects which must be explored more fully in order to understand the implantation and condensation process. These include: using higher energy implants and optimized initial capping oxides to increase SiGe layer thickness by reducing Ge evaporation and incorporation into the oxide; the examination of the Ge in the oxide to confirm whether or not a mixed oxide was formed or if Ge was incorporated into the oxide; the agglomeration of Ge which can cause non-uniformity in the films due to the melting of Ge at high temperature; the concentration and effects of implants induced defects which should be

explored more comprehensively using TEM; the determination of surface roughness using AFM; and finally a broader and more comprehensive examination of the strain evolution during the growth process. Doing so will allow for improvements in modelling of the data as well as allowing for comparison between implanted and epitaxially grown SiGe samples. In addition to the experimental aspects, there is still a need for the development of a model which would take into account the effect of point defects, the conservation of lattice density, and include the diffusion of Ge in the oxide.

In addition to improving our understanding of the process, future work should also focus on the applications of this process specifically its use as a template for growth of GaAs and Ge, as well as improving the responsivity of the detector. As to what should be specifically focused on in this regard work remains to be done on the optimization of the implantation dose, the oxidation length and oxidation temperature. Optimizing the three of these variables may well lead to a thicker layer with a higher Ge concentration and as such a much improved detector. In addition to this it would be beneficial to fabricate future devices so that they are butt coupled rather than grating coupled as this will allow the investigation of a much larger range of wavelengths for a single device.

6.2.2 Long wavelength detection in Ge

Long wavelength detection is of great interest for use in the TDFA band and while the work in this thesis represents an important first step in the use of Ge in detection at higher wavelengths there is still much to be done. A relatively simple step would be the elimination of parasitic absorption associated with free charge carriers from phosphorus doping as discussed in Chapter 4. A more complex avenue of research is the use of the nanowire bridge techniques demonstrated in chapter 5. In order to be used successfully there needs to be the development of

a biaxially strained nanowire structure which would allow for the extraction of charge carriers, in addition to this it would be of great interest to characterize the absorption coefficient of Ge for both biaxially and uniaxially strained devices at higher wavelengths. Finally the development of a Ge-Si avalanche detector which incorporates SACM is another potential avenue of research.